A STUDY OF 4GEV/c $\pi^{\pm}$ -PROTON INTERACTIONS IN A LIQUID HYDROGEN BUBBLE CHAMBER.

by

M. IBBOTSON

A thesis presented for the Degree of Doctor of Philosophy of the University of London.

Department of Physics,
Imperial College of Science & Technology,
London, S.W.7.

November 1963.

CONTENTS

ABSTRACT

This thesis is divided into two parts. In Section I a description is given of a liquid hydrogen bubble chamber expansion system designed for use with the Imperial College 40cm. hydrogen chamber, and as a prototype system for the 150 cm. British National chamber.

Section II contains a study of π^-- proton interactions at an incident pion momentum of 4 Gev/c. The Saclay 81cm. liquid hydrogen bubble chamber was exposed to a beam from the CERN proton synchroton, and produced 60,000 useful pictures. The analysis of those events with two charged secondaries, excluding strange particle events, is presented.

Chapter II reviews the background to and objectives of the experiment. In Chapter III an account is given of the apparatus and methods used in the processing of the film. The individual identification of events is described in Chapter IV. Cross-sections, angular and momentum distributions, and resonance production for the different reaction channels are presented and discussed in Chapters V and VI. Finally in Chapter VII, a brief description is given of some preliminary results of an investigation of π^+-proton interactions of 4Gev/c.

PREFACE.

The work presented in this thesis was undertaken by the author, from October 1958 - April 1962 as a member of the Imperial College bubble chamber group under Mr. N.C. Barford and from April 1962 as a member of the bubble chamber film analysis group under the supervision of Dr. I. Butterworth.

It was decided in 1956 to build a small 10cm. liquid hydrogen bubble chamber at Imperial College. The chamber became operational in January 1958 and was subsequently used for the study of p-p interactions of 146 Mev and n-p interactions around 50 Mev, both using the Harwell cyclotron.[1,2] In early 1958, design began of a 40 cm. bubble chamber for use with hydrogen and deuterium. This chamber was intended to be used as an instrument in its own right, but also as a prototype for the British National chamber.

The author joined the bubble chamber group in October 1958, and initially spent some time gaining experience with the 10 cm. chamber at Harwell. His time was then devoted to the design, construction and testing of the components of the 40 cm. chamber, being especially concerned with the expansion system.

The chamber was transported to Saclay in May 1961 for final testing. It was proposed to study proton-deuteron, and neutron-proton interactions at 3Gev/c using the Saturne proton synchrotron. However, after several tests at nitrogen temperatures, the chamber body was found to have become magnetic and the window clamping flanges badly distorted. To overcome

these technical difficulties would have been very costly in time and money, and the decision was taken to discontinue the project.

The author returned to Imperial College in May 1962 and joined the film analysis group. During the period from November 1961 until February 1962, 60,000 photographs of 4Gev/c π^- had been taken at CERN. This film was analysed by groups from Aachen, Bonn, Hamburg, Munich, Birmingham and Imperial College. The author took responsibility for the organisation of scanning, measuring and analysis of the Imperial College film. The results of this π^- investigation have appeared in four publications.(3)

The analysis by the same collaboration together with an East Berlin group of 70,000 4Gev/c π^+ photographs, taken in April 1962, began in June 1963. The author took part in the scanning and analysis of this film.

CHAPTER I

EXPANSION SYSTEM OF A LIQUID HYDROGEN BUBBLE CHAMBER.

1.1. Introduction.

In 1953, Glaser[4], after a series of experiments with diethyl ether and other liquids, showed that in a superheated liquid, bubble formation occurred along the track of an ionising particle. It was soon realised that such a detector had advantages over other detectors because of its short resolution time, rapid cycling rate, high density and good spatial resolution.[5] Many liquids have been used for this instrument - the bubble chamber - but the greatest effort has been in the construction of liquid hydrogen bubble chambers, the largest in operation being the Berkeley 72", Brookhaven 80" and British National 60" chambers.

1.2. General Considerations.

When a liquid is brought into a superheated state, bubbles of visible size will only form if an energy source is available to create bubbles greater than a critical radius r_c, given by

$$r_c = 2\sigma / (p_v - p_L) \qquad (1.1)$$

where

σ is the surface tension of liquid

p_v is the vapour pressure inside bubble

p_L is the pressure of surrounding liquid

Early theories of nucleation were based on the repulsion of ions

on the bubble wall. Seitz[6], however, in disagreement with the electrostatic theories, showed that δ-rays of about 1kev would deposit their energy in a region 10^{-6} cm. radius, and produce bubbles of critical size in 10^{-10}sec. Typical growth times to bubbles of visible size are between 0.1 and 2 m.sec.

To bring liquid hydrogen into a superheated state one maintains it at just below boiling-point at a given initial pressure (e.g. 29°K at 8 Atm), and then suddenly releases the pressure. For early, all glass, chambers it was possible to hold the condition of superheat for several seconds, but with composite chambers, parasitic boiling prevents a lengthy period of superheat. Hence it is necessary to re-apply the pressure to the liquid after only a few milliseconds. An idealised form of pressure pulse is shown in Fig. 1.1. In order that the heat input to the chamber be small, the duration of the expansion-recompression cycle should be as short as possible, since 'dynamic' heat loss, due to irreversible heat exchanges during the cycle, is in general much greater than the 'static' loss caused by conduction, convection and radiation. The expansion time (Fig. 1.1) must be kept as short as possible to prevent boiling at the chamber walls becoming important. It must not be too short, however, as turbulences may occur, and a time of 5-10 milliseconds is a typical compromise. The recompression time can be as short as possible, although, in general, it is necessarily of the same order as the expansion time. The time of arrival of the beam of particles can vary by 1-2 m.sec., and

allowing for bubble growth time, requires the sensitive time to be 5-10 m.sec. Thus the total expansion-recompression cycle should be between 20 and 30 milliseconds.

1.3. Expansion Systems.

There are in general two ways of expanding a bubble chamber: liquid expansion and gas expansion. In the former, a piston or bellows system in contact with the liquid surface performs the expansion. In the latter, the gas above the liquid is expanded.

Various technical problems present themselves in the design of expansion systems for liquid hydrogen chambers. It is essential to have complete reliability of the moving parts. This is especially true in the case of liquid expansion, as the piston or bellows work at hydrogen temperatures. Thus, to repair a broken piston ring or fractured bellows, the whole chamber must be brought to room temperature and for large chambers this could take several days. A gas expansion system has its moving parts at room temperature. However, turbulent gas flow promotes the mixing of hot and cold gas in the expansion pipes, and flashing also tends to occur at the liquid surface. Both these effects tend to increase the dynamic heat loss for gas expansion systems.

1.4. The 40 cm. Chamber Expansion System.

A schematic diagram of the expansion system is shown in Fig. 1.2. The gas line from the chamber was joined through two valves to high and low pressure tanks of 1 and 120 cu.ft. respectively. These valves will be

referred to as the recompression valve and the expansion valve. During the expansion cycle, the expansion valve had to close before the recompression valve opened to prevent direct connection of the high and low pressure tanks. A compressor pumped gas from the low pressure tank to the high pressure tank. This system is known as a closed circuit gas expansion system.

These valves consisted of a cylindrical steel spool, ground and highly finished to a precision sliding fit within a sleeve containing holes at one end. (Fig. 1.3.(b)). The valve was opened when the spool was at one end of the sleeve, and gas flowed through the radial holes. In the closed position, the spool covered these holes. The good sliding fit required no lubricant, and the leak rate between sleeve and spool could be made sufficiently small. Specially designed rubber buffers were used to stop the moving spool at the end of its travel.

The expansion and recompression valves were opened and closed with the use of pilot valves. To keep the main valves closed against a line pressure of say, 100 psig,required the use of a pressure in excess of this, say 120 psig. To open the main valve, the excess pressure was released through the pilot valve. A pilot valve was designed to have very precise timing of operation. The valve was operated by the fast movement of a piston which opened a 1" port for 10 m.sec. The valve body formed the yoke of an electromagnet, and the piston was held in its closed position by magnetic attraction to the valve body. A small 'knock-off' coil was

wound on the same former as the main coil, and was so arranged that when a discharge current was passed through it, it reversed the main field, and allowed the pressure to force up the piston, thus opening the valve (Fig.1.4(a) A spring returned the piston. A typical timing sequence of the pilot and main valves is shown in Fig. 1.3(a).

The chamber itself was a cylinder of 40 cm. diameter and 20 cm. effective depth, giving a useful liquid volume of around 25 litres. In order to prevent the turbulent motion of the liquid during the expansion cycle causing distortion of the tracks, it is desirable to expand the liquid in the direction of the magnetic field. To achieve this and also to provide uniform linear flow, the chamber body contained an expansion manifold near the chamber window with radial slots of different width, calculated to give equal volume flow through each slot. These slots led into an annular ring, which in turn led to the expansion pipes (Fig.1.5). The liquid in the chamber was calculated to have a natural period of oscillation of 12 milliseconds, so that the half-period (6 m.sec.) could be used for the pressure pulse generated in the chamber during each expansion cycle.

1.5. Performance of Expansion Valves.

The reliability of operation of the main expansion valves was dependent on the clearance between spool and cylinder. It was necessary to have a small clearance to keep the leak rate small compared with the compressor pumping speed. The leakage through the valve is given by

$$\frac{dV}{dt} = \frac{h^3 w}{3\eta \ell} \cdot \frac{p_2^2 - p_1^2}{p_o} \qquad 1.2$$

w is the width of gap

$2h$ is the spool-sleeve clearance on diameter.

η is the viscosity of the gas.

l is the length of leakage pa th

p_1, p_2 are the downstream and upstream pressures.

p_o is one standard atmosphere.

The first valve used (Fig. 1.6(a)) cycled very reliably for 10,000 cycles. It had, however, a clearance (2h) of 0.70×10^{-3} inch, which with 100 psi. pressure difference, corresponds to a leak rate of 3 standard litres/sec. This leak rate was not insignificant when compared with the compressor pumping speed (14 litres/sec.). When the clearance of the valves (2h) was reduced to 0.2×10^{-3} inch, the leak rate was then only 0.1 litre/sec, but considerable difficulty was experienced with scratching of the highly finished surfaces. This was due to both dirt in the plumbing system, and 'belling' of the ends of the spools from the high forces of impact.

Another form of valve experimented with consisted of an aluminium spool of large clearance but containing "Gaco" rubber sealing rings (Fig.1.6(b) The speed of the valve was not seriously affected, but again scratching of the surfaces was experienced.

The pilot valves performed 150,000 operations without fault. The main trouble experienced was an electrical one associated with the lifetime of the discharge tube, used to supply the pulsed current to the 'knock-off' coil.

A circuit was subsequently designed giving a discharge tube life in excess of 3×10^6 cycles (1.4(b)). By means of monitoring the induced current in the main coil, a measure of the valve speed was obtained. Fig. 1.4.(c) shows an oscilloscope trace of a typical valve operation, indicating an open and close time of 12 milliseconds. No bounce of the piston was observed on its closure.

1.6. British National Chamber Expansion System.

A brief description of the essential features of the chamber has been given elsewhere[7]. The expansion aperture of the chamber is divided into many cells, and 48 pipes join this to the expansion valves to provide a turbulence-free expansion. The volume of gas between the expansion (and recompression) valve and the liquid-gas interfaces in the pipes is approximately 70 litres. This is 20 grms. of gas, assuming an initial pressure of 90 psia and an expanded pressure of 45 psia and as the transfer rate for hydrogen at room temperature is about 7 gms./sec./cm.^{2}/atmosphere, the size of aperture required for the valve is approximately 100 cm.^{2} in order to pass the gas in 5 milliseconds. In practice four $2\frac{1}{2}$" valves in parallel are used. Fig. 1.7 shows a schematic arrangement of the chamber and valves.

As in the 40 cm. chamber, the valves used consist of metal sleeves and spools ground to close tolerances. In early prototype valves, difficulties were experienced due to seizing of the valves in operation. Increasing the hardness of the rubbing surfaces now seems to have cleared this problem and the type of valve now in use has successfully performed 50,000 operations.

Nylon buffers are used to stop the spools at the end of their travel.

Fig. 1.6(c) shows a new expansion valve designed recently with a spool of weight about 50% of that of previous ones in an effort to reduce the loading on the buffers and to speed up the turn-round time of the valve. This will be manufactured and tested shortly.

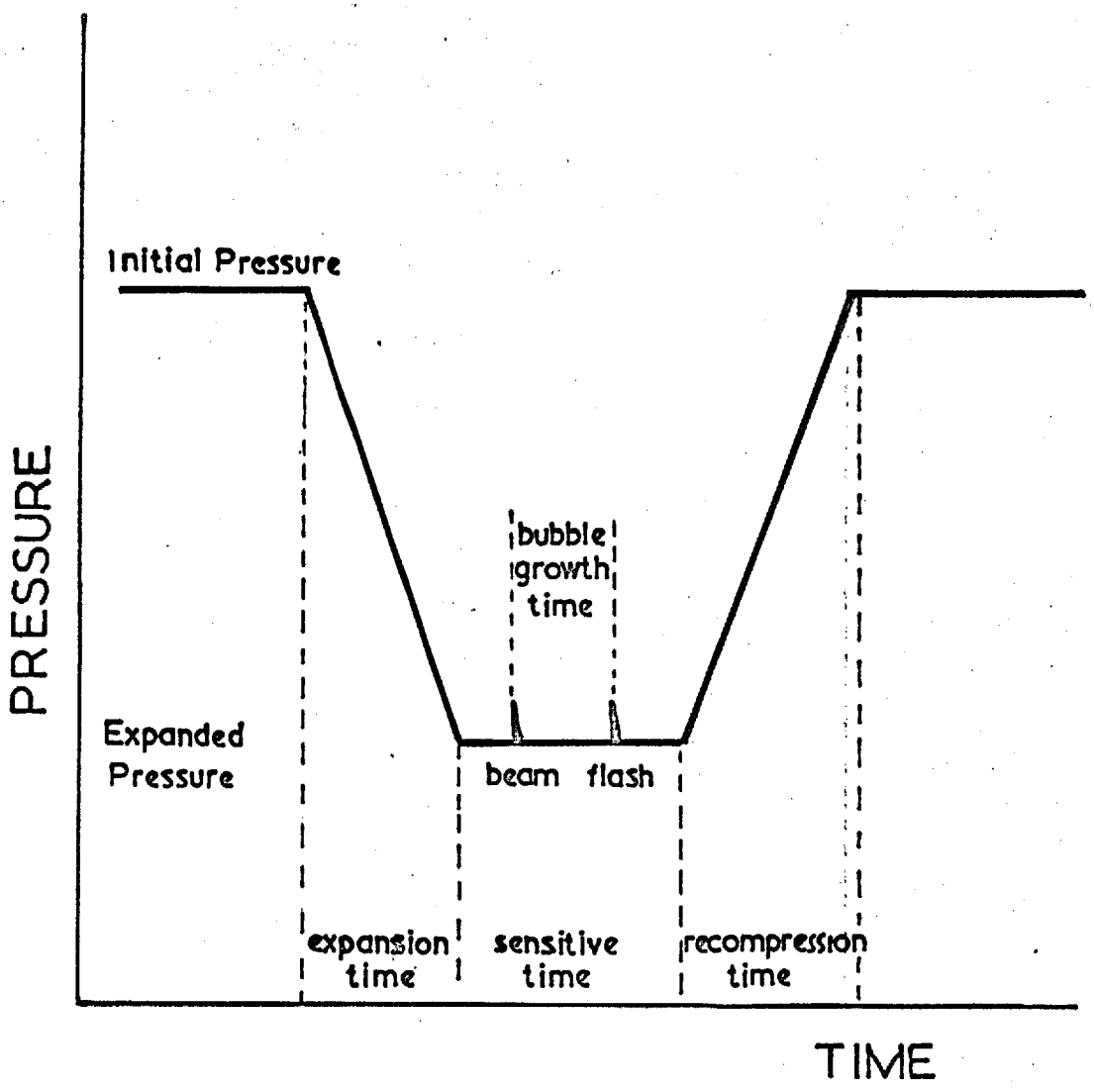

IDEALISED BUBBLE CHAMBER PRESSURE PULSE

Fig. 1.1

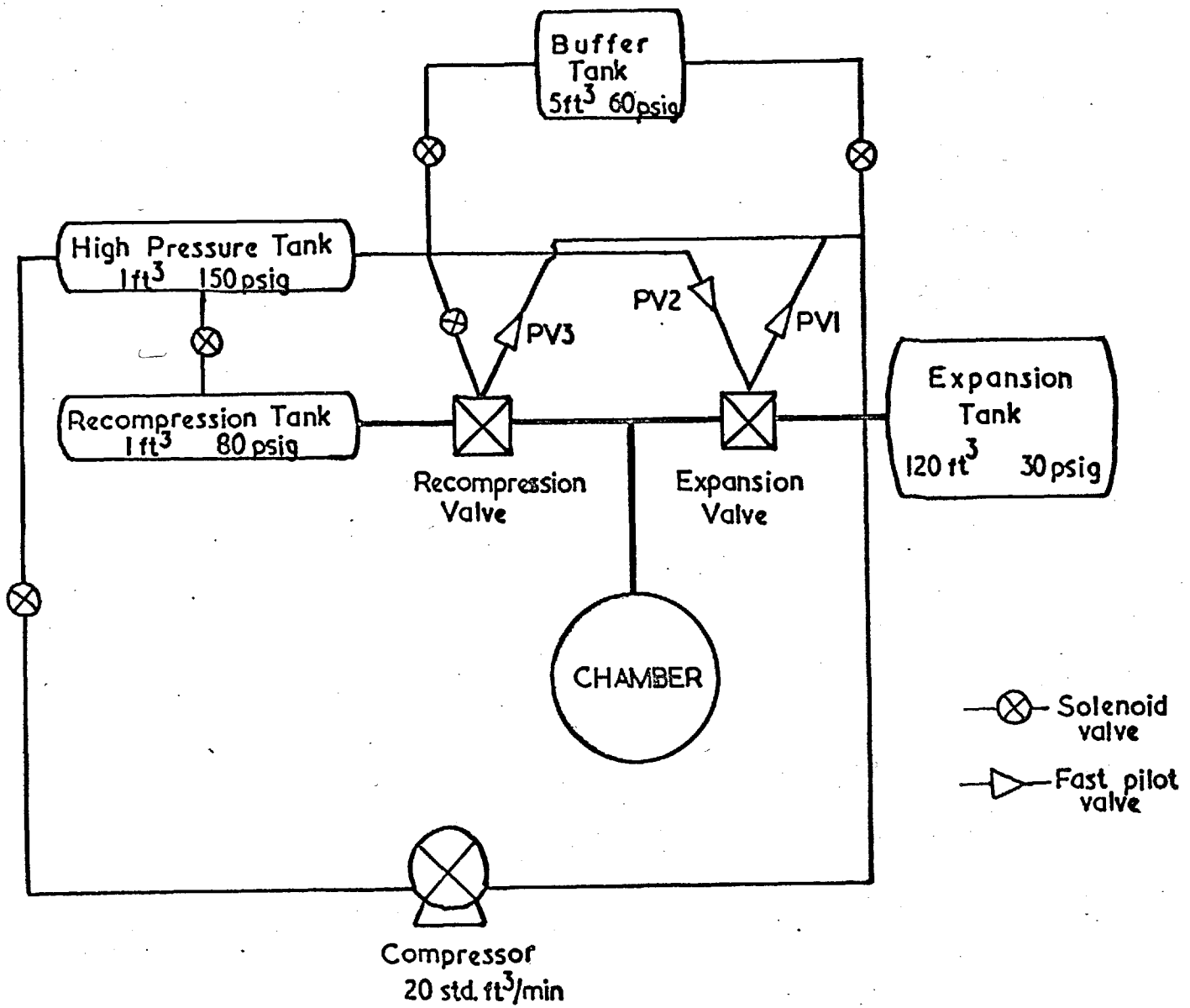

Fig. 1.2

40 CM. CHAMBER GAS EXPANSION CIRCUIT

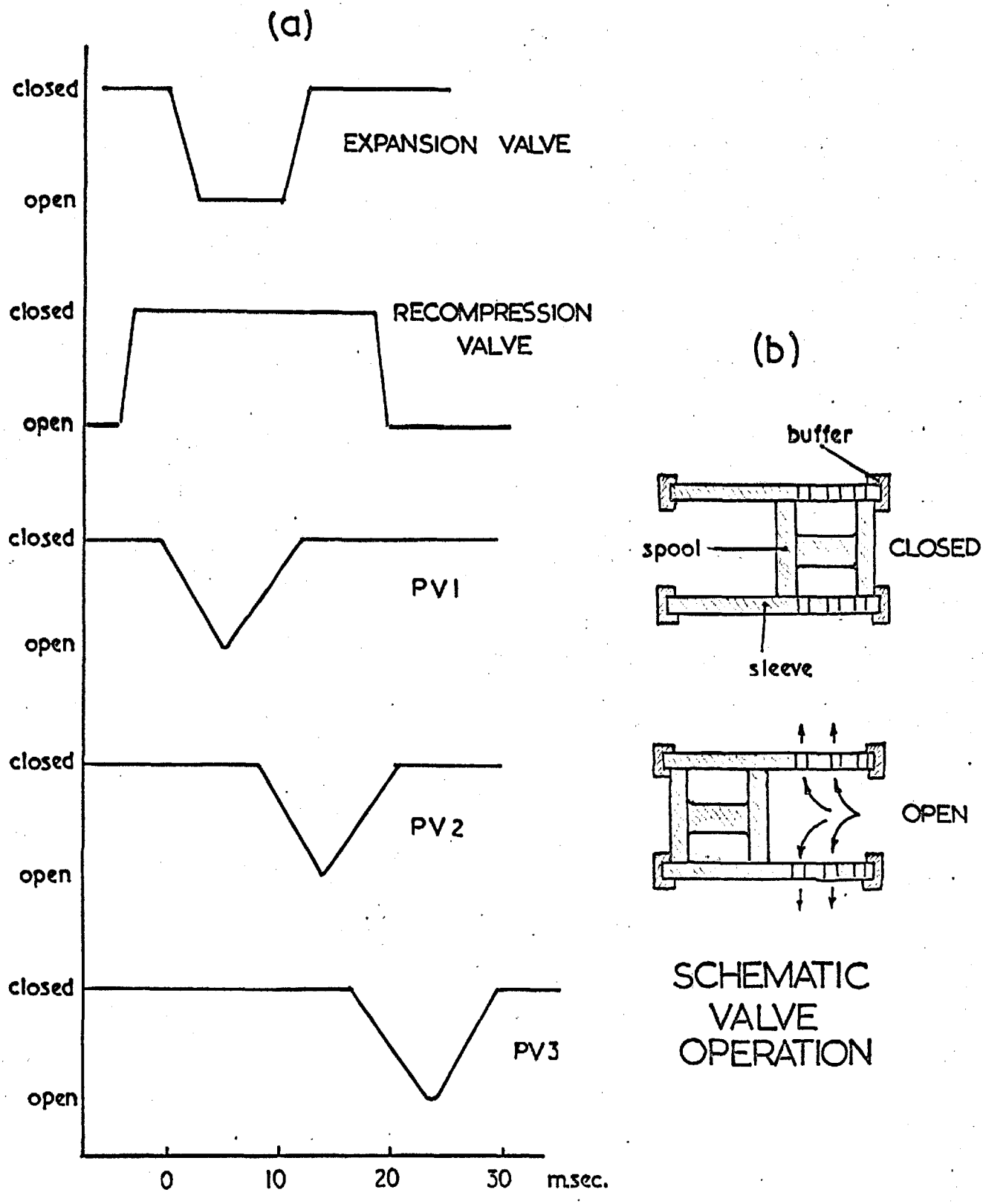

TYPICAL VALVE TIMING SEQUENCE

Fig. 1.3

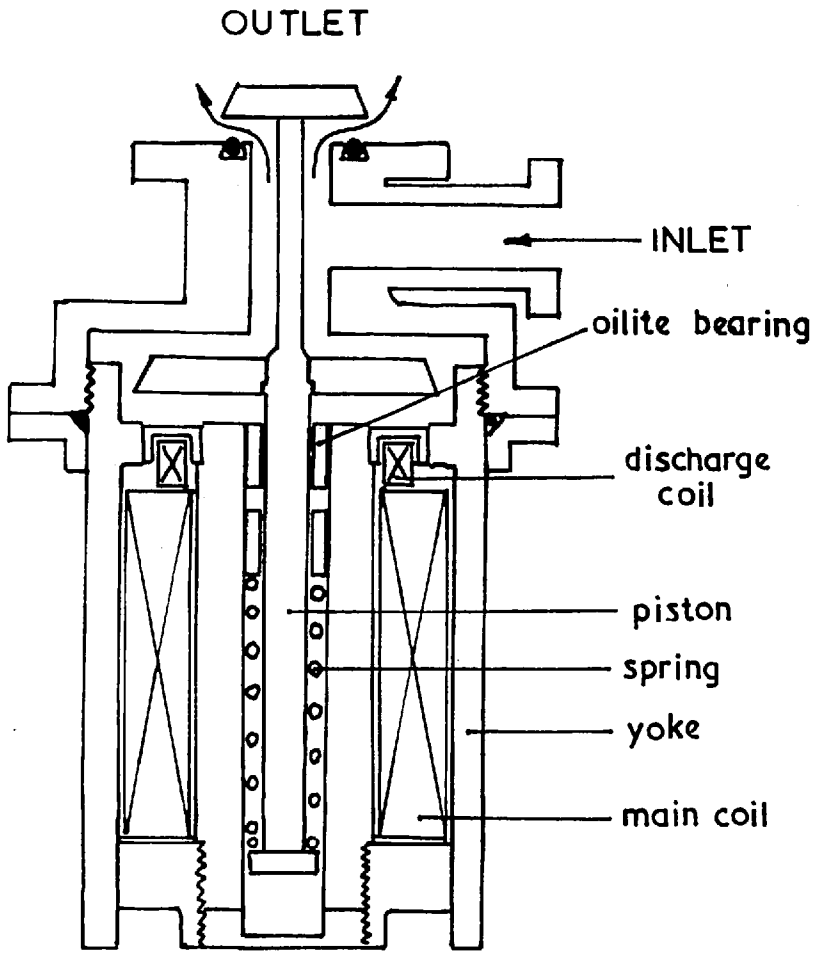

(a) FAST PILOT VALVE

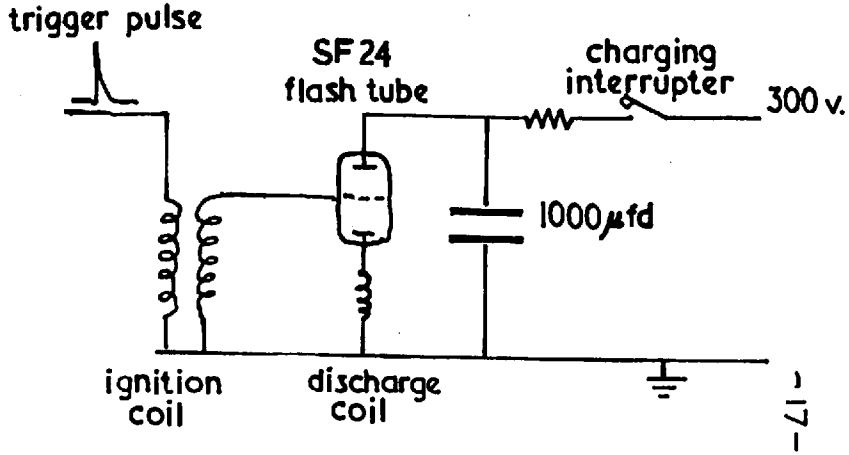

(b) DISCHARGE CIRCUIT

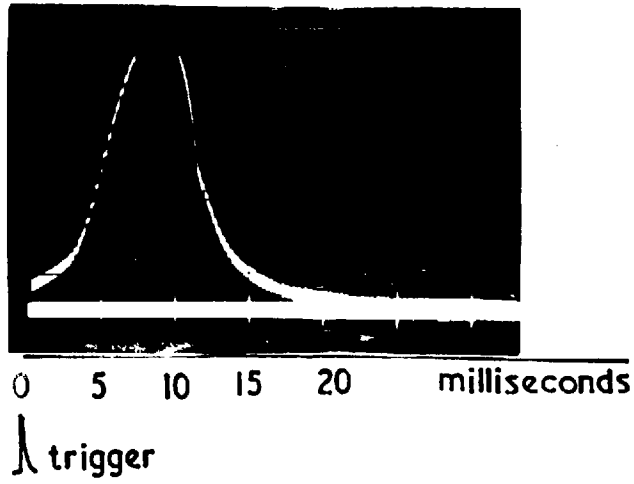

(c) PISTON MONITOR

Fig. 1.4

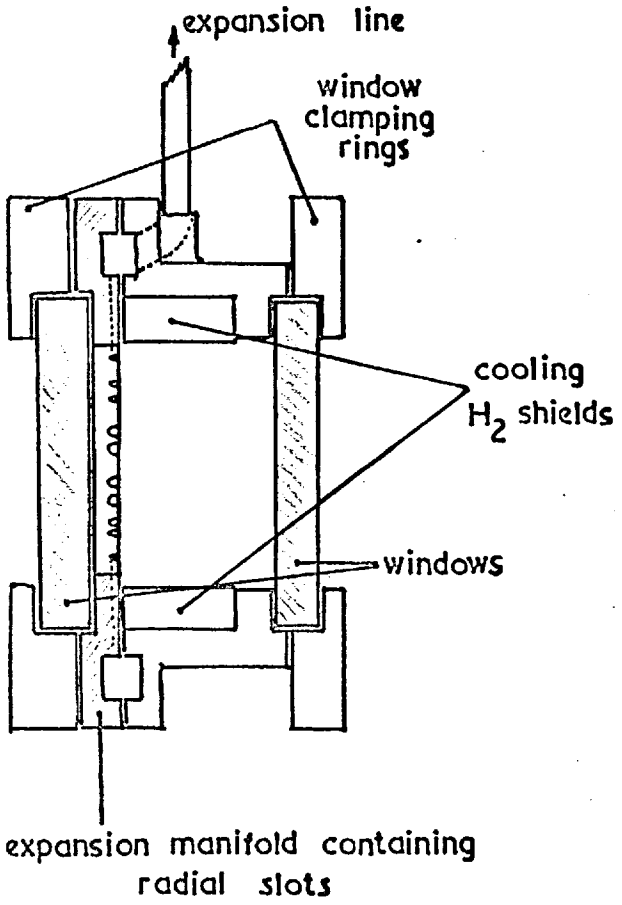

CHAMBER BODY

Fig. 1.5

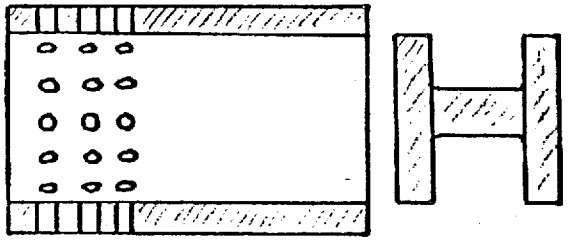

(a) ORIGINAL VALVE

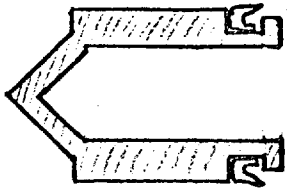

(b) GACO SPOOL

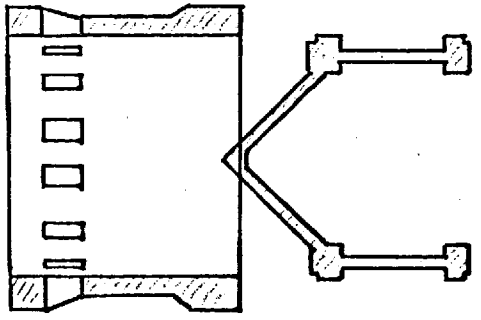

(c) NATIONAL CHAMBER VALVE

EXPANSION VALVE DESIGNS

Fig. 1.6

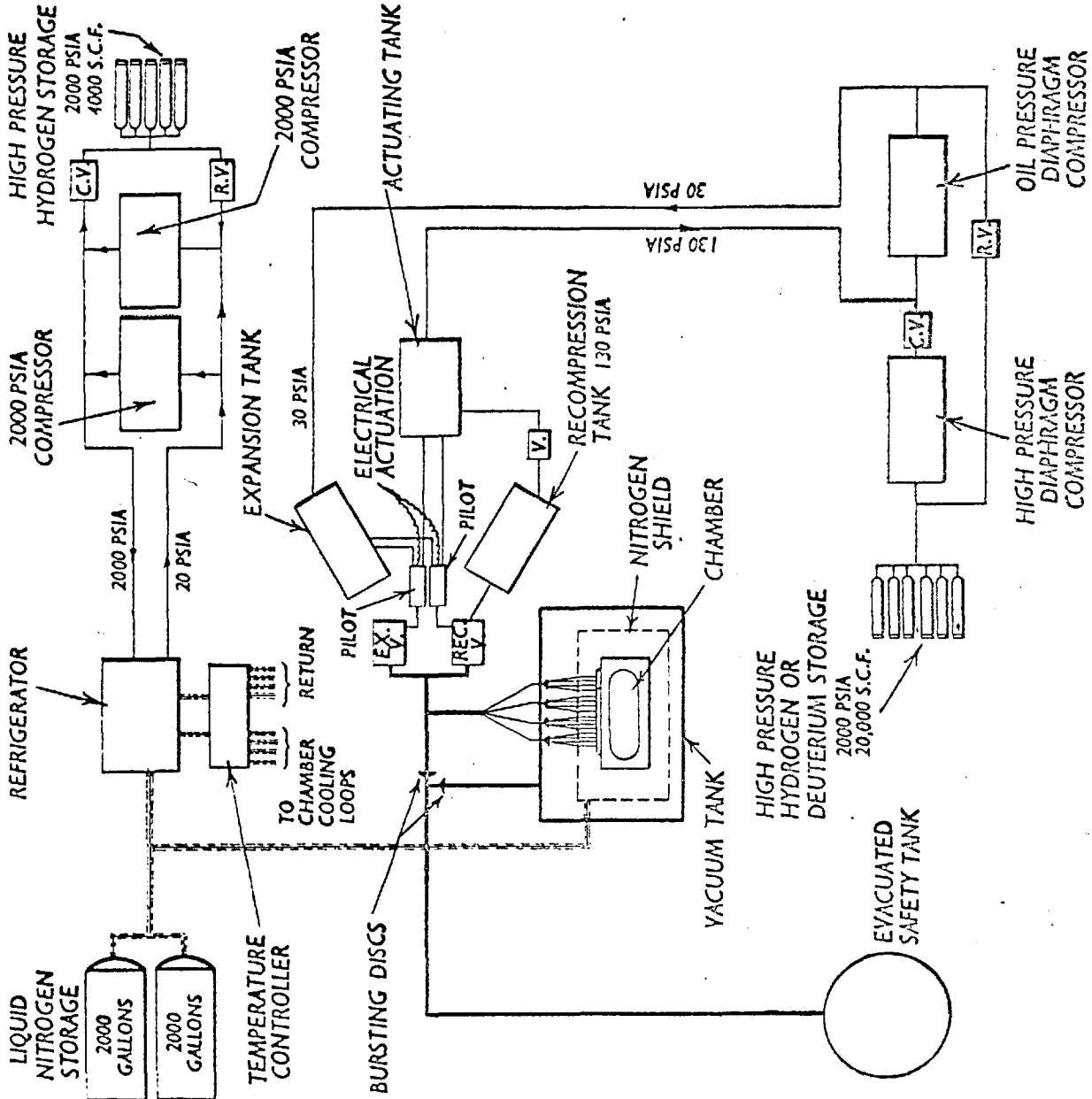

60" HYDROGEN BUBBLE CHAMBER

FIG. 1.7

CHAPTER II

BACKGROUND TO AND OBJECTIVES OF THE EXPERIMENT.

2.1. Pion Resonances.

Investigation of pion-nucleon interactions have tended to fall into categories according to the magnitude of the incident pion momenta. Experiments at incident pion momenta up to about 300 Mev/c have yielded detailed information on elastic scattering and could be analysed in terms of phase shifts. At higher energies, there is enough energy to produce additional particles. The number of angular momentum states increases and a phase shift analysis is no longer feasible. Early inelastic scattering experiments studied the multiplicity of pion production and compared this with the predictions of statistical theories of pion production[8,9]. These experiments also showed that as the energy increases the interaction becomes more 'peripheral' i.e. the incident pion interacts only with a virtual pion in the meson cloud surrounding the nucleon. With the introduction of high quality bubble chamber photographs and fast computer programmes, it became possible to completely analyse individual interactions, and hence determine the branching cross-sections for each inelastic channel. Also, by studying correlations between two or more final state pions, resonant states of pions were observed.

Resonances have been discovered in two different experimental situations. Firstly, the two particles in the initial state of a reaction can be at a

resonant energy. Most of the pion-nucleon resonances were discovered in this way, mainly by the use of counter techniques. Secondly, two or more of the particles in a many-body final state can be at a resonant energy. These resonant states have been found mainly in experiments using bubble chambers.

In bubble chamber experiments, the procedure in looking for resonances is usually as follows. Kinematic analysis identifies the interaction, and a grouping is made of all events identified as having the same final state particles. One then calculates the invariant mass of the n selected particles ,

$$M_n^* = \left[\left(\sum_{i=1}^{n} E_i \right)^2 - \left(\sum_{i=1}^{n} \vec{p}_i \right)^2 \right]^{\frac{1}{2}} \qquad (2.1)$$

where E_i, p_i are energy, momentum of individual particles in final state.

and studies the frequency distribution of the mass values. This distribution is then compared with that expected from the kinematics of the final state particles (see next section).

In order to explain the electromagnetic structure of the nucleon, Frazer and Fulco [10] suggested that there should exist a strong p-wave pion-pion resonance at a mass squared value of $11\mu^2$ (μ is the pion mass). Bowcock et al.[11] supported this suggestion, but predicted a mass squared value of $22\mu^2$. The first convincing experimental evidence for this

resonance was presented by Erwin et al.,[12] who analysed 1.9 Gev/c $\pi^- p$ interactions in the 14" Adair bubble chamber, and also by Stonehill et al.,[13] who analysed 1.09 Gev/c and 1.26 Gev/c $\pi^+ p$ interactions in the Shutt 20" bubble chamber. They studied the reactions :

$$\pi^{\pm} p \longrightarrow \pi^{\pm} \pi^{o} p$$

$$\longrightarrow \pi^{\pm} \pi^{+} n$$

and examined all dipion combinations. They found significant departures from phase space in the $(\pi^+ \pi^-)$ and $(\pi^{\pm} \pi^o)$ mass distributions, but not in the $(\pi^+ \pi^+)$ mass distribution. The peak of the resonance was found to be at 760 Mev (mass squared value $29\mu^2$) and had a width of about 100 Mev. This so-called ρ -resonance (ρ -meson) has since been observed in many bubble chamber experiments.[14,15] The central mass value and width vary from one experiment to another, but are about 750 Mev and 110 Mev respectively. The ρ -resonance is observed to decay as follows,

$$\rho^+ \longrightarrow \pi^+ \pi^o$$

$$\rho^o \longrightarrow \pi^+ \pi^-$$

$$\rho^- \longrightarrow \pi^- \pi^o$$

$$\rho \not\longrightarrow \pi^{\pm} \pi^{\pm}$$

which indicates that the isotopic spin, $T=1$. Also the ratio $\frac{\pi^- p \longrightarrow n \rho^o}{\pi^- p \longrightarrow p \rho^-}$ is observed experimentally to be 1.8 ± 0.3, which is consistent with the

charge independence prediction of a ratio 2 for a T=1 ρ -particle. Since the resonances has a broad width, and hence decays by strong interactions, the G-parity,

G-parity = (charge conjugation parity)x(charge symmetry)

is even. The spin angular momentum, J, of the ρ resonance has been determined in two ways. The angular distribution of the decay products of the ρ , and the peak value of the π - π scattering cross-section as calculated by the Chew-Low method, both indicate that J=1. Thus the quantum numbers of the ρ -meson are $J^{PG} = 1^{-+}$, and T=1, where J is the angular momentum, $P = (-1)^J$ is the parity, and G=G-parity. There has been a suggestion of a double peaked structure for the ρ [16], but no other experiments have so far convincingly confirmed this.

The next resonant state to be discovered was the ω-meson. It was first seen in proton-antiproton annihilations at 1.61 Gev/c by Maglic et al.[17] who analysed the reaction :

$$\bar{p} + p \rightarrow \pi^+ \pi^- \pi^o \pi^+ \pi^-$$

They examined all 3π mass combinations, and in the ($\pi^+ \pi^- \pi^o$) combinations found a very narrow peak above background at 785 Mev. The width of the peak was comparable with the experimental resolution of their experiment. In other 3π mass combinations ($\pi^\pm \pi^\pm \pi^\mp$, $\pi^\pm \pi^\pm \pi^o$), no peak was observed, leading to the assignment that the isotopic spin, T=0. This resonance has been confirmed elsewhere,[18] and is best described with

a mass value of 784 ± 1 Mev, and a width of (9.4 ± 1.5) Mev[19]. A particle which decays into three pions leads to a more difficult determination of its quantum numbers. However, from the experimental distribution of points on the Dalitz plot for the ω, evidence is obtained concerning the matrix element for ω decay, yielding the quantum numbers $J^{PG} = 1^{--}$.[17] A particle with these quantum numbers had been predicted by Nambu[20] and Chew [21] to explain the theoretical interpretation of the electromagnetic structure of the nucleon. They postulated that one should expect a three pion T=0 particle, if the two pion T=1 ρ-particle existed.

Pevsner et al[18], studying the reaction :

$$\pi^+ + d \longrightarrow p + p + \pi^+ + \pi^- + \pi^o$$

saw, in the mass spectrum of the $\pi^+ \pi^- \pi^o$ system, a narrow peak at 550 Mev, in addition to their ω-peak at 780 Mev. A more detailed study of this resonance, the η meson, was made by Bastien et al., [22] who analysed the reaction :

$$K^- + p \longrightarrow \Lambda^o + \pi^+ + \pi^- + \pi^o$$

at an incident K^- momentum of 750 Mev/c. They also looked for events of the type

$$K^- + p \longrightarrow \Lambda^o + \text{neutrals},$$

and saw a peak in the missing mass spectrum of the neutrals. They deduced

that the ratio:

$$\frac{\eta \rightarrow \text{neutrals}}{\eta \rightarrow \pi^+ \pi^- \pi^o} \quad \text{was equal to } 3.0 \pm 1.0$$

Their results suggested that the η had isospin T=0 (from the non-existence of a charged counterpart $\eta^{\pm}$) and decayed electromagnetically with isospin violation. Other decay modes of the η have been investigated extensively by other groups Convincing evidence for the other quantum numbers has been obtained by combining the data for several experiments on a Dalitz plot for the $\pi^+ \pi^- \pi^o$ decay mode[23]. It is now believed to have $J^{PG} = 0^{-+}$.

The production of ρ. ω and η particles has been shown to represent a significant fraction of multiple pion production in pion-proton interactions above 1 Gev/c. They are the only pion resonances which prior to this experiment had had convincing determinations of their quantum numbers.

A peak has been observed by Abashian, Booth, and Crowe (24) in the momentum spectrum of He^3 in the reaction

$$p + d \rightarrow He^3 + \text{other particles}$$

and could be due to a dipion resonance with a mass value of 300 Mev. Tentative assignments, T=J=0 have been made, but have had no real confirmation, although some weak supporting evidence has recently appeared.[24] This suggested dipion resonance is known as the ABC resonance, but is currently thought to be due to an s-wave interaction near threshold.

Barloutaud et al [25] observed a T=1 peak in the dipion spectrum at 575 Mev. This has had some supporting evidence from other groups, but

Stonehill et al.[26] performing an experiment identical to that of Barloutaud do not see this peak. This peak is known as the ξ resonance.

Several other resonances have been proposed by different experimenters but without confirmation from other groups. However, recently, in a study of $\pi^- p$ interactions at 3 Gev/c, Selove et al[27] have reported a T=0 dipion resonance at 1250 Mev witb a width of 100 Mev. A J=2 resonance at about this mass value has been proposed theoretically on the basis of the Regge pole approach[28]. The above experiment was unable to conclusively determine the quantum numbers of this resonance, now called the f^o resonance.

2.2. Pion-Pion Interaction.

Detailed considerations of peripheral models in inelastic processes were first made by Chew and Low[29]. They hoped to describe the cross-section for a process such as $\pi^- p \rightarrow p\ \pi^-\ \pi^o$ on the basis of a one pion exchange model :-

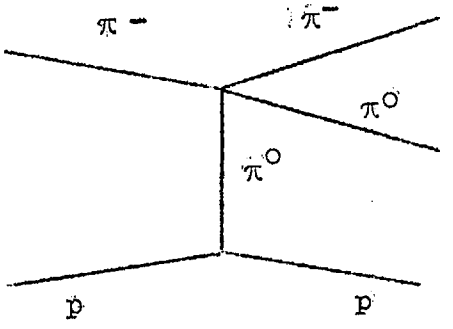

They related the overall differential cross-section, as a function of the four-momentum transfer, t, and the energy at the upper $\pi\pi$ vertex, ω^2, to the pion-pion cross-section, where

$t = (p'-p)^2$ is the invariant four-momentum transfer squared to the nucleon.

p', p being the four momenta of incident and final nucleons.

ω^2 is the square of total energy of the outgoing pions in their centre of mass system.

Such an approach is the only method at present available of obtaining a measure of the pion-pion cross-section. Pion-pion scattering cannot be studied directly, unless clashing beam accelerators are able to provide effective pion targets.

Chew and Low show that

$$\lim_{t \to \mu^2} \frac{\partial^2 \sigma}{\partial t \, \partial \omega^2}(\omega^2, t) = \frac{f^2}{2\pi} \frac{t}{(t-\mu^2)^2} \cdot \frac{\omega \left(\frac{\omega^2}{4} - \mu^2\right)^{\frac{1}{2}}}{\mu^2 \, q_{1L}} \cdot \sigma_{\pi^-\pi^0}(\omega^2) \qquad 2.2$$

where f^2 is the pion-nucleon coupling constant ~ 0.08

q_{iL} is the laboratory momentum of incident pion

$\sigma_{\pi^-\pi^0}(\omega^2)$ is the pion-pion cross-section at energy ω^2

This formula is only valid at the unphysical point $t = \mu^2$, and so if one applies this method to deduce a value for $\sigma_{\pi\pi}(\omega^2)$, one plots the experimental points on a plot of $(t-\mu^2)^2 \frac{\partial^2 \sigma}{\partial t \, \partial \omega^2}$ against $-t$, and extrapolates the graph to the limit $t = +\mu^2$. This is known as the Chew-Low extrapolation method. Unfortunately to perform a successful extrapolation, it is

necessary to have greater statistics than present experiments can supply especially with low physical values of t.

However, if a good linear fit passing through the origin t=0 is obtained, the assumption of dominance of the one pion exchange model is a reasonable one. Further, the assumption is usually made that the Chew-Low formalism extends up to small physical values of t. One can then obtain $\sigma_{\pi^-\pi^o}(\omega^2)$ by direct integration of equation 2.2 over t.

$$\frac{\partial\sigma}{\partial(\omega^2)} = \frac{f^2}{2\pi}\,\frac{\omega}{\mu^2}\,\frac{(\omega^2/4-\mu^2)^{\frac{1}{2}}}{q1L}\,\sigma_{\pi^-\pi^o}(\omega^2)\int_{t_{min}}^{t_{max}}\frac{t}{(t-\mu^2)^2}\,dt \qquad 2.3$$

where t_{min} is the limit imposed by kinematics and t_{max} is the selected upper limit, both being functions of ω^2 (see Fig 6.1).

Anderson et al[30] carried out an analysis of this type for $\pi^+p \rightarrow \pi^+p\pi^o$, and showed that the $\pi\pi$ cross-section at the unphysical limit, obtained by extrapolation, and in the physical region for low $|t|$ values, has a resonance at $\omega^2 = 25\mu^2 - 30\mu^2$, and with a cross-section approximating to that required for a J=1 resonance.

Other experimenters[31] have had limited success with the extrapolation procedure due to the need for high statistics, and have tended to assume the validity of the Chew-Low formalism in the physical region. The values for $\sigma_{\pi\pi}$ obtained in the ρ -resonance region ($\omega^2 = 30\mu^2$) tended to be

somewhat low compared with the expected value for true resonant elastic $\pi\pi$ scattering of 12 $\pi\lambda^2$ for J=1.

A modification to the Chew-Low formula has been recently made by Selleri[32]. He made allowance for the exchanged virtual pion being off the mass shell (i.e. not satisfying energy and momentum conservation) by introducing a factor into the Chew-Low formula thus :-

$$\left(\frac{d^2\sigma}{dt\, d\omega^2}\right)_{\text{Selleri}} = \left(\frac{q^{off}}{q}\right)^{2l} (F(t))^2 \left(\frac{d^2\sigma}{dt\, d\omega^2}\right)_{\text{Chew. Low}} \qquad 2.4$$

where

$$q^{off} = \left[\left(\frac{\omega^2 - t + \mu^2}{2\omega}\right)^2 - \mu^2\right]^{\frac{1}{2}}$$

$$q = -\left(\frac{\omega^2}{4} - \mu^2\right)^{\frac{1}{2}}$$

$F(t)$, related to the pionic form factor of the nucleon

$$= \frac{0.72}{1 + \frac{-t+\mu^2}{4.73\mu^2}} + 0.28$$

ω is the total energy in the outgoing $\pi - \pi$ centre of mass system.

l is the angular momentum of $\pi - \pi$ state.

During their study of π^-p interactions at 1.59 Gev/c, the Saclay-Orsay

Bari-Bologna collaboration [32] examined the distribution of $\sigma_{\pi^+\pi^-}(\omega^2)$ from the reaction $\pi^- + p \rightarrow n + \pi^+ + \pi^-$, as calculated by the Chew-Low formula assumed to be valid for $-t < 8\mu^2$. This distribution showed a maximum of 56 ± 8 mb., appreciably lower than the value of $12\pi\lambda^2 = 120$ mb. expected for resonant elastic J=1 $\pi - \pi$ scattering at the peak of the ρ-resonance. However, the corrected Selleri formula gave a peak value of 108 ± 16 mb., in good agreement with the expected value.

2.3. Phase Space Distributions and Dalitz plots.

In order to compare experimental results, such as effective mass, momentum distributions of final state particles with theoretical predictions, one usually superimposes a normalised phase space curve. The transition rate between an initial state $|i\rangle$ and final state $\langle f|$ can be shown to be [33]:

$$d\tau = 2\pi |\langle f | T | i \rangle|^2 \, d\rho \qquad 2.5$$

where T is the matrix element for the transition

$d\rho$ is the energy density of final states (phase space density)

For simplicity's sake, one normally assumes that the matrix element is independent of the final state kinematic configuration i.e.

constant, although this is known not to be true for peripheral interactions. An example of the use of a constant matrix element is given by Fermi's statistical theory of multiple pion production [9]. In this

case, then, the transition rate or probability of attaining a given final state is just proportional to the density of final states.

As an example, one can consider a final state of three particles (e.g. $\pi^- p \rightarrow p \pi^- \pi^o$). The Lorentz invariant form of the density can be written [34]

$$d\rho \sim \frac{1}{(2\pi)^9} \frac{d^3\vec{p}_1}{2\varepsilon_1} \frac{d^3\vec{p}_2}{2\varepsilon_2} \frac{d^3\vec{p}_3}{2\varepsilon_3} \delta(\vec{p}_1+\vec{p}_2+\vec{p}_3)\delta(E-\varepsilon_1+\varepsilon_2+\varepsilon_3) \qquad 2.6.$$

where the δ-functions exhibit requirements of energy ($\Sigma\varepsilon_i = E$) and momentum ($\Sigma p_i = 0$, because in overall centre of mass system) conservation.

To obtain the phase space distribution of C.M. momentum or energy of a single particle or effective mass of a group of particles, one integrates over all variables except the one of interest. e.g. to obtain the momentum distribution of $\vec{p_3}$, one integrates over all kinematically allowed $\vec{p_1}$ and $\vec{p_2}$.

It is customary to exhibit the kinematic correlations for three body final states in a so-called Dalitz plot. The centre of mass energies of two of the outgoing particles define a point in a two-dimensional plot. The constraints of energy and momentum conservation restrict the location of the point to a certain region. It is a convenient property of this Dalitz plot that a unit of area in the allowed region is proportional to a unit of Lorentz invariant phase space [35]. One can see this from equation 2.6 above, if one integrates over $\vec{p_3}$ and all angles except between

$\overrightarrow{p_1}$ and $\overrightarrow{p_2}$ to be left with $\rho(\varepsilon_1,\varepsilon_2)\, d\varepsilon_1 d\varepsilon_2$ i.e.

$$\rho(\varepsilon_1,\varepsilon_2)\, d\varepsilon_1 d\varepsilon_2 \sim \int \frac{p_1^2 dp_1 d(\cos\vartheta) p_2^2 dp_2 d(\cos\vartheta_{12}) \delta(E-\varepsilon_1-\varepsilon_2-\varepsilon_3)}{\varepsilon_1 \varepsilon_2 \varepsilon_3}$$

and since $\varepsilon_1^2 = p_1^2+m_1^2$, $\varepsilon_2^2 = p_2^2 + m_2^2$

$$\varepsilon_3^2 = m_3^2+p_1^2+p_2^2+2p_1p_2\cos\vartheta_{12}$$

$$\rho(\varepsilon_1,\varepsilon_2)\, d\varepsilon_1 d\varepsilon_2 \sim \int \delta(E-\varepsilon_1-\varepsilon_2-\varepsilon_3)\, d\varepsilon_1 d\varepsilon_2 d\varepsilon_3$$

$$\sim \quad d\varepsilon_1 d\varepsilon_2$$

i.e. $\rho(\varepsilon_1,\varepsilon_2)$ = constant.

Thus if a three body reaction proceeds according to Lorentz invariant phase space, the corresponding Dalitz plot will exhibit a constant density of points.

For each ε_1, there is a 'strip' of allowed values of ε_2. Along this strip, the effective mass of particles 2 and 3 is constant, since :

$$M_{23}^2 = (\varepsilon_2+\varepsilon_3)^2 - (\vec{p}_2+\vec{p}_3)^2$$

$$= E^2+m_1^2 - 2E\varepsilon_1$$

and $M_{23}^2 + M_{12}^2 + M_{13}^2 = E^2 + \sum_{i=1}^{3} m_i^2$ 2.7

Thus a variant of the conventional Dalitz plot is a plot of effective masses

instead of energies.

Let a particle of mass M_{23} 'decay' into particles (2,3) in its own rest system with an angle ϑ^* with respect to its line of flight. It can be shown by a Lorentz transformation from the decay rest system to the overall centre of mass system that

$$\cos\vartheta^* = A\varepsilon_2 - B \qquad 2.8$$

where A and B are constant along strips of constant ε_1.

Thus if the three particle production process occurs by the formation of a compound particle or resonance of mass M_{23}, subsequently decaying in its own rest frame with a certain angular distribution $\frac{dN}{d(\cos\vartheta^*)}$ into particles 2 and 3, the experimental Dalitz plot will exhibit a concentration of events along a strip of constant ε_1, and the density along this strip will vary as $\frac{dN}{d(\cos\vartheta^*)}$.

2.4. Objectives of the Present Experiment.

The 1-2 Gev/c incident pion momentum region has been thoroughly explored recently, and several experiments have been carried out in the 20Gev/c region. In the latter case the high momenta of the secondary particles prevented an accurate analysis of each event.

Since events with low four-momentum transfer squared have been seen to be important in the study of peripheral collisions, the primary momentum should be as high as possible, although compatible with a full analysis of

each event. To identify events with a missing neutral particle, it is necessary to measure the event accurately enough to allow a good determination of the missing mass. If one pion mass is set for the error allowable on the determination of the neutral particle mass, and the maximum detectable momentum assumed to be 300 Gev/c for the 81 cm bubble chamber, calculation shows that the incident momentum should not exceed 6Gev/c. As a beam was already set up for 4Gev/c antiprotons, it was decided that an incident pion momentum of 4Gev/c would best suit all requirements.

The primary objectives of the experiment were to study multipion production mechanisms in the light of the peripheral model, and to investigate further the production and decay properties of well-known resonant states. With the high incident pion momentum it was intended to explore the existence of non-strange resonances with higher mass values. Strange particle production was to form a separate investigation to be carried out after the analysis of pion production was completed.

Thus it was intended to investigate the following processes :-

$\pi^- p \rightarrow \pi^- p$	2.9		
$\pi^- p \rightarrow \pi^- p\, \pi^o$	2.10	two prong events.	
$\pi^- p \rightarrow \pi^- n\, \pi^+$	2.11		
$\pi^- p \rightarrow \pi^- p\, \pi^o + m\pi^o,\ m \geq 1$	2.12		
$\pi^- p \rightarrow \pi^- n\, \pi^+ + m\pi^o,\ m \geq 1$	2.13		

$\pi^- p \rightarrow \pi^- p \pi^+ \pi^-$	2.14	four prong events
$\pi^- p \rightarrow \pi^- p \pi^+ \pi^- \pi^o$	2.15	
$\pi^- p \rightarrow \pi^- n \pi^+ \pi^+ \pi^-$	2.16	
$\pi^- p \rightarrow \pi^- p \pi^+ \pi^- \pi^o + m\pi^o$, $m \geq 1$	2.17	
$\pi^- p \rightarrow \pi^- n \pi^+ \pi^+ \pi^- + m\pi^o$, $m \geq 1$	2.18	

In the two prong events, it would be possible to study elastic scattering (2.9), especially at small angles (small $|t|$) and compare results with the optical model and other predictions. Reactions 2.10 and 2.11 would provide data for the study of the one pion exchange model and $\rho^{\pm o}$ production and decay. Also, it was hoped to confirm the use of the Selleri formula in the region of the ρ^o-resonance, and extend its use to higher mass values in order to determine unambiguously the quantum numbers of the f^o meson. The unfittable reactions (2.12, 2.13) could provide information on the neutral decay mode of resonant states.

In the four-prong events, it was intended to study the production mechanisms of ω^o, ρ, η^o and $N^*(I = 3/2, J=3/2)$ in the light of the OPE model.

CHAPTER III

EXPERIMENTAL PROCEDURE

3.1 Introduction

A flow diagram of the experiment, typical of all bubble chamber experiments, is shown in Fig. 3.1. The 81 cm chamber was exposed to the 4 Gev/c negative pion beam from the CERN synchrotron. The film produced was scanned for all events in a selected fiducial region. Selected events were measured and geometrically reconstructed by computer in two stages. The first stage geometry programme, 'LINK', was performed on a Ferranti Mercury computer, and the output after conversion from paper tape through cards to magnetic tape, fed into the second stage programme 'GAP'. This latter stage together with the kinematics fitting programme, 'GRIND' were carried out on an IBM 7090 computer. The output was then analysed by a physicist, and if satisfactory, used for the calculation of further physical quantities associated with each event.

3.2. Pion Beam

Figure 3.2 shows the experimental arrangement used for the production of the 4Gev/c $\pi^{\pm}$ beam. Circulating protons of 20.1 Gev/c struck an internal beryllium target 38 mm. in length. Particles were accepted at an angle of $12\frac{1}{4}^{o}$ to the circulating beam, and into a solid angle of 5.9×10^{-5} steradian. They passed through a series of bending magnets, and magnetic quadrupoles, and arrived at the mass slit with a momentum dispersion of

1 Mev/c per centimetre. The electromagnetic separator was used only for the π^+ beam, and not for the π^- beam. The opening of the slit was 2cm, giving a momentum bite of $\pm$ 1 Mev/c. The angular spreads in the horizontal and vertical planes were respectively 1.3 and 1.4 milliradians at the mass slit, and 3 and 4 milliradians at the entrance to the bubble chamber. These angular spreads were checked during the experiment and will be disoussed below. From the measurement of many beam tracks on the film, the mean pion momentum was found to be 4Gev/c $\pm$ 10 Mev/c. The contamination of antiprotons was estimated at 1%, and the negative muon contamination from absorption measurements in lead determined to be 5%. The electron contamination was negligible.

3.3. 81 cm. Bubble Chamber.

A full description of the design and operation of the Saclay 81 cm. liquid hydrogen bubble chamber has been given elsewhere.(36) The chamber has dimensions of 81 x 40 x 32.0 cm^3. containing 127 litres of liquid hydrogen, and is expanded by a piston in contact with the liquid surface. The chamber was operated at a pressure of 75 psig. and a temperature of 27^oK. The magnetic field at the centre of the chamber was 10.7 kilogauss $\pm$ 0.2% and changed by $\pm$ 5% near the edge of the illuminated region. The pion beam entered the chamber through a 4mm. aluminium window (1.1 gm/cm^2) and, after a delay of 1 millisecond, three Xenon-filled flash tubes were discharged providing straight through illumination.

The illuminated volume thus provided was about 70 cm. in length (4.5 gm/cm^2), 28 cm. wide and 32 cm. deep. Three photographs were taken simultaneously by automatic cameras, with their objectives forming an equilateral triangle, C_1, C_2, C_3, in a plane one metre from the front glass of the chamber. The positions of the cameras relative to the chamber, and the co-ordinate system referred to in all future discussions are shown in Fig. 3.3. The photographs taken with the cameras $C_1C_2C_3$ will be referred to as view one, view two and view three respectively.

Fiducial markings etched on the inner surfaces of both front and back glasses provide reference points on the film for the spatial reconstruction of interactions in the chamber. The positions of these marks, six on the front glass and six on the back glass, are known with an accuracy of 10 microns.

3.4. Scanning Procedure.

Scanning was carried out on one of the British National Scanning tables. The magnification of the tables was such as to present a view of approximately chamber dimensions, and two views could be scanned simultaneously.

A total of 60,000 π^- photographs was obtained at a momentum of 4Gev/c The Imperial College group studied 5,000 of these. In order that good measurements of the tracks would be obtained, events were selected for measurement only if their apex fell inside a given fiducial volume (see

below).

The pion beam momentum was known to an accuracy much better than could be obtained from measurement. Hence it was only necessary to have a sufficient length of primary track to enable one to recognise it as a genuine beam track on the scanning table, and also to provide good measurements for the azimuthal and dip angles. Also, as the beam contamination of antiprotons was small, one could assume for all calculations that the incident track was a pion of the nominal beam momentum. Secondary tracks however should be as long as possible as the measuring error is inversely proportional to the square of the length of track measured. However, the higher the lower limit on length of track is set, the fewer will be the number of acceptable events and hence the higher the statistical error. In view of the above considerations, the fiducial volume chosen was such that the minimum beam length was 10 cm. and the minimum length of secondary track in the beam direction 30 cm. Secondary tracks scattered at large angles have in general lower momenta than those in the forward direction and also since the beam was well collimated, no length criterion was applied in the Y-direction. The fiducial region was defined by drawing on a scanning card, placed with respect to view 2, two lines parallel to the Y-axis. The lines were drawn through selected fiducial marks, for easy reference if ever the scanning table magnification was changed. This region, R_1, defines a trapezoidal scanning

volume in the chamber as shown in Fig. 3.3. A region R_2 was similarly defined further downstream to provide more statistics if required.

The scanning was carried out simultaneously on view two and the best other view. Two persons, one always a physicist, scanned the film from opposite ends of the scanning table, looking upstream and downstream of the beam. For cross-section purposes, a beam track count was made every tenth frame, and all blank and half-blank frame numbers recorded. An angular acceptance of 10 milliradians was set for deciding whether an incident particle was an acceptable beam track or not. This was the minimum angle which could be detected easily by eye on the scanning table, but measurements with calipers were made on all views when a deviation was seen.

All events with apices in regions R_1 and R_2 and originating from genuine beam tracks were recorded on scanning sheets. Scanners were trained to look for 0, 2, 4, 6, 8 prong events. The initial state, $\pi^- + p$, has zero charge, and so an equal number of positive and negative particles appear in the final state. The following information was recorded on the scanning sheets for each event:

(1) Scanners name.

(2) Event type and region.

(3) Frame number.

(4) Visual estimation of all positive secondary tracks.

The ratio of the ionization density of the track to that of the beam track was estimated.

(5) Stopping protons. If a positive track came to a definite end, a superposition of its end points from two views was made to see if the track stopped in the chamber liquid or went out of the front or back chamber windows.

(6) Stopping pions with subsequent $\pi^{\pm} \longrightarrow \mu^{\pm} \longrightarrow e^{\pm}$ decays.

(7) Knock-on protons produced by secondary neutrons. Again an end-point check was made to be certain the track originated from the chamber liquid.

(8) Associated electron-positron pairs, and Dalitz pairs.

(9) Secondary interactions.

(10) Charged and neutral V-particles.

(11) δ -rays on secondary tracks greater than 1 cm. diameter.

The ionisation density is a function of the velocity of a particle, and hence makes a very useful contribution in the identification of tracks (Section 4.3).

There exist well-known range-momentum relations for all particles (Fig. 3.4). For low-momentum tracks, the value of momentum obtained from the range far exceeds in accuracy that obtained from curvature measurements. This is particularly true for short stopping protons, when sometimes even

the sign of curvature is ambiguous from measurements.

Secondary neutral particles are indicated by associated knock-on protons (produced by neutrons) and e^+e^- pairs (indicating presence of one or more neutral pions).

Useful information enabling the identification of particles can in general be obtained from a study of δ-rays. The maximum energy transferred to an electron by collision is a strong function of the mass of an incident particle, and is given by (39):

$$E_{max} = \frac{2M_e P^2}{M_e^2 + M^2 + 2\ MeW} \simeq \frac{2M_e P^2}{M^2}$$

where M_e, M are the rest masses of electron and incident particles (Mev).

P is the momentum of the incident particle (Mev/c).

W is the total energy of the incident particle (Mev).

For 2 Gev/c protons, E_{max} is 4.4. Mev, corresponding to a δ-ray of 8 mm. diameter in the chamber, so that all 2Gev particles producing δ-rays with diameter greater than 1 cm. must be pions.

The film was scanned twice to enable scanning efficiences to be calculated. Only a record of the event type and frame number was made in the second scan. A third check scan was made to make a detailed scanning record of those events found in the second scan and not in the first scan.

Another purpose of the check scan was to find whether the reason for non-correspondence of events on first and second scans was a book-

keeping error, or a genuine random scanning loss.

When a final list of events had been obtained, twin photographic prints one of which was of view 2, were taken on the scanning table. The size of the image on the table was reduced to half chamber dimensions by using a 70 mm lens, so as to present two adjacent prints on a piece of 15" x 12" bromide paper. The scan sheets and prints were then attached to each other, and the tracks labelled by a physicist (Fig. 3.5).

These scan sheets then performed several functions, obvious from their format :

(1) Record of scanning information.

(2) Guide for measurer and bubble counter.

(3) Means of communication between physicists and measurers.

(4) Record of topology of event without referring back to scanning table.

3.5 Measurement of Events.

Two measuring machines were used for the measurement of the film. One, constructed at the College, has been used for other experiments, and a detailed description of it is given elsewhere [37]. The other, the British National Measuring machine, had its mechanical parts and electronics built commercially. The optics was designed and installed by the Technical Optics group of the College. Most of the film in the experiment was measured on the latter machine.

Measurement is achieved by digitising the movement of horizontal stages on one of which the film is clamped. The machine has two mutually perpendicular cast steel stages moving relative to each other and to a cast steel framework. The three views of the film are clamped on the X-stage, and the projection lenses on the Y-stage. Each stage is moved by a two-way hydraulic piston whose velocity is proportional to the appropriate component of a sine-cosine resolver, so that the resultant apparent motion of the film can be set by the operator. Relative motion between each stage and the frame is measured by a system designed by Ferranti Ltd., incorporating the principle of Moiré fringes. To both movable stage and fixed frame is attached a diffraction grating of the same line spacing (4μ), mounted in such a way to provide a small angle between the lines of the gratings. The transmitted light from a mercury lamp forms a band pattern at right angles to the bisector of this angle and the separation of the bands is a function of this angle. When the stage is moved by one line spacing, the resultant fringes move by one band spacing. This sinusoidal pattern of light falls on four photocells, which we used to sense the direction of motion of the stage, and to count on a binary scalar the number of bands passing them. One count of the digitiser corresponds to 2μ on the film or 20 μ in the chamber.

The mercury lamp is shone upwards through a selected view and the Y-stage projection lenses provide a moving image of the film on a circular

ground glass screen of 30 times magnification. Points of interest are brought to the central cross(arrow), so that their co-ordinates relative to an arbitrary origin can be measured. Another stationary chamber size (x10) image is produced by shining white light through other projection lenses attached to the X-stage.

The operator, brought the event of interest into view on the large stationary image for each view in turn by means of an automatic film transport system. The procedure was to measure three views for each event. The measurement of an event proceeded by measuring, an each view, four back glass fiducial marks, apex, and eight to ten points uniformly spaced along the track. The identification labels and co-ordinate pairs were output on five-hole paper tape. The identification labels consisted of event number, measurer's number, remeasurement number, date, view number, and for each track, track number and stopping point code.

3.6 Measurement Errors.

Several factors contribute to the accuracy of determination of the momentum of a charged particle. A track of curvature $\frac{1}{\rho}$, where ρ is the radius of curvature has a momentum p (electron volts) given by

$$p = 300\ H\rho$$

with ρ expressed in centimetres, and H in gauss. The uncertainty in the measurement of ρ comes from (1) measuring machine (2) bubble chamber (3) multiple Coulomb scattering.

Measuring machine errors arise in two ways: random point setting errors, and systematic errors due to non-linear stage movement. The former was found from repeated setting on a fiduciary to have a root mean square value of 4μ on the film. The systematic error was estimated for both the College machine and the British National machine by repeated measurement of the curvature of an 8 cm. long supposedly straight line placed parallel to the direction of travel of the stage. A value of curvature opposite in sign should be obtained on reversal of the line and remeasurement, if no distortion of the stage is present. The difference of these two sets of measurements indicated a systematic curvature corresponding to a sagitta of 15μ over 8 cm. or a momentum of 320 Gev/c for the College machine, and 0.5μ and 9600 Gev/c for the British National Machine.

The bubble chamber errors arise from liquid convection in the time between beam entry and the flash, and also optical distortion coming from both the optical components of the chamber and from the changes of refractive index produced by temperature gradients.

Since for high energy particles, multiple Coulomb scattering is negligible compared with the other errors, the mean uncertainty, Δs, in determining the sagitta of no magnetic field tracks, is caused only by measurement and instrumental errors. The momentum corresponding to this sagitta is known as the maximum detectable momentum of the experiment.

$$P_{MDM} = \frac{300\ HL^2}{8\ (\Delta s)}$$

This was measured only with the College machine and was found to be approximately 260 Gev/c for 55 cm. tracks. The displacement of the mean corresponded to a sagitta of 80μ i.e. systematic curvature correspondin to a momentum of 360 Gev/c. As this value of overall systematic distortion is of the same magnitude as the distortion of the College measuring machine, a reliable estimate of bubble chamber distortion alone could not be made. However, these measurements enabled a starting value of 75μ sagitta error to be set in the fitting programme. The validity of this was then examined on the basis of the χ^2 distribution obtained from the fits. (Section 4.2). If measurements of no-field tracks were made on the National machine, the low stage distortion would enable a good estimate of bubble chamber distortion to be made.

3.6. Geometrical Reconstruction.

The measuring machines provide co-ordinate measurements of tracks and apices for each of three views. The problem of reconstruction is to obtain from these measurements, the radiusof curvature, dip angle, azimuthal angle, with calculated errors, for each track. A knowledge of camera position, s, glass thicknesses, refractive indices, and fiducial mark positions, is required to set up a reference frame for the reconstruction.

This reference frame is set up by finding the apparent position on the outside of the front glass, of each of the fiducial marks as seen from each view. For each view in turn transformation coefficients are found relating the measuring machine co-ordinates of the fiducial marks to their apparent position on the front glass. Four fiducial marks were measured on each view to allow for differential film shrinkage in the X and Y directions. A check is also made to see if the fiducial marks have been measured to within a given tolerance. The transformation coefficients are then used to construct light ray equations for each measurement pair (x-y co-ordinates), and by intersection of light rays from corresponding points, space points are calculated.

A first approximate helix is found using two selected views only. This is then used as a starting point to do a least squares fit with measurements on all views and so find the best helix. No account is taken of the change in curvature of the tracks due to multiple scattering and energy loss. After all the tracks in an event have been reconstructed, the apex position is improved upon using the convergence of all tracks associated with the apex.

This geometrical reconstruction was carried out using two programmes written at CERN[38]. The data was first processed on a Mercury computer using the 'LINK' programme, which carried out the reconstruction up to the first approximation helix. This 'LINK' programme had two functions.

Firstly, it served to reject events with faulty information labels, badly measured tracks, apices and fiducial marks. Secondly, it served as a link between the measuring machine output and the required input format for the GAP programme. The output contained the measured co-ordinates of tracks and points for successful events, and a list of rejected events with reasons for failure.

The output from LINK was first converted into cards by an IBM 046 and then into magnetic tape using an IBM 1401. The full least squares helix fitting was then carried out using the GAP programme, run on an IBM 7090. The output from GAP contained the following quantities (1) XYZ co-ordinates of each apex (2) Radius of curvature at the centre of the track; dip angle and azimulhal angle at the apex. Associated errors were also printed out.

The percentage of successful events to pass through the complete process from measuring machine to GAP varied considerably. Bad labelling and measurements were responsible for many failures, but many more were often caused by faulty punching of paper tape during the production of the LINK output.

3.8. Kinematics Fitting.

With the knowledge of the magnetic field inside the chamber, the momentum of each track can be obtained directly from the GAP geometry output. If masses are then assigned to each of the particles, and

provided there is not more than one neutral particle, in the interaction, all kinematic quantities can be calculated. However, because of measuring errors or incorrect mass assignments, these kinematic quantities will not in general simultaneously satisfy energy and momentum conservation at the vertex. By applying four-momentum conservation at each vertex the number of constraint equations is equal to four times the number of vertices. In this experiment however, only single vertices are used, and hence four constraint equations are available. Each track is characterised by three variables :

$1/_p$, where p is the momentum

λ , the dip angle

ϕ , the azimuthal angle, and so only one missing neutral particle can have its variables calculated. Hence the problem of calculating momenta, energies for all particles is over-determined with four degrees of freedom (ND=4) with no missing neutrals, and one degree of freedom with one missing neutral. (ND=1).

Hence it is possible to adjust the momenta and angles at the vertex to conserve energy momentum in such a way as to minimise the χ^2 function of the adjustments by an iteration procedure.

$$\chi^2 = \sum_{ij} (x_i - x_i^m)\, G_{ij}^{-1}\, (x_j - x_j^m)$$

where

x_i^m are the measured values of $\frac{1}{p}, \lambda, \phi$

x_i are the adjusted values of $\frac{1}{p}, \lambda, \phi$

G_{ij}^{-1} is the inverse error matrix.

The χ^2 is minimised subject to the constraint

$$F(x_i) = 0$$

by the method of Lagrangian multipliers. Thus the value of χ^2 represents the amount of adjustment relative to the uncertainties and hence is a measure of the goodness of the fit. A number of tests are applied at each stage of, and at the end of the iteration. At each stage χ^2 must be positive and less than a specified value. Also the magnitude of the residuals term of each constraint equation had to become zero within set tolerances and the end of the iteration.

The CERN GRIND Kinematics fitting programme [38] is used to carry out this fitting routine. The output from GAP, together with a variety of mass assignments (hypotheses), a table of magnetic field values and range energy tables constitute the input to GRIND.

External errors, inserted in the programme to represent chamber distortion (75μ on the sagitta over a length of 60 cm), are compared with the reconstructed errors from GAP to decide if a track variable is satisfactorily measured. If the geometrical reconstruction error is less

than the external error, the external error is used in GRIND. If the reconstruction error is greater but not more than three times greater than the external error, the track is considered to be well-measured. If the reconstruction error is more than three times greater but satisfactory convergence is obtained, the track is considered to be badly measured. If, however, no convergence in the iteration is obtainable, the variable is considered to be unmeasured, and a constraint equation is used to determine it. Of course, very badly measured tracks are normally failed in LINK.

A common source of a badly measured or unmeasured momentum, is a very short stopping proton. However, there is a facility in GAP to bypass the helix fitting procedure, and reconstruct the track as a straight line. GRIND then uses range-energy relations to calculate its momenta. A weighted average of momentum from curvature measurement and range measurement is generally used for stopping points.

For successfully fitted hypotheses, GRIND outputs the mass, momentum, dip and azimuthal angle of each track, at the vertex, together with fitted and unfitted errors. Effective masses and centre of mass quantities for various combinations also appear on the output. For each hypothesis tried, a summary is given, showing the χ^2, probability of obtaining this χ^2 or greater, and the fault code if a fit was not obtained. Also printed for each hypothesis are the missing momenta and masses with associated errors.

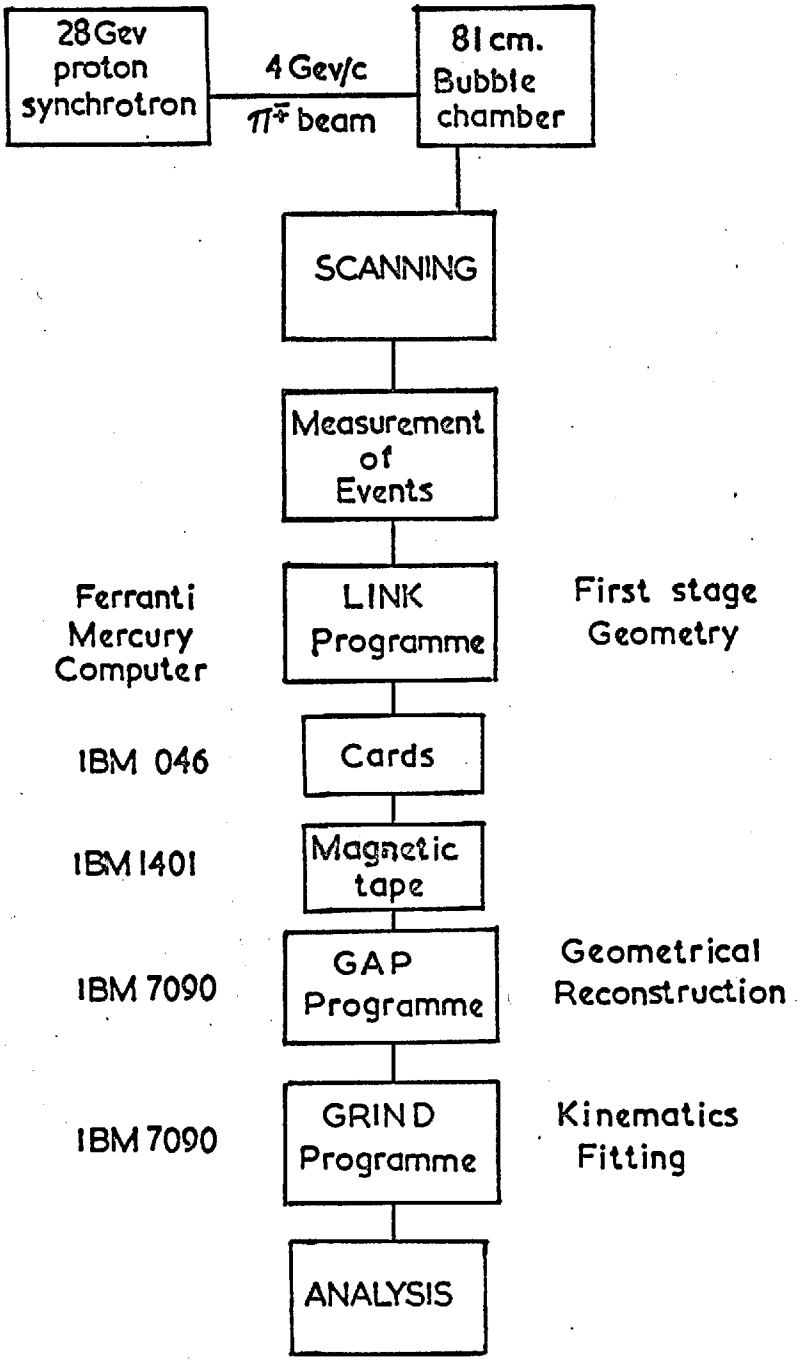

FLOW DIAGRAM OF EXPERIMENT

Fig. 3.1

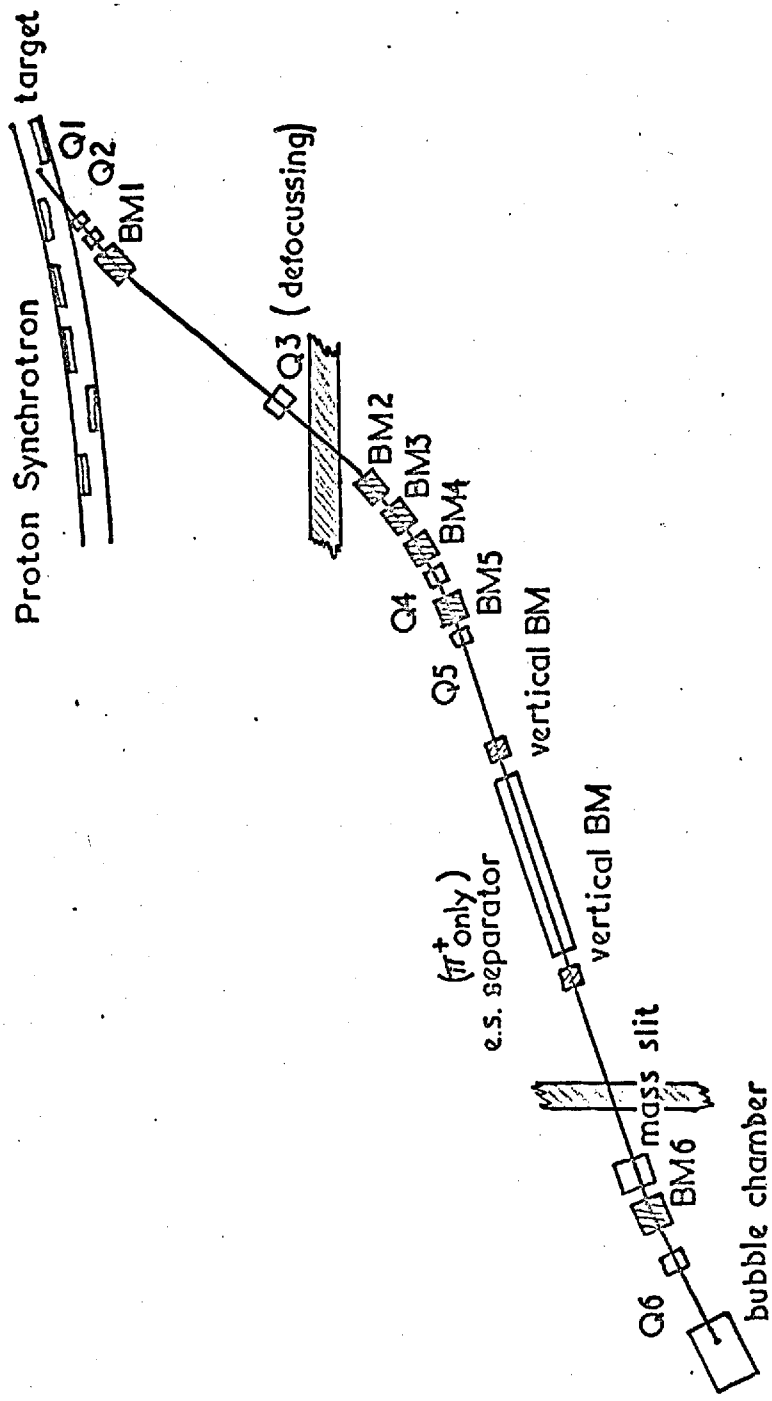

4 Gev/c $\pi^{\pm}$ beam

Fig. 3.2

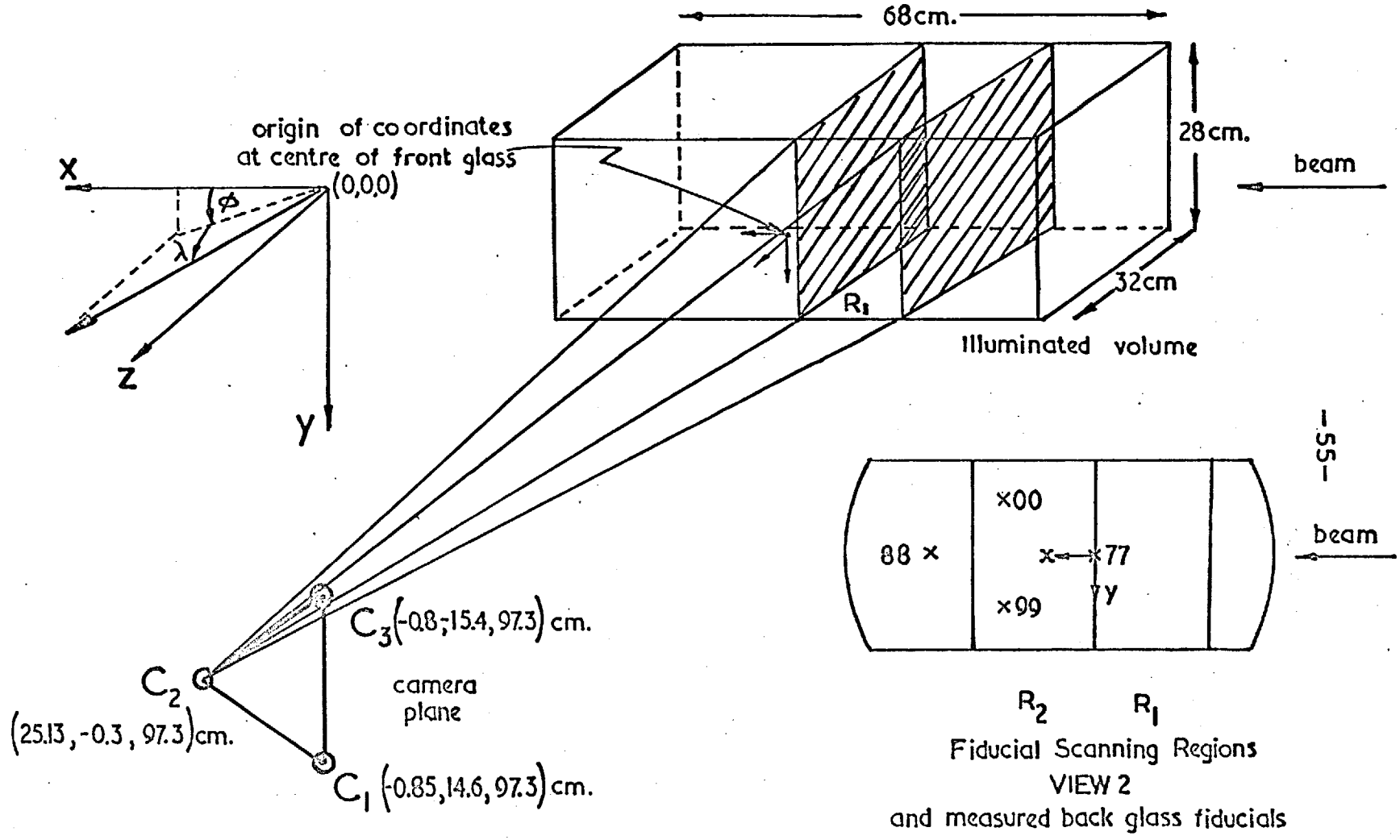

81cm. CHAMBER GEOMETRY

Fig. 3.3

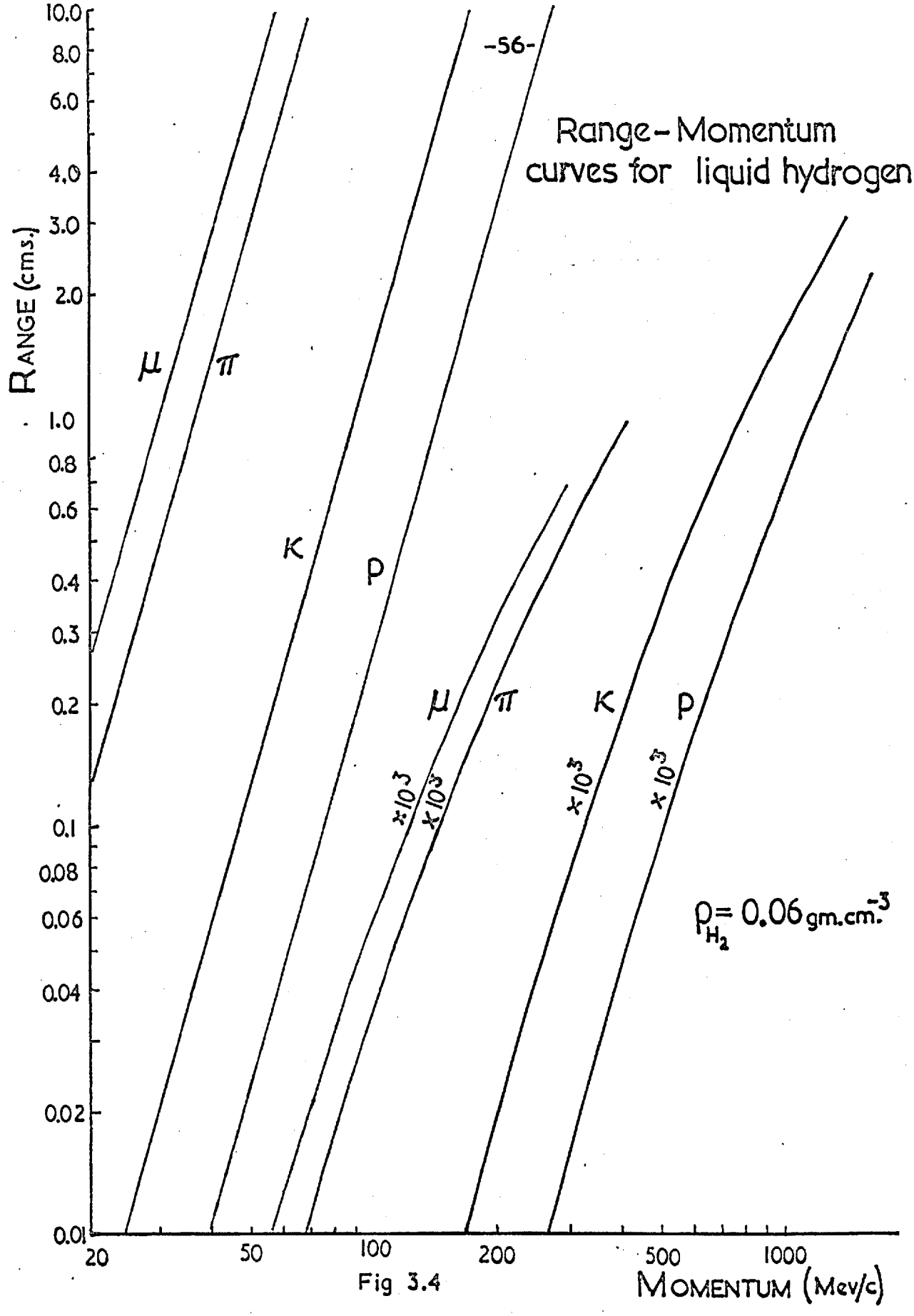
Range-Momentum
curves for liquid hydrogen
RANGE (cms.)
10.0
8.0
6.0
4.0
3.0
2.0
1.0
0.8
0.6
0.4
0.3
0.2
0.1
0.08
0.06
0.04
0.02
0.01
μ
π
K
P
μ
π
K
P
x10³
x10³
x10³
x10³
ρ_H2 = 0.06 gm.cm.⁻³
20
50
100
200
500
1000
MOMENTUM (Mev/c)

Fig 3.4

Experiment - 4 Gev π⁻ Event type 2 P Event No 445592

Scan Information

Re Scanner	V°	V⁻	V° ep	KOP	s.p	π,e	S⁻	S°	δ	Vis A2	Estimation A	A
1	M A									2		

Ionization Density

Track	Started By	Finished By	n_1	n_2	n_3	n_4	n_5	N_1	N_2	N_3	N_4	N_5	p (GeV)	λ	$g_c \pm \Delta g_c$	$\frac{m}{m_0} \pm \Delta\frac{m}{m_0}$	$V_c \pm \Delta V_c$	Theor Value π	Theor Value p	IDENTITY
beam	9.4.63		5578	5245	5139	3674	7774													
	VJ	VJ	5437	5015	5608	3632	7738	530	439	209	78	36								
			141	230	131	42	36													
A2	9.4.63		5437	5015	5608	3632	7738													
	VJ	VJ	5281	4896	5581	3628	7738	306	150	31	4	-	0.89	-0.45		1.95 ± 0.2	1.7 ± 0.5	1.02	2.17	proton
			156	119	27	4	-													
A																				
A																				

Measurement Routine

Track	View 1	View 2	View 3	Special Instructions	Meas. Machine	Started by	DATE	Finish by	Measurer's Comments
A1	×	×	×	Meas		MR	11-3	MR	
A2	×	×	×	ReMeas		Q	28-3	Q	V3 ? to spec of A1 measured.
A3	×	×	×	ReM					
A4									
A5				ReM					
A6				ReM					
A7				ReM					

SCAN SHEET

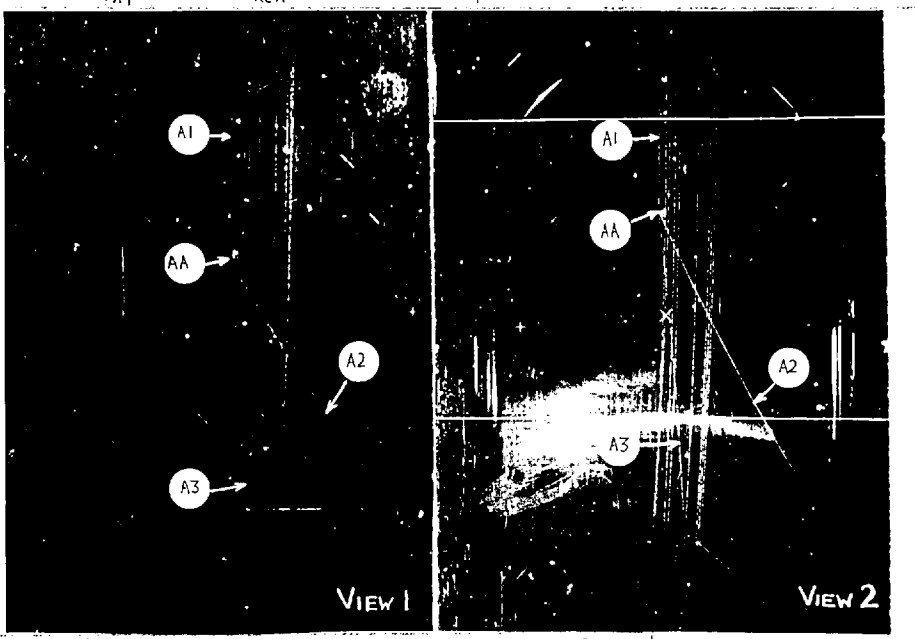

Fiducial Scanning Region

Geometry

Date	A1	A2	A3	A4	A5
26 MAR 63	WWW	WWW	WWW		
GAP					

Scan Information

V°	V⁻	V° ep	KOP	s.p.	π,e	S⁻	δ	Particle Identity	A 2 Ident	A 2 Method	A Ident	A Method	A Ident	A Method
									P	B.C.				

Final Identity
$\pi^- p \pi^0 (\pi^0)$

KIN SHEET

Kinematics Fitting

Date :- 26 MAR 63

Fitted Hypotheses		Other Fits suggested	
Non-c.m	c.m	Non-c.m.	c.m
GRIND		$\pi^- p \pi^0 \pi^0$	
		$\pi^- n \pi^0 \pi^0$	

Experiment 4 Gev π⁻ Event type 2P Event No 445592

Fig. 3.5

CHAPTER IV

INTERPRETATION OF EVENTS

The analysis of both two and four-prong events was undertaken simultaneously, but as the analysis of the latter has appeared elsewhere, the discussion in this and subsequent chapters will be limited to two prongs only.

4.1. Interpretation of Events by Kinematics Programme

The following hypotheses were tested by the GRIND fitting programme

$$\pi^- p \longrightarrow \pi^- p \qquad 4.1.$$

$$\pi^- p \longrightarrow \pi^- p \pi^o \qquad 4.2.$$

$$\pi^- p \longrightarrow \pi^- n \pi^+ \qquad 4.3.$$

A fitted hypothesis was accepted if its χ^2 was less than a cut-off value. This value was set to correspond to a probability of 1/1000 of rejecting a correct hypothesis. Thus a χ^2 cut-off of 20 was used for those events without a neutral particle, i.e. four degrees of freedom, and $\chi^2=10$ for those events with one missing neutral, i.e. one degree of freedom. All acceptable fits were recorded on a KIN sheet for the event (FIG. 3.5).

Frequently, the event could not be fitted to a tried hypothesis. An indication of the reaction could then be obtained from the missing variables

calculated from the measured quantities.

$$\vec{p}_N = \vec{p}_1 - \sum_i \vec{p}_i \qquad 4.7$$

$$E_N = E_1 + M_p - \Sigma E_i \qquad 4.8.$$

$$M_N^2 = E_N^2 - \vec{p}_N^{\,2} \qquad 4.9$$

where E_N, $\bar{p}_N$, M_N^2 , are the energy, momentum and effective mass squared carried by the missing neutral particles.

E_1, p_1 are the energy, momentum of incident pion

E_i, p_i are the energy, momentum of visible secondaries.

M_p is the rest mass of the proton.

The minimum effective mass squared carried by two neutral pions is 0.073 Gev^2; and by a neutron and pion, 1.15 Gev^2. Thus, if, for a given hypothesis, the corresponding M_N^2 was greater than, or less than but within three standard deviations of one of these values, the event was classified as possibly one of the no-fit hypotheses;

$$\pi^- p \longrightarrow \pi^- p\, \pi^o + m\, \pi^o \quad ; \quad m \geq 1$$

$$\pi^- p \longrightarrow \pi^- n\, \pi^+ + m\, \pi^o \quad ; \quad m \geq 1$$

4.2. Consistency Tests.

The spread of the beam momentum as determined from the beam design

was $\pm$ 20 Mev/c. As the measurement errors on short beam tracks are considerably larger than this, the nominal 4 Gev/c with its above nominal error were used for GRIND. The measurements of 60 full length beam tracks yielded a corrected value for $\frac{1}{\rho}$ of $(0.001558 \pm .000024)$ cm^{-1}, corresponding to 3.99 $\pm$.06 Gev/c.[42] A combination of measurements from all groups gave a mean value of 4.0 Gev/c and spread of $\pm$ 15 Mev/c.

The fitted beam momentum for all accepted fitted events is shown in Fig. 4.1, and its mean value is seen to be 3.992 Gev/c with a standard deviation of $\pm$ 15 Mev/c. This shift to a lower momentum could indicate that the beam momentum was less than 4.000 Gev/c, or simply that systematic biases cause underestimation of all reconstructed momenta.

The angular distributions of beam tracks, obtained from the study of 500 events, are shown in Figs. 4.2 - 4.3. The distributions give the following values, measured in radians

$$\phi = 3.112 \pm 0.010 \quad \text{reduced to } x_a = -28 \text{ cm.}$$

$$\overline{\Delta\phi} = 0.0015$$

$$\lambda = 0.008 \pm 0.012$$

$$\overline{\Delta\lambda} = 0.003$$

where the errors quoted on ϕ, λ are the half-widths at half maximum, and $\overline{\Delta\phi}$, $\overline{\Delta\lambda}$ are mean values of the error distribution. The mean error, $\overline{\Delta\lambda}$ is about twice the magnitude of $\Delta\phi$, as the measurement of λ involves measurements in the z direction. The real spread on ϕ, λ is thus about $\pm$ 0.010 radians due to a combination of inherent beam spread and multiple

Coulomb scattering in the chamber wall. The latter, calculated for an aluminium wall thickness of 1.0 cm, gives a root mean square angle.(39)

$$\langle\theta\rangle = \frac{E_s}{\beta p}\sqrt{\frac{x}{X_o}} \sim 0.002 \text{ radians}$$

where x is the wall thickness = 2.5 gm. cm^{-2}

X_o is the radiation length for Al = 25 gm.cm^{-2}

E_s = 21 Mev

p is the momentum of incident pion = 4000 Mev

$\beta \simeq 1$

Thus, the spread is almost entirely due to inherent beam spread of $\pm$ 0.010 radians, or about three times the quoted design value.

The difference in the shape of the ϕ and λ distribution is due to the imposed beam scanning criterion for azimuthal angle. By comparison with the λ distribution, it appears that events were rejected unnecessarily and a criterion of $\pm$0.02 radians would have been better.

The distributions of apex positions in x,y,z are shown in Fig.4.4. The x distribution reflects the chosen fiducial volume. The y and z distributions show that the beam is well centred in the chamber. The mean values and widths (half-maximum) are :-

$$\bar{y} = 0.72 \pm 2.0 \text{ cm.}$$
$$\bar{z} = -18.3 \pm 2.5 \text{ cm.}$$

To check that events were correctly interpreted by the fitting programme, missing mass squared distributions were plotted for each class of fit. They are shown for events of the type $\pi^- p \to \pi^- p$, $\pi^- p \to \pi^- p\, \pi^o$ and $\pi^- p \to \pi^- n\, \pi^+$ in Figs. 4.7 (a) - (c). Figs 4.8(a)(b) show the distributions for the 'no-fit' events $\pi^- p\, \pi^o (m\pi^o)$ and $\pi^- n\, \pi^+ (m\pi^o)$. The distributions for fits and no-fits are seen to be quite well separated, indicating that the measurements were sufficiently good.

The χ^2 distributions found for each fit are shown in Figs. 4.5 (a) - (c). Theoretical χ^2 distributions are superimposed and show reasonable agreement with the data within the statistics. Also shown in Fig. 4.6 is the distribution of the associated probability function $P(\chi^2)$, plotted for all fits together,

$$P(\chi^2) = \int_{\chi^2} f(\chi^2)\, d\chi^2$$

$f(\chi^2)$ is the normal χ^2 distribution function.

which should be flat if the correct errors have been used in the fitting programme. The slight peaking at low probabilities comes from the acceptance of several high χ^2 elastic events. These events had a χ^2 outside the cut-off value, but were accepted as elastic since all the missing quantities were zero, and had an identifiable proton. Otherwise the shape of the probability distribution is flat.

4.3. Identification of tracks by Ionisation Density Measurement.

Measurement of the bubble densities of positive tracks was used to distinguish between positive pions and protons where fitting alone was ambiguous.

The number, n, of knock-on electrons produced per gm cm^{-2} path of an ionizing particle, with energies between E_{min} and E_{max} can be shown to be (39).

$$n = \frac{2\pi N_A Z}{A} \quad \frac{e^4}{m_e c^2} \cdot \frac{1}{\beta^2} \left(\frac{1}{E_{min}} - \frac{1}{E_{max}} \right)$$

where N_A is Avogadro's Number

m_e , e are the mass and charge of electron

Z, A are the atomic number and mass number of the ionised material.

and $E_{max} \gg E_{min}$

It has been reported by several experimenters that, over a wide range of chamber operating conditions, track bubble densities are inversely proportional to β^2. This fact suggests strongly that the energy required for bubble nucleation originates from the energy transfer by the particle to the scattered electrons, which then stop in the chamber.

The track bubble density, m, has been shown to depend also on the thermodynamic condition of the chamber. Kenney et al., (41) measured proton

tracks under carefully controlled conditions in the 20" Shutt bubble chamber. The pressure superheat dependence $\frac{1}{m}\frac{\Delta m}{p_s}$ was found to be ~10% /psia, and temperature dependence $\frac{1}{m}\frac{\Delta m}{\Delta T} \sim$ 5-15% /0.1°K. In principle, then, a knowledge of the dependence of bubble density on chamber operating conditions should make it possible to normalise measurements of track density on each frame to standard chamber conditions. However, for the present experiment in the 81 cm chamber, these conditions were not known for each stereo-frame, and it was necessary to compare the ionisation of each track with a minimum ionising beam track.

There are in general three methods of determining bubble density; bubble counting, gap counting, and a determination of the mean gap length. The first two methods have difficulties due to bubble image coalescence and personal error corrections have to be applied. A mean gap length method was used in this experiment to avoid this overlap correction.

The number of gaps, dN, of length between x and x+dx, is given by (40)

$$dN = K\, e^{-x/g}\, dx$$

where g is the mean gap length, K a constant . If one imposes a lower fixed limit on gap lengths, x_o, below which bubble image coalescence becomes important, the observed number with length greater than x_o is

$$N_o = \int_{x_o}^{\infty} K e^{-x/g}\, dx = Kg\, e^{-x_o/g}$$

The number with length greater than X is therefore

$$N_{(x)} = \int_{x}^{\infty} Ke^{-x/g}\, dx = No\, e^{(x-x_o)/g}$$

or $$\log_e N_{(x)} = x\left(\frac{1}{g}\right) - \frac{x_o}{g} + \log_e N_o.$$

Thus a plot of $\log_e N(x)$ against x has a slope of $1/g$, equal to the track density, m.

Measurements were made with a microscope by moving the film stage across the field of view of a graticule mounted in the eyepiece. This graticule consisted of five concentric circles of radii $x_o, 2x_o, 4x_o, 6x_o$, and $8x_o$. The centre of each bubble was successively brought to the centre of the circles, and the position of the adjacent bubble relative to the circles recorded on one of five relay counters. Gaps in the vicinity of crossing tracks or in any way obscured, were omitted, as were gaps that fell inside the cut-off value, x_o. In this way the number of gaps greater than each circle radius could be determined, and the mean gap length determined by a plot of N(x) against x on logarithmic linear paper. (Fig. 4.10).

The determination of the gap length x_o, below which the gap length distribution departs from its exponential form, is important if systematic errors due to overlap are to be avoided. Use of gap lengths so small that

large numbers of such gaps are not detected leads to an underestimate of track density, the importance of which increases with increasing track density. However, the use of a too large value of this cut-off parameter throws away valuable information, and limits the statistical accuracy of the measurement $\left(\frac{1}{\sqrt{N_o}}\right)$.

An optimum value of x_o was difficult to find due to a large variation of densities caused by fluctuating chamber conditions. A value for x_o of 1.1 bubble diameters (300μ in the chamber) was initially used, but from the plots, a depression of the most significant point($N(x_o)$) was often seen. The value of x_o was altered to 1.4 bubble diameters, and for the majority of measurements, a satisfactory linear plot was obtained. In the early part of the experiment, a weighted least squares fitting programme was used to determine g from the measured points. This proved unsatisfactory since it gave an underestimate of g if the most significant point was depressed.

Before comparison of the measured bubble density, with the theoretically expected value, a correction for dip angle was applied. The true demagnification factor from the chamber to film is given by:

$$\frac{\delta g'}{\delta g} = \frac{z_o - z_2}{z_2 - z} \left[\frac{\left(1 + \frac{x-x_2}{z_2-z} \tan\lambda \sec\phi\right)^2 + \tan^2\phi\left(1 + \frac{y-y_2}{z_2-z} \tan\lambda \operatorname{cosec}\phi\right)^2}{1 + \tan^2\phi + \tan^2\lambda \sec^2\phi} \right]^{\frac{1}{2}}$$

where $\delta g'$, δg are infinitesimal lengths of track on the film and in the chamber.

(x,y,z) are chamber co-ordinates of point on track

(x_2,y_2,z_2) are camera co-ordinates

λ, ϕ are dip and azimuthal angles

z_o is z-co-ordinate of the film plane

If assumptions are made that (a) the beam track used for normalisation has the same z-co-ordinate as that of track and (b) the centre of the track is on the axis of the camera, ie. $x = x_2$ $y = y_2$, the correction factor for (g/g_o) reduces to $\sec\lambda$, where g_o is the mean gap length for the beam track. For this reason, the measurements of gap length were always made on view 2, the camera axis on this view being most normal to the centre of the tracks, and the beam track chosen as near as possible to the track. Visual estimations were also made on view 2 for the same reason. The validity of these assumptions and the reliability of the measurements in general was checked by comparing the obtained corrected relative density $\frac{m}{m_o}$ with the expected value for particles positively identified from the kinematics fitting programme.

The measured relative ionisation densities were then compared with the expected value given by

$$\frac{m}{m_o} = 1 + \frac{M^2}{p^2}$$

which are plotted in Fig. 4.9. If $(\frac{m}{m_o})$ differed by more than three standard deviations from the expected value for a proton, say, then the track was considered not to be a proton. If the measurement lay within three standard

deviations of both proton and pion, then the nature of the particle was considered as undecided.

4.4. Efficiency of Methods used for Identification of Events.

Out of all the two prong events tested by the GRIND kinematics fitting programme, only about 25% were unambiguously identified. The remainder were identified from the ionisation densities of the positive particles.

At momenta below 100 Mev/c, proton and pion tracks are very dense and cannot be distinguished. However, at these low momenta, both pions and protons stop in the chamber, the former with its characteristic $\pi^+ \rightarrow \mu^+ \rightarrow e^+$ decays, and range-energy relations allow an unambiguous identification to be made. Identification from visual estimation was possible up to 750 Mev/c, and this allowed the complete interpretion of another 40% of all two prong events. Systematic bubble density measurements covered the range 750 Mev/c to 1800 Mev/c, although this upper limit was lower when the dip angle became appreciable. For dip angles $\lambda > 50^\circ$, no reliable ionisation estimates were possible, although events with positives having large dip angles were usually already unambiguously identified from fitting. Above 1800 Mev/c, it was impossible to distinguish between pion and proton by ionisation, and, unless unambiguously identified by fitting, these events were classed as ambiguous (see next section). For four events, the presence of a large δ-ray on positives with momenta 2 to 3 Gev/c, enabled identification to be made, but other scanning information generally

provided only confirmatory evidence for an already identified event. In 1% of all two prong events, contradictory decisions were obtained from the fitting programme and from the identity of positives. In these cases, the events were regarded as unclassified.

If the fitting programme had been the only source of information, mistakes in identification would be made by choosing the fit with the smaller χ^2. If this was done for the 290 fitted two prong events, 28 events or 10% would have been wrongly classified. If, however, a fit is only accepted if its χ^2 is an order of magnitude lower than the others, a mistake would be made for only 2% of all events. If this reliance were placed on the fitting procedure, ionisation densities would only be required for 15% of the events.

4.5. Biases and Ambiguities.

The only significant scanning bias was the loss of elastic events at small scattering angles. The correction for these lost events will be discussed in the next Chapter.

About 5% of all events failed to pass through the geometry programme in spite of repeated measurements. A significant proportion of these was due to overlapping beam tracks causing bad apex measurements or non-convergence of the primary track during reconstruction. Some events were passed successfully through the kinematics programme by fixing all three beam track variables (p, λ, ϕ) with errors equal to the spread of the distributions. A successful helix fit could often not be obtained for

highly curved tracks (e.g. $\pi\mu e$) or steeply dipping tracks. Events with secondary scatters often had an immeasurable track length.

Apart from bad geometry events, 7% of the events from a total of 595 analysed, were ambiguous between two reaction channels, as they had positives with momenta in excess of 1.7 Gev/c. Of these, half were ambiguous between the no-fit reactions $\pi^- p \rightarrow \pi^- n \pi^+ + m\pi^0$, $m \geqslant 1$, and $\pi^- p \rightarrow \pi^- p \pi^0 + m \pi^0$, $m \geqslant 1$, and were divided equally between the two channels. More serious was that 25% of the events which gave a fit to reaction $\pi^- p \rightarrow \pi^- n \pi^+$ were also kinematically consistent with $\pi^- p \rightarrow \pi^- p \pi^0 + m \pi^0$, $m > 1$. These have been classified as due to the reaction $\pi^- p \rightarrow \pi^- n \pi^+$, and the effective mass distributions resulting from these particular events agree with those resulting from the completely unambiguous events (Fig. 6.10).

4.6. Combination of data from different groups.

Although the criteria for identifying events were the same for all groups in the collaboration, some details varied from group to group. To check the consistency of measurement and analysis of data among the groups, 20 test events were measured, computed and analysed by each group. The geometry and identification of the events were compared and excellent agreement was found. Branching ratios, χ^2, and missing mass distributions for each hypothesis were also compared with good agreement. Some groups had used a rather long fiducial volume (Fig. 4.11), specifying a minimum secondary length of 20 cm., rather than 30 cm, used by Imperial College.

The consequence of this was to broaden the missing mass distributions and cause some overlap between corresponding fit and no-fit events. The branching ratios for such groups show a higher FIT/NO FIT ratio than for Imperial College. Because of this, those events with apices at the end of the chamber (i.e. shortest secondaries) were removed before combination of the data.

Un-analysed events for the whole collaboration constituted 6% of the total number initially found, and because of the varied reasons for failure, it is believed that the combined results constitute an unbiased set, free from physical bias.

4.7. Cross-Sections.

In order to calculate the cross sections, it is necessary to know the true number of events in the fiducial volume of the chamber. If the true number of events of a particular type is N_i, and the scanning efficiences for first and second scans of finding this type of event are e_1 and e_2, then

$n_1 = N_i e_1$ is the no of events found in first scan

$n_2 = N_i e_2$ is the no of events found in second scan

$n_{12} = N_i e_1 e_2$ is the no of events common to both scans

The overall efficiency e is thus

$$e = 1 - (1-e_1)(1-e_2) = e_1 + e_2 - e_1 e_2$$

$$= \frac{n_{12}}{n_1 n_2} (n_1 + n_2 - n_{12})$$

For all two-prong events scanned at Imperial College

$$n_1 = 610 \ , \quad n_2 = 623 \ , \quad n_{12} = 585$$

$$e_1 = 0.93 \quad e_2 = 0.96 \ , \quad e = 0.997 \quad N_i = 656$$

The largest correction was that applied to elastic events, which had an overall scanning efficiency e of 93.5%. Elastic events were then also corrected for azimuthal loss (Section 5.1), giving $N_i = 670$.

The cross-section is then given by

$$\sigma_i = \left(\frac{A \ N_i}{N_A \cdot \rho \cdot \bar{l}} \cdot \frac{1}{N} \right) \times 10^{27} \text{mb.}$$

where A is the atomic number = 1 for hydrogen

N_A is the Avogadro's number = 6.03×10^{23} mols/gm.mol.

ρ is the density of liquid hydrogen at chamber operating conditions.

$\bar{l}$ is the length of fiducial volume at peak of beam z - profile.

N is the no of beam tracks scanned or (mean beam density x no of frames scanned).

For the Imperial College fiducial volume and two-prong data; $\bar{l} = 20.56$cm $N = 44.6 \times 10^3$., $N_{2_p} = 670$.

The following corrections were then applied :

(1) The pion beam had a 5% muon and 1% antiproton contamination.

(2) On the average, the primary particle of each event only travelled half-way through the fiducial volume. This reduces the interacting

length. $\bar{l}$, by about 1%.

The density of hydrogen, ρ , was obtained both from chamber operating conditions ($27^{o}K$ and 45 psi expanded pressure) and from a study of stopping $\pi^{+} \longrightarrow \mu^{+}$ decays. When a π^{+} meson stops in the chamber, it immediately decays into $\mu^{+} + \nu$ with subsequent $\mu^{+} \longrightarrow e^{+} + \nu + \bar{\nu}$. The unique μ^{+} energy (30 Mev) is determined from the kinematics of π-decay, and the range ($\sim$1cm) from measurements in the chamber. Thus the density is found from range-energy curves. The value found and used for ρ was 0.0625 $gm.cm^{-3}$.

The total cross-section thus obtained for Imperial College two prongs is 20.8 ± 0.8 mb.

The number of events analysed and the corrected corss-sections for the various channels are shown in the following tables, both for the Imperial College data (Table 4.1), and that of the whole collaboration (Table 4.2). Four prong cross-sections are also included for comparison. The total cross-section was calculated from all events found in the fiducial volume. All errors quoted are statistical.

Imperial College data Table 4.1

Channel	No. of events analysed	Corrected Cross-Section mb.
$\pi^- p$	144	5.75 ± 0.5 ≠
$\pi^- p \pi^o$	58	1.95 ± 0.3
$\pi^- n \pi^+$	92	3.05 ± 0.3
$\pi^- p \pi^o (\pi^o)$	97	3.3 ± 0.3
$\pi^- n \pi^+ (\pi^o)$	202	6.8 ± 0.6
TOTAL 2-prong	595	20.8 ± 0.8
$\pi^- p \pi^+ \pi^-$	50	1.8 ± 0.3
$\pi^- p \pi^+ \pi^- \pi^o$	63	2.25 ± 0.3
$\pi^- n \pi^+ \pi^- \pi^+$	23	0.85 ± 0.2
$\pi^- p \pi^+ \pi^- \pi^o (\pi^o)$	28	0.95 ± 0.2
$\pi^- n \pi^+ \pi^- \pi^+ (\pi^o)$	47	1.65 ± 0.3
TOTAL 4-prong	211	7.5 ± 0.5
TOTAL	-	31.6 ± 1.2

Combined data Table 4.2

Channel	No. of events analysed	Corrected Cross-sections mb.
$\pi^- p$	1083	6.62 ± 0.22
$\pi^- p \pi^o$	446	2.21 ± 0.10
$\pi^- n \pi^+$	636	3.16 ± 0.13
$\pi^- p \pi^o (\pi^o)$	538	2.67 ± 0.12
$\pi^- n \pi^+ (\pi^o)$	1125	5.57 ± 0.17
Total 2-prong	3828	20.23 ± 0.30
$\pi^- p \pi^+ \pi^-$	542	1.91 ± 0.08
$\pi^- p \pi^+ \pi^- \pi^o$	606	2.11 ± 0.09
$\pi^- n \pi^+ \pi^- \pi^+$	315	1.10 ± 0.06
$\pi^- p \pi^+ \pi^- \pi^o (\pi^o)$	244	0.85 ± 0.06
$\pi^- n \pi^+ \pi^- \pi^+ (\pi^o)$	421	1.47 ± 0.07
TOTAL 4-prong	2128	7.44 ± 0.17
TOTAL inc.6-prong & strange-particle		32.3 ± 0.7

≠ Uncorrected for small t loss, due to small statistics.

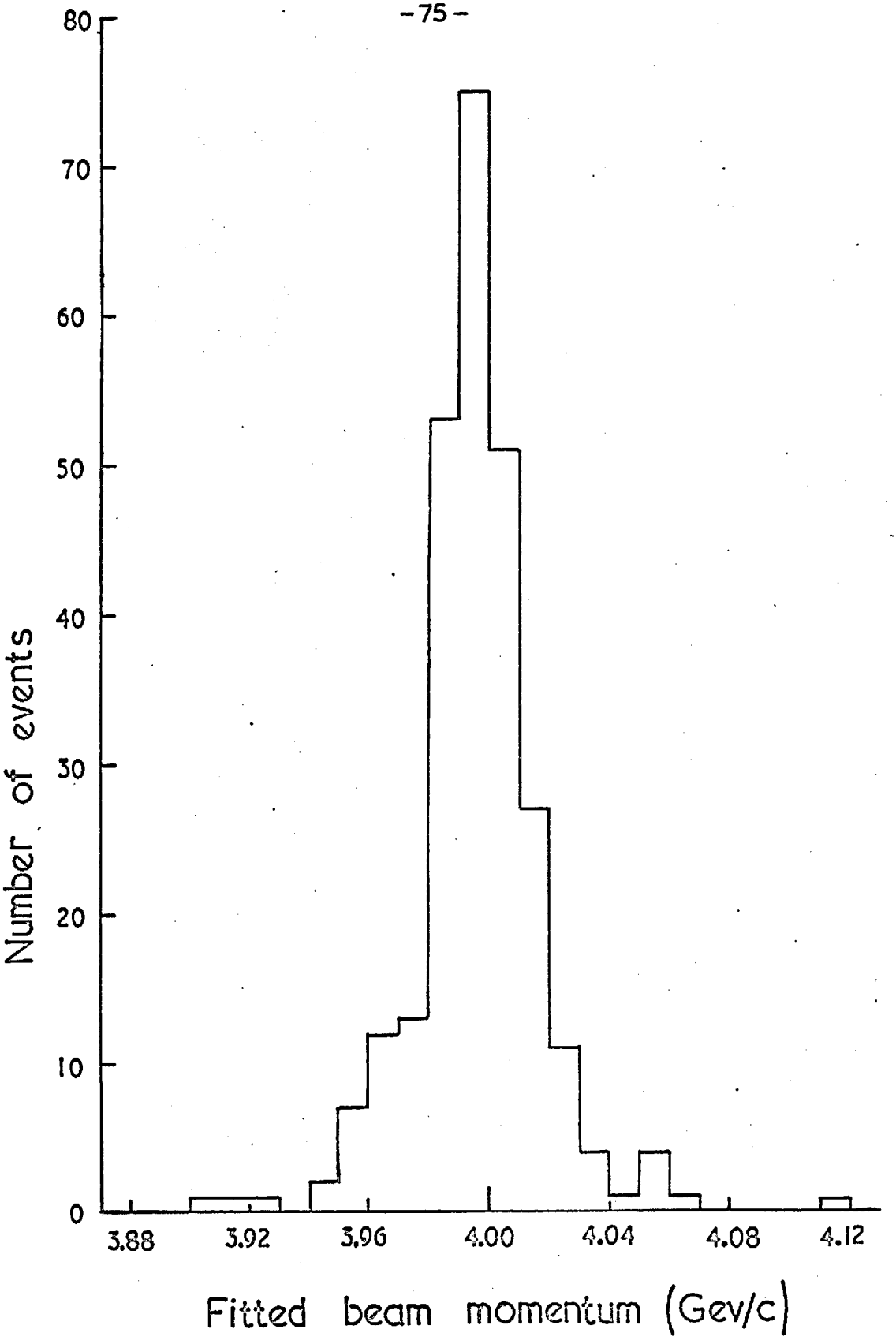
80
70
60
50
40
30
20
10
0
Number of events
3.88
3.92
3.96
4.00
4.04
4.08
4.12
Fitted beam momentum (Gev/c)

Fig. 4.1

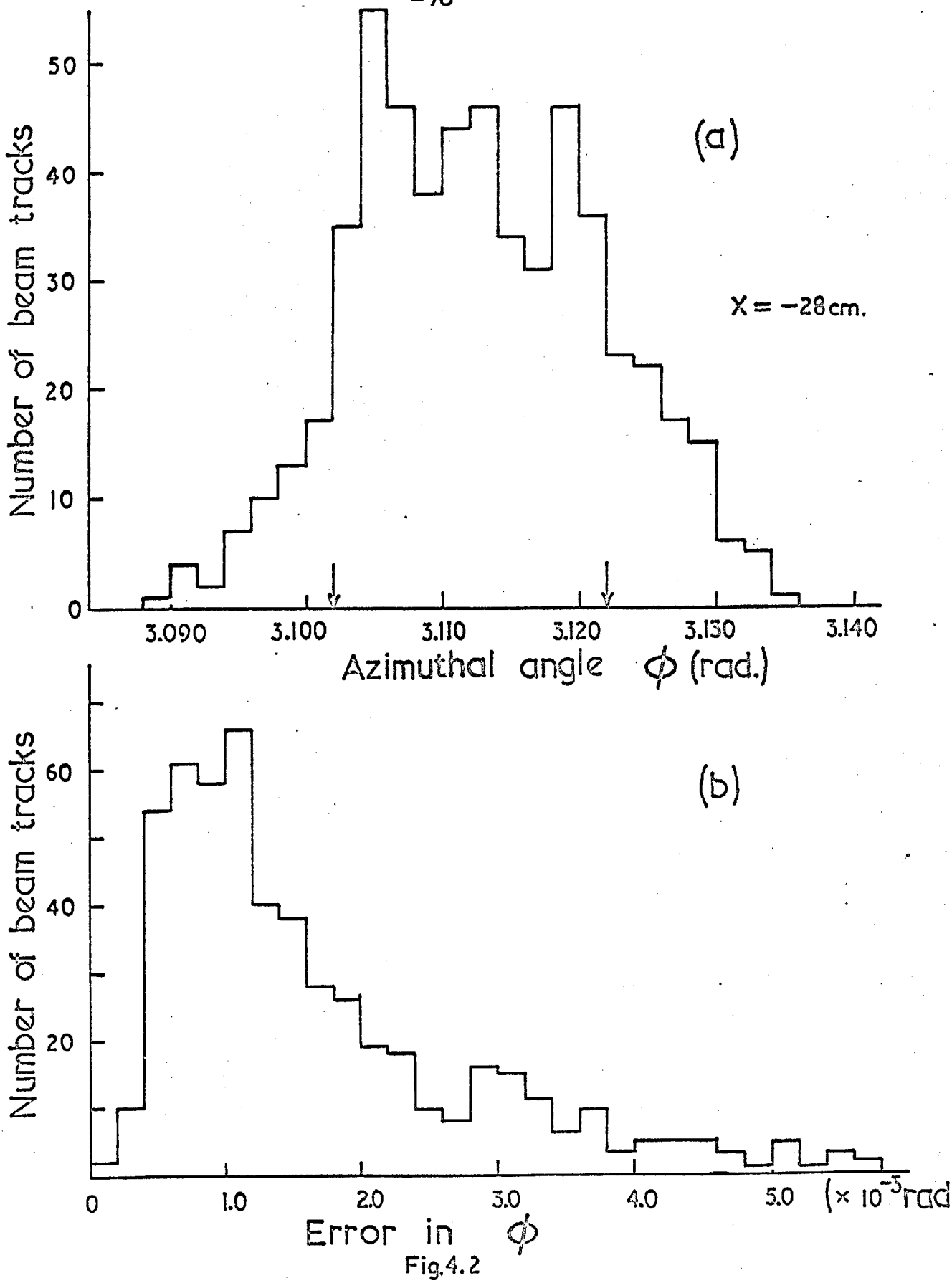
(a)
X = −28 cm.
Number of beam tracks
0
10
20
30
40
50
3.090
3.100
3.110
3.120
3.130
3.140
Azimuthal angle φ (rad.)
(b)
Number of beam tracks
0
20
40
60
1.0
2.0
3.0
4.0
5.0
(× 10⁻³ rad.
Error in φ

Fig.4.2

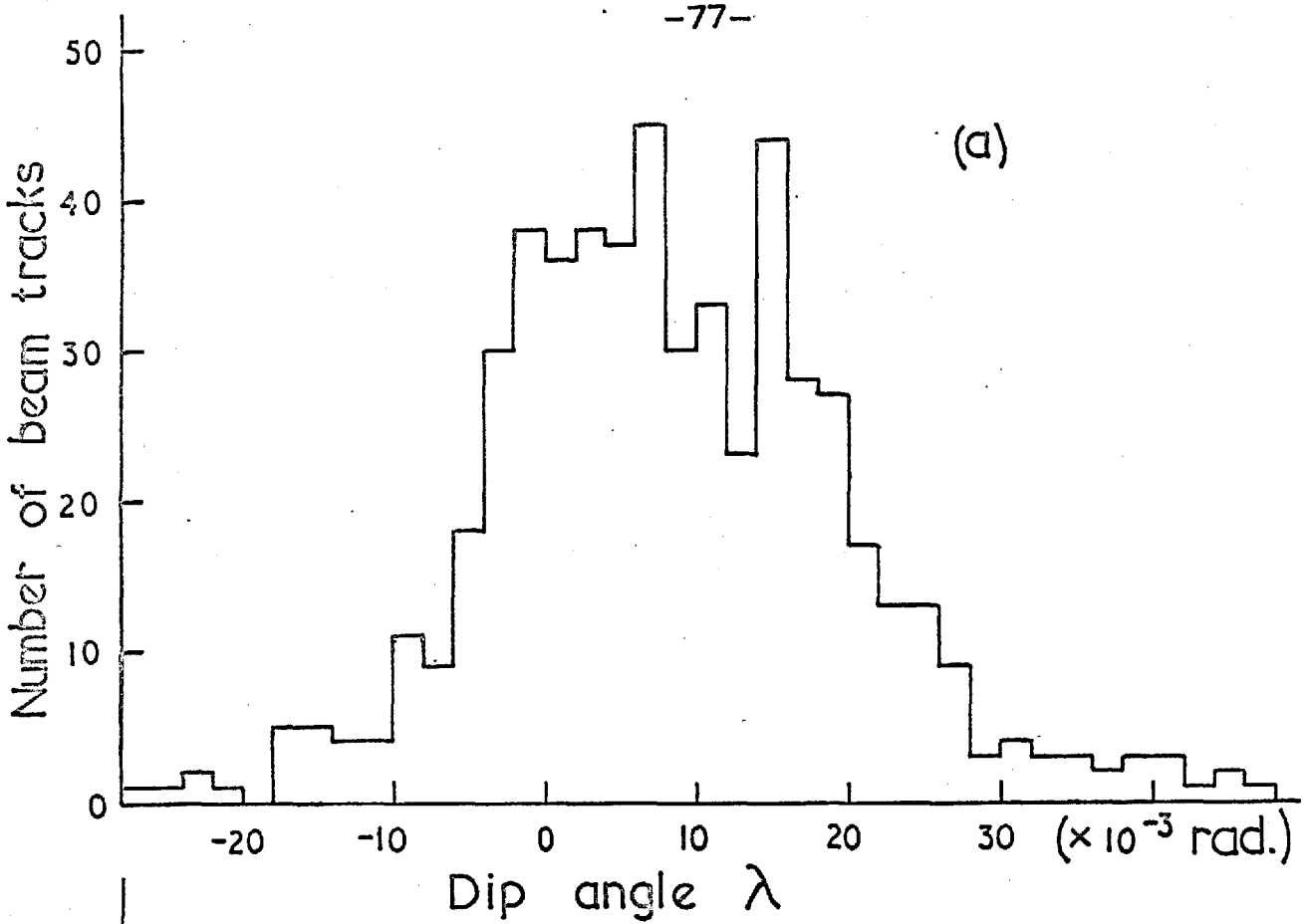
(a)
Number of beam tracks
0
10
20
30
40
50
-20
-10
0
10
20
30
(× 10⁻³ rad.)
Dip angle λ

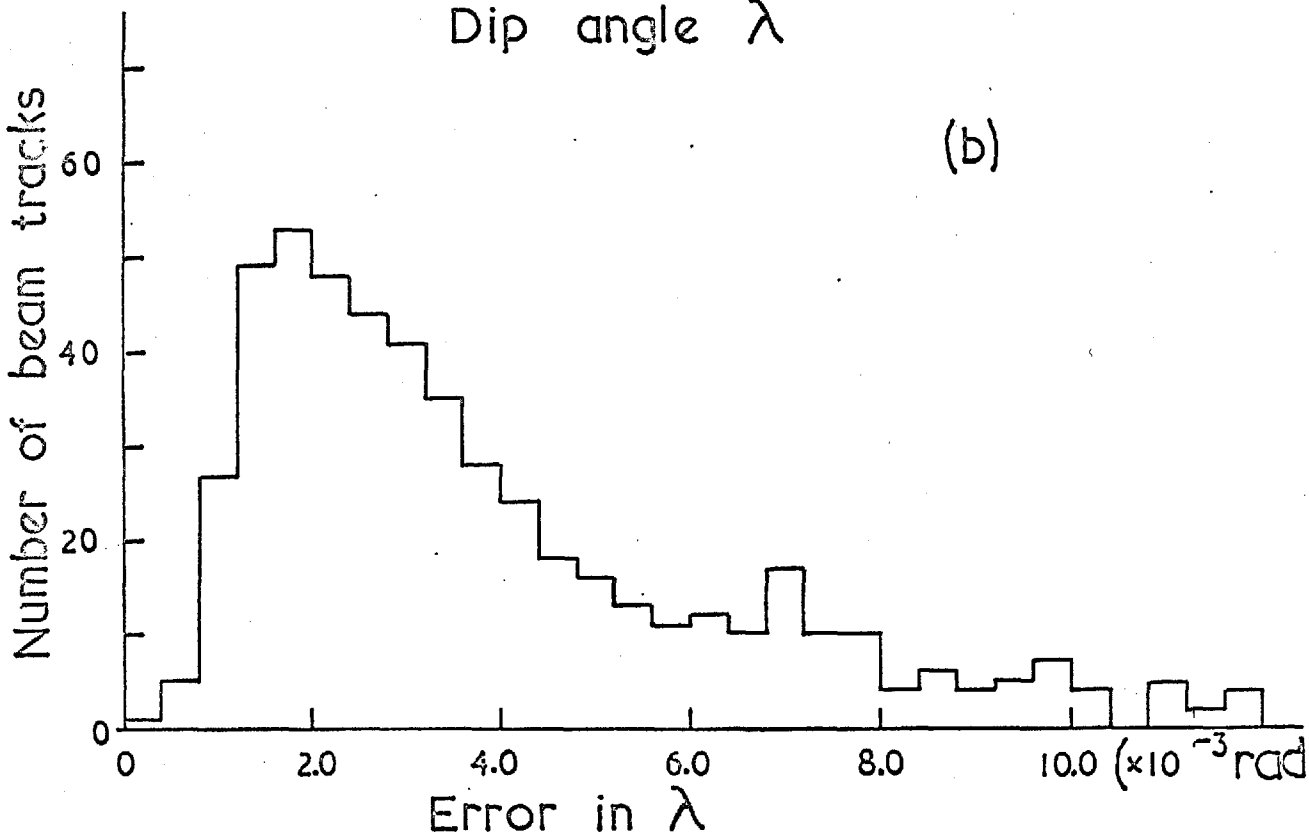
(b)
Number of beam tracks
0
20
40
60
0
2.0
4.0
6.0
8.0
10.0
(×10⁻³ rad.)
Error in λ

Fig.4.3

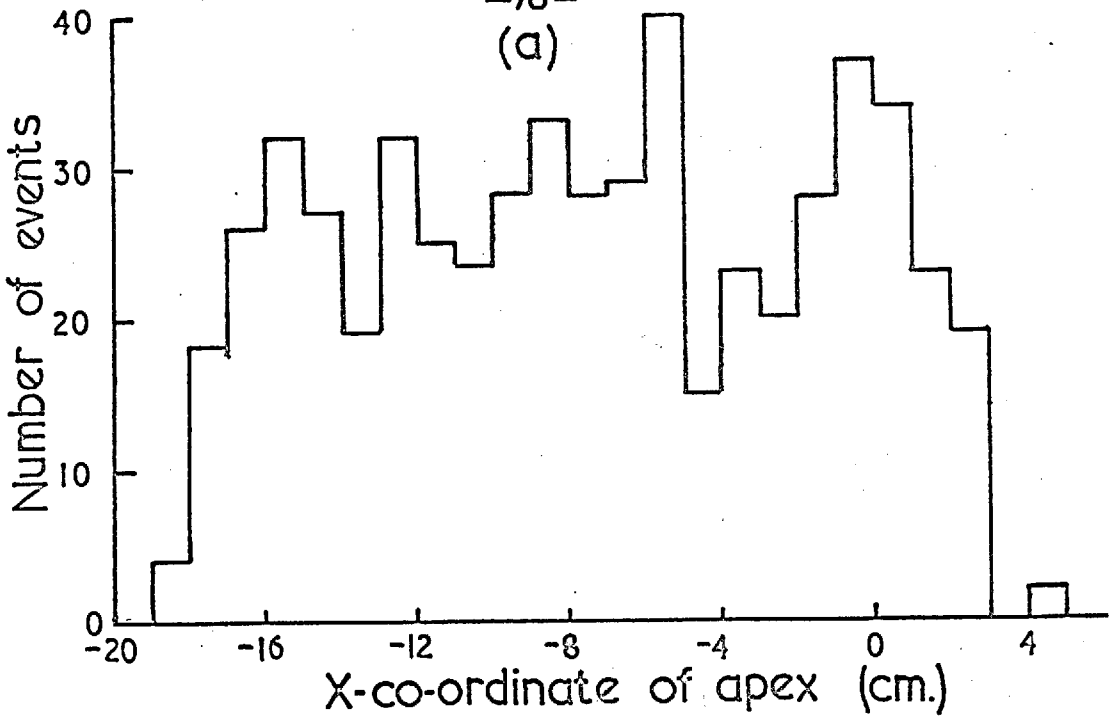
(a)
Number of events
40
30
20
10
0
-20
-16
-12
-8
-4
0
4
X-co-ordinate of apex (cm.)

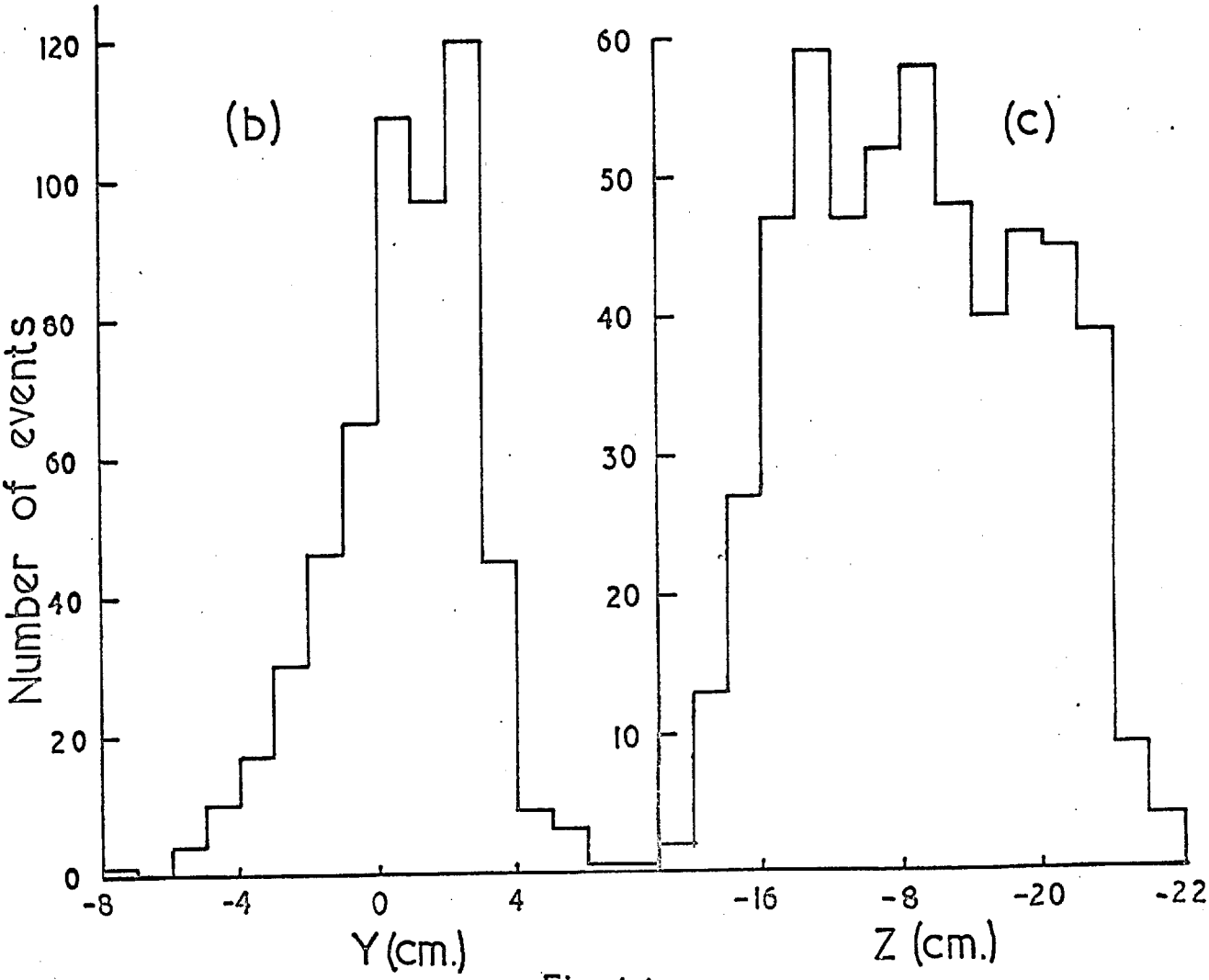
(b)
(c)
Number of events
120
100
80
60
40
20
0
-8
-4
0
4
Y (cm.)
60
50
40
30
20
10
-16
-8
-20
-22
Z (cm.)

Fig. 4.4

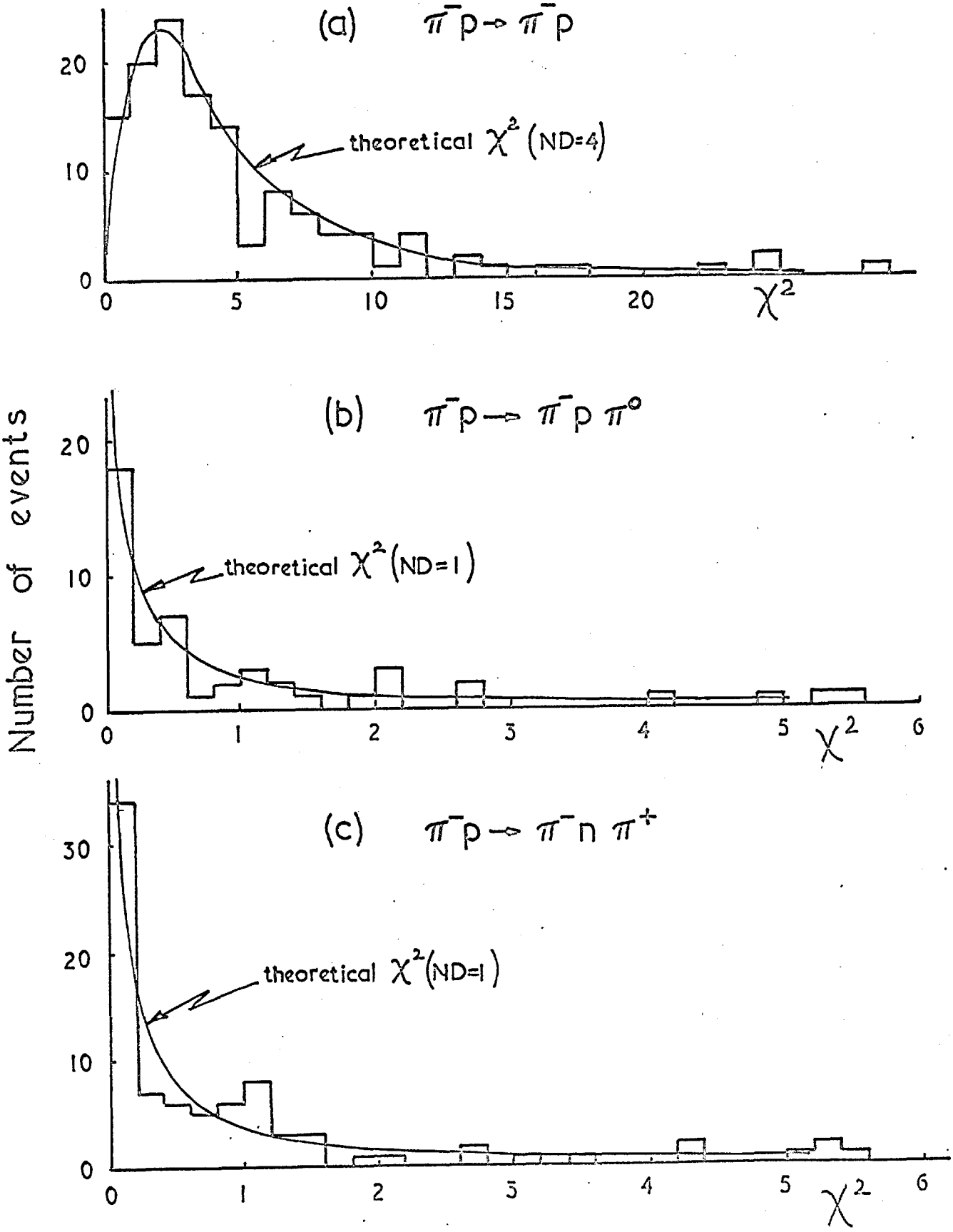
(a) $\pi^- p \to \pi^- p$
theoretical χ^2 (ND=4)
χ^2
(b) $\pi^- p \to \pi^- p \pi^0$
theoretical χ^2 (ND=1)
Number of events
χ^2
(c) $\pi^- p \to \pi^- n \pi^+$
theoretical χ^2 (ND=1)
χ^2

Fig. 4.5

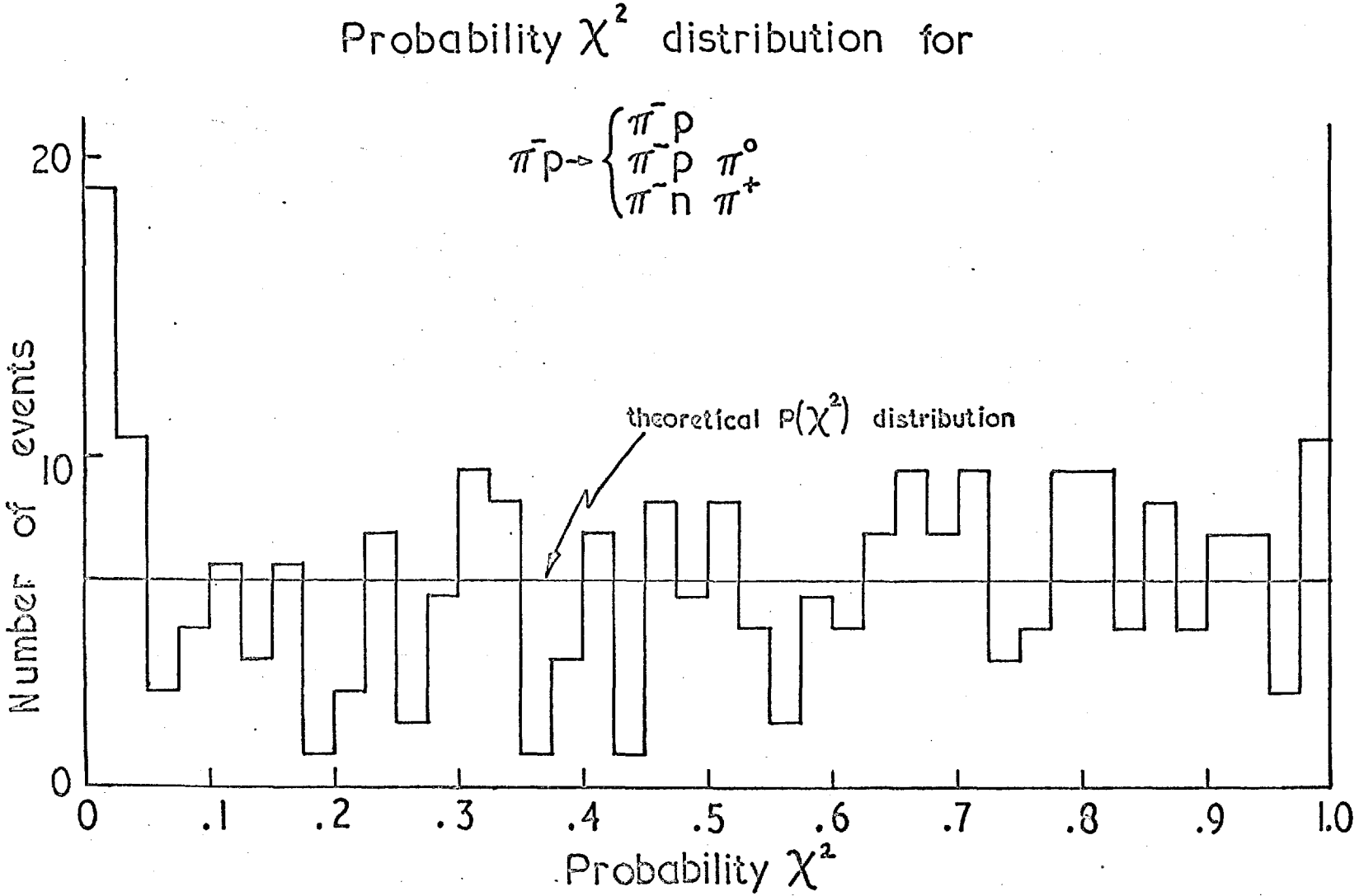
Probability χ^2 distribution for
$\pi^- p \rightarrow \begin{cases} \pi^- p \\ \pi^- p\ \pi^0 \\ \pi^- n\ \pi^+ \end{cases}$
theoretical $P(\chi^2)$ distribution
Number of events
Probability χ^2
0
10
20
0
.1
.2
.3
.4
.5
.6
.7
.8
.9
1.0

Fig. 4.6

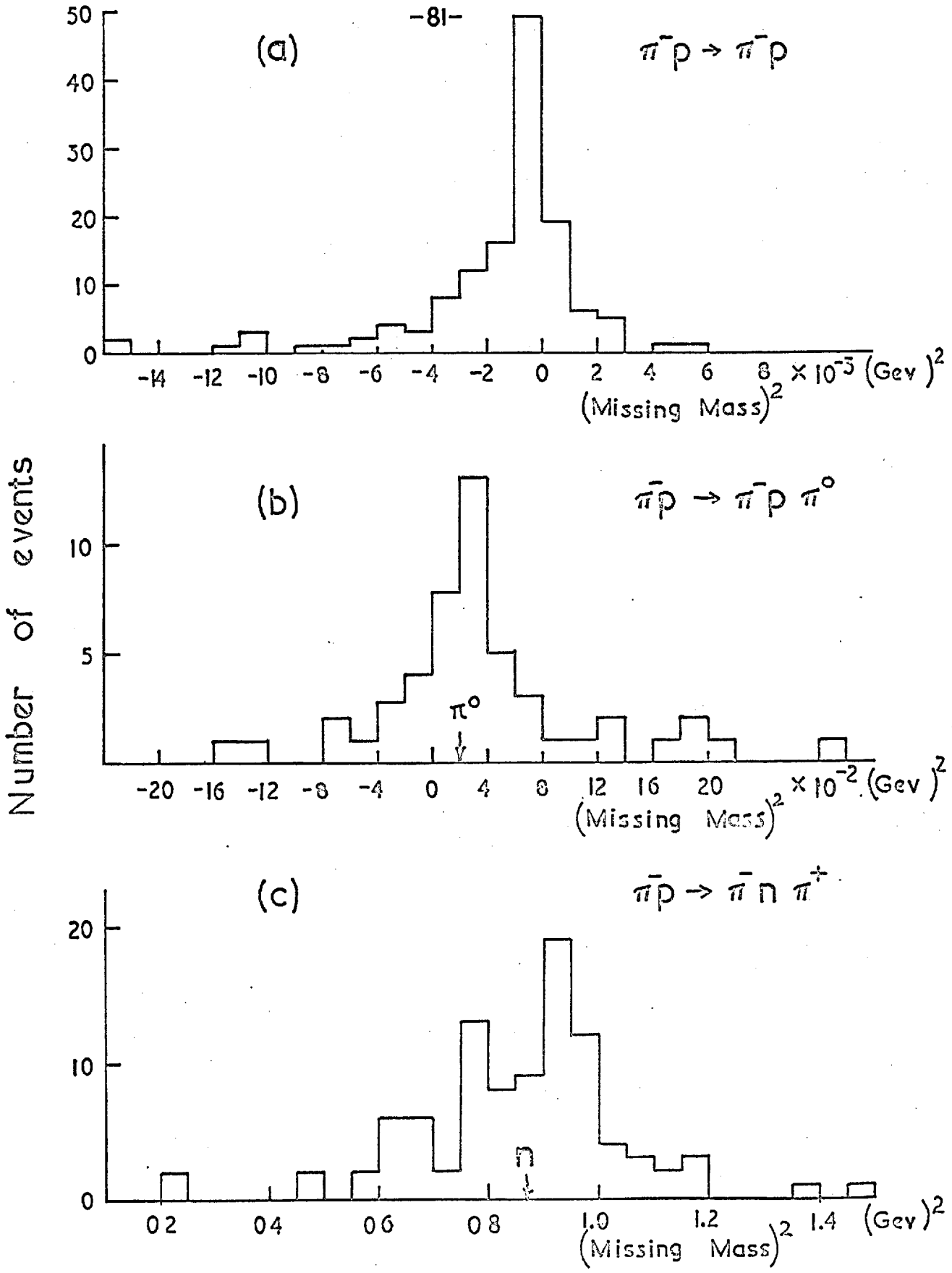
(a)
$\pi^- p \to \pi^- p$
50
40
30
20
10
0
-14 -12 -10 -8 -6 -4 -2 0 2 4 6 8 $\times 10^{-3}$ (Gev)^2
(Missing Mass)^2
Number of events
(b)
$\pi^- p \to \pi^- p\, \pi^0$
10
5
π^0
-20 -16 -12 -8 -4 0 4 8 12 16 20 $\times 10^{-2}$ (Gev)^2
(Missing Mass)^2
(c)
$\pi^- p \to \pi^- n\, \pi^+$
20
10
0
n
0.2 0.4 0.6 0.8 1.0 1.2 1.4 (Gev)^2
(Missing Mass)^2

Fig. 4.7

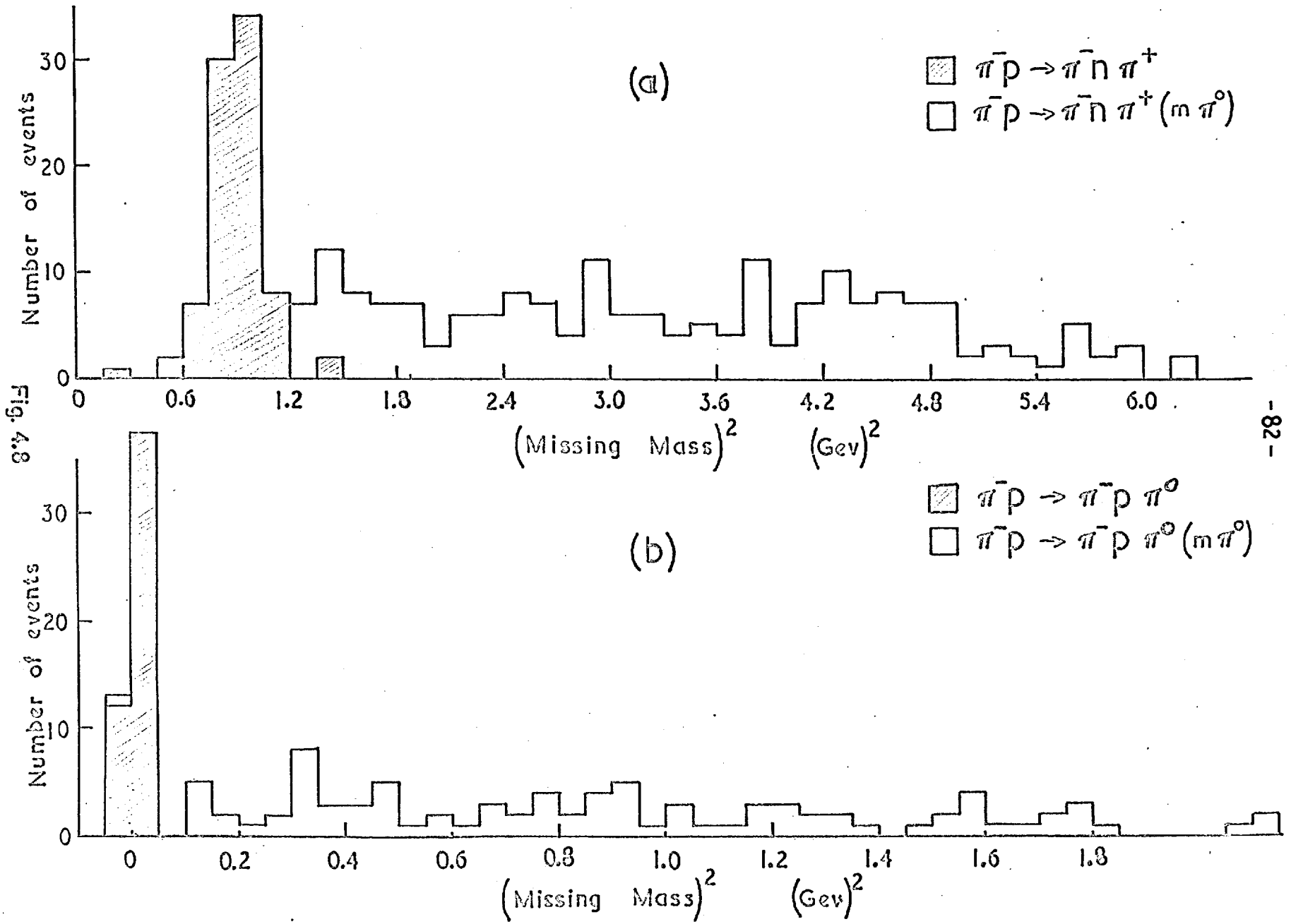
(a)
$\pi^- p \to \pi^- n \pi^+$
$\pi^- p \to \pi^- n \pi^+ (m\pi^0)$
Number of events
0
10
20
30
0
0.6
1.2
1.8
2.4
3.0
3.6
4.2
4.8
5.4
6.0
(Missing Mass)^2 (Gev)^2
(b)
$\pi^- p \to \pi^- p \pi^0$
$\pi^- p \to \pi^- p \pi^0 (m\pi^0)$
Number of events
0
10
20
30
0
0.2
0.4
0.6
0.8
1.0
1.2
1.4
1.6
1.8
(Missing Mass)^2 (Gev)^2

Fig. 4.8

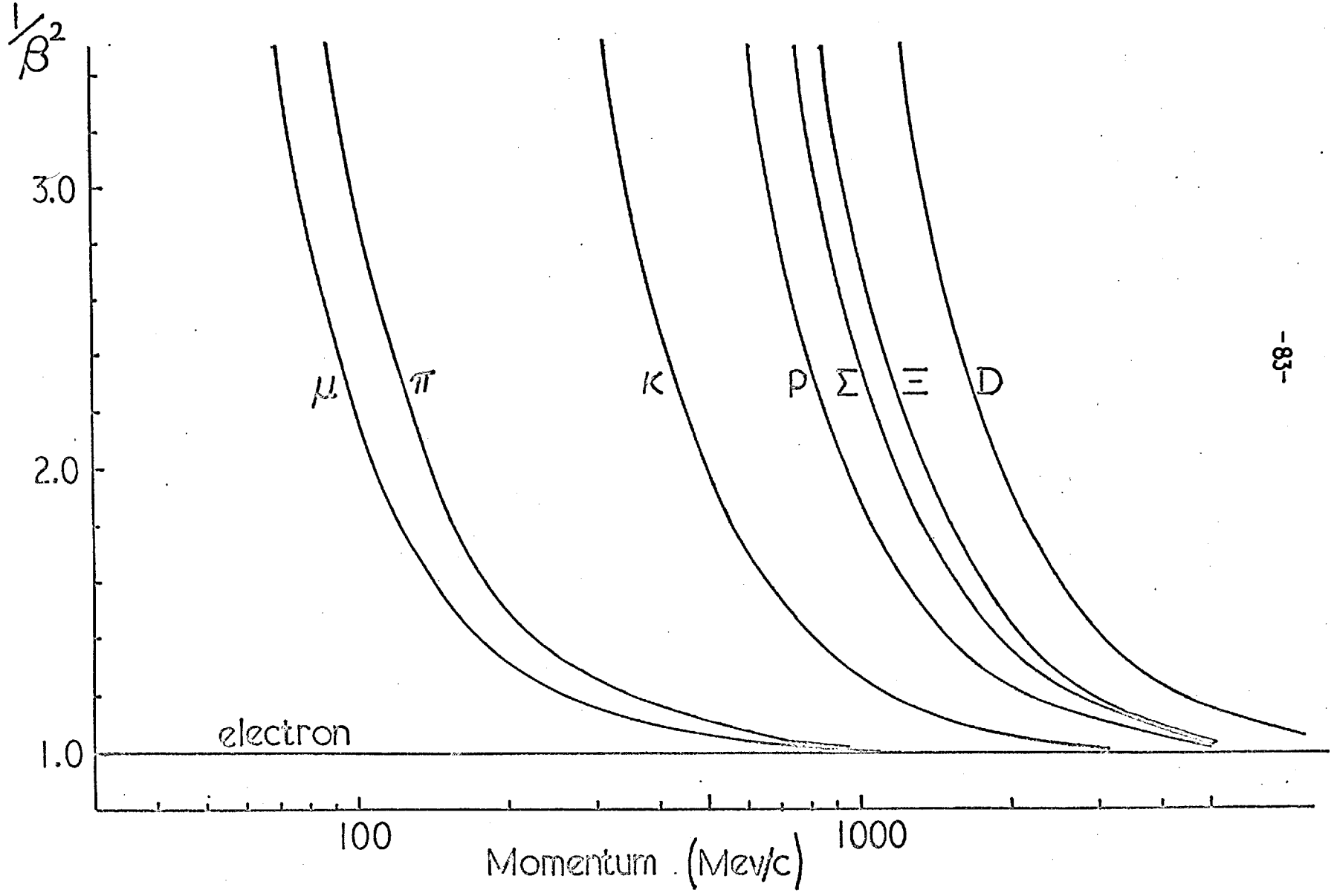

Fig 4.9

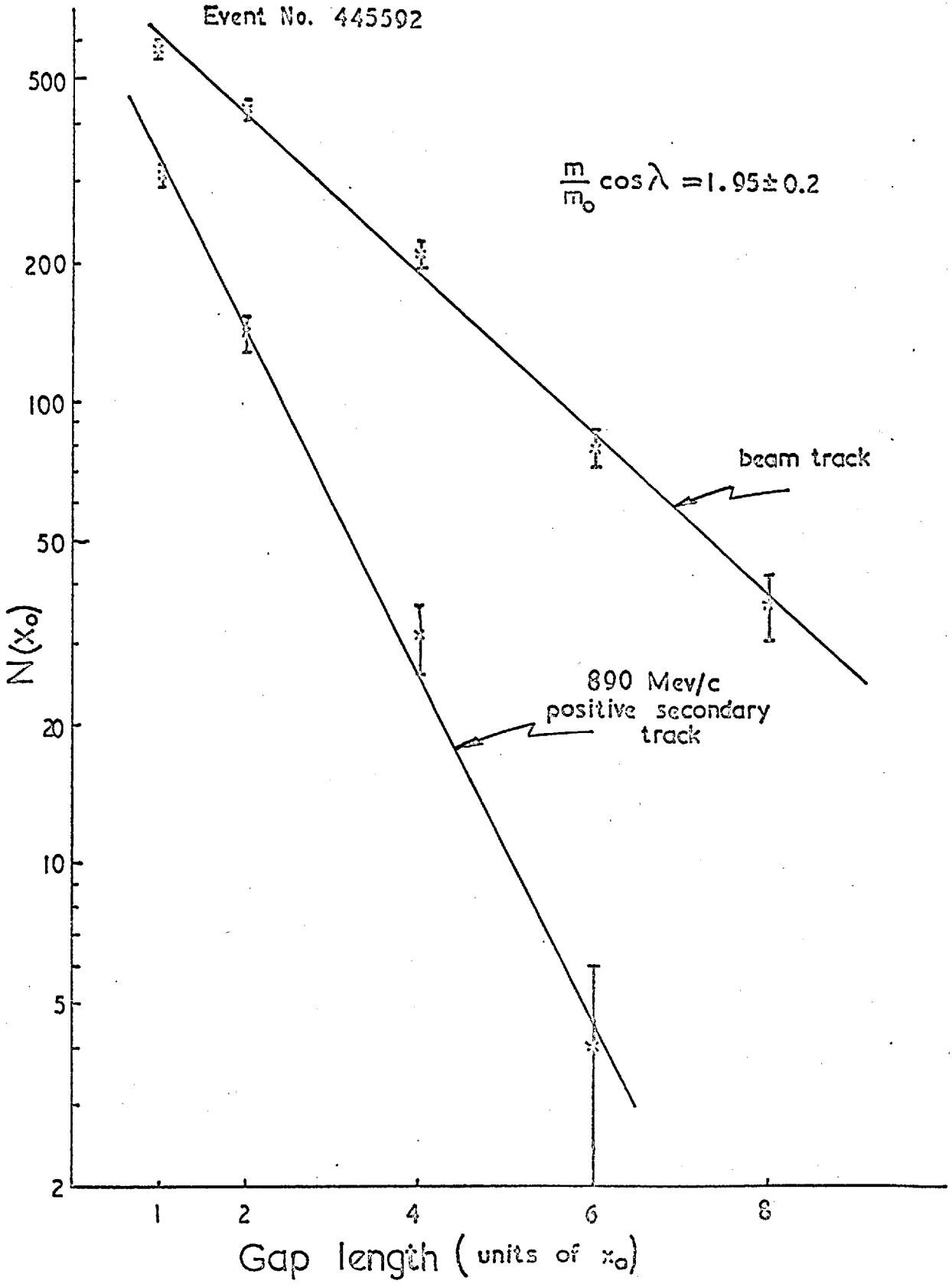
Event No. 445592
$\frac{m}{m_o}\cos\lambda = 1.95 \pm 0.2$
beam track
890 Mev/c
positive secondary
track
N(Xo)
500
200
100
50
20
10
5
2
1
2
4
6
8
Gap length (units of x_o)

Fig. 4.10

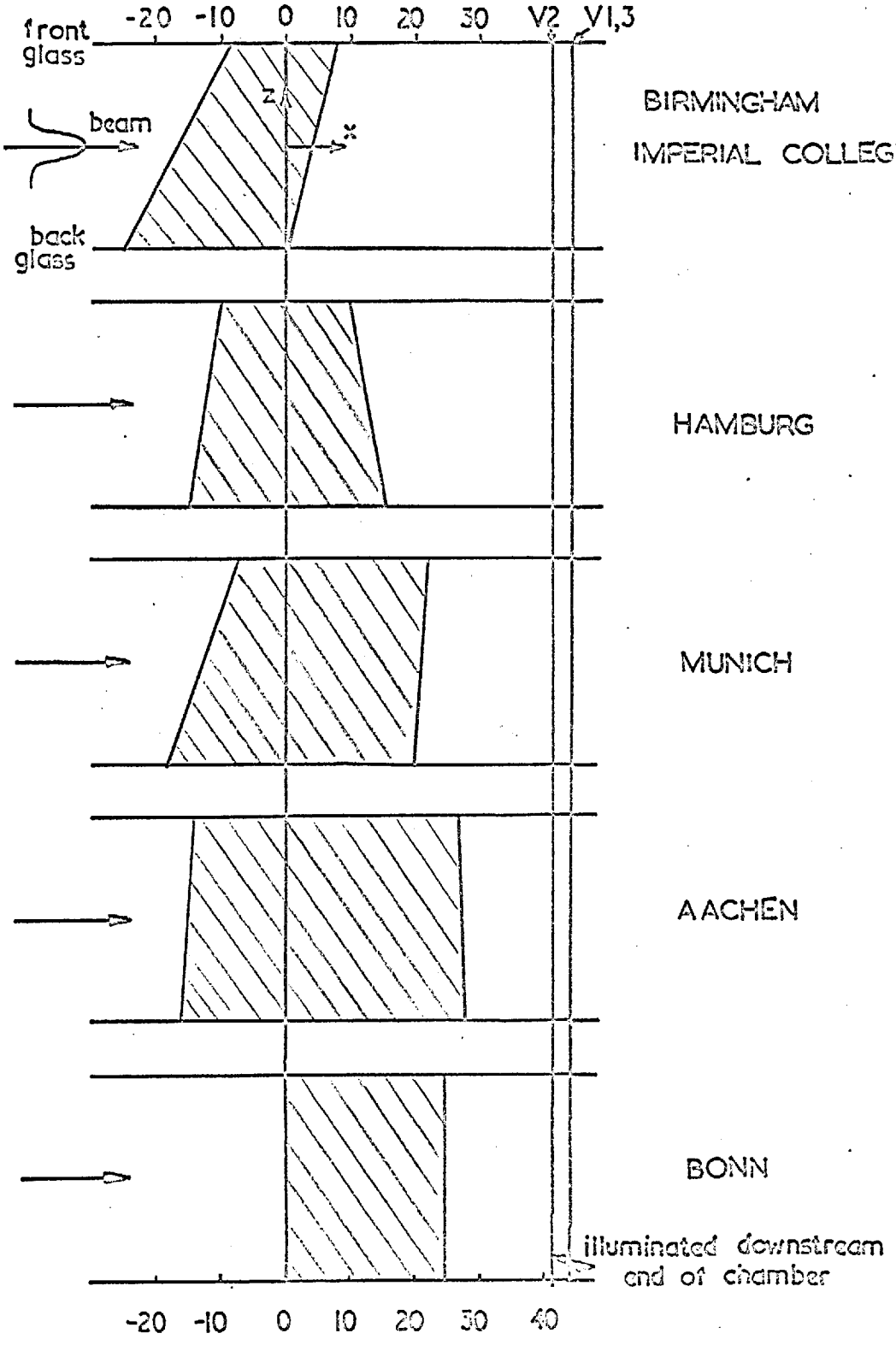

FIDUCIAL REGIONS USED BY EACH GROUP

Fig. 4.11

CHAPTER V

TWO-PRONG INTERACTIONS

5.1 Elastic Scattering

Scanning loss of elastic events occurs in two ways. Firstly, events are missed if the angle between the normal to the scattering plane and the optic axis, ϕ approaches 90°.

$$\phi = \cos^{-1} \frac{(\vec{\pi}_{in} \wedge \vec{\pi}_{out}) \cdot \vec{z}}{|(\vec{\pi}_{in} \wedge \vec{\pi}_{out}) \cdot \vec{z}|} \qquad 5.1$$

The scattering should be isotropic in ϕ, and the anisotropy observed is a measure of the dependence of scanning efficiency on scattering plane orientation. Secondly, when the proton recoil track is short, the event will be overlooked.

To correct for this scanning loss, the distributions of angle ϕ was plotted for various ranges of momentum transfer $-t$, given by

$$t = -2 |p^*|^2 (1 - \cos \vartheta^*) \qquad 5.2$$

where p^* is the centre of mass momentum and ϑ^* is the centre of mass scattering angle of the pion. These plots are shown in Fig. 5.1. For $0.02 \text{ Gev}^2 < -t < 0.04 \text{ Gev}^2$, a correction factor of 1.20 had to be applied, and for $0.04 \text{ Gev}^2 < -t < 0.06 \text{ Gev}^2$ a factor of 1.08, and for $-t > 0.06 \text{ Gev}^2$ the correction was small and not statistically significant. At values of $-t < 0.02 \text{ Gev}^2$, the correction approached 100%, and in this range there

is also the additional loss due to shortness of proton recoil track ($l < 1$cm.); hence these events were not included in the data.

The total elastic cross-section was thus determined by applying the correction, and extrapolating the differential cross-section ($\frac{d\sigma}{dt}$) obtained to $t = 0$ (Fig. 5.2a), and integrating over all values of $-t$. The value thus obtained was (6.62 ± 0.22) mb. Ting et al.,[48] obtained a value of (5.9 ± 0.6) mb. at an incident pion momentum of 4.13 Gev/c. However the value obtained is rather sensitive to the method of extrapolation (see later this section).

At 4 Gev/c, the wavelength of the incident pion in the centre of mass system $\lambda = 0.94 \times 10^{-13}$ cm. , is of the same order as the size of the proton ($\sim 10^{-13}$ cm) as defined by the range of nuclear forces. One therefore can attempt to fit the data with diffraction scattering from an opaque sphere of radius R.

In this approach, one considers a plane wave incident on a spherically symmetric potential, and expresses the scattering amplitude in terms of the usual partial wave expansion [50].

$$f(\theta^*) = \frac{1}{2ik} \sum_{l=0}^{\infty} (2l+1)\,(a_l - 1)\,P_l(\cos\theta^*) \qquad 5.3$$

where $k = |p^*|/\hbar$, a_l is the absorption coefficient for the l^{th} partial wave.

One assumes that the first L (=kR) partial waves are attenuated by the same factor, and all other wave unaffected i.e. $a_l = a$ for all $l \leq L$.

The following results are obtained in the diffraction region:

$$\frac{d\sigma}{d\Omega}(\vartheta^*) = f(\vartheta^*)^2 = (1-a)^2 R^4 k^2 \left| \frac{J_1(kR\sin\vartheta^*)}{kR\sin\vartheta^*} \right|^2 \qquad 5.4$$

$$\sigma(\text{elastic}) = \pi R^2 (1-a)^2 \qquad 5.5$$

$$\sigma(\text{inelastic}) = \pi R^2 (1 - |a|^2) \qquad 5.6$$

$$\sigma_{\text{total}} = \sigma(\text{elastic}) + \sigma(\text{inelastic}) = 2\pi R^2 (1-a) \qquad 5.7$$

In the present data, $\sigma_{\text{total}} = (32.3 \pm 0.7)$ mb., and $\sigma_{\text{elastic}} = (6.62 \pm 0.22)$ mb. This gives a value for the proton radius, R, of $(1.12 \pm 0.04) \times 10^{-13}$ cm, and opacity (1-a) of 0.41 ± 0.02. Fig. 5.2 shows the differential cross-section in the diffraction region as a function of $\cos\vartheta^*$. Curves for the expected angular distribution in the diffraction region are shown for $R = 1.0 \times 10^{-13}$ cm. and $R = 1.1 \times 10^{-13}$ cm. A maximum value of $\cos\vartheta^* = 0.85$ was used for this comparison. Only the most forward points were used because this simple optical model falls below the experimental points at larger angles, making it impossible to get a meaningful fit. Thus a value for R of 1.07 ± 0.03 appears to fit the data well in this region. The values of R are quite similar to those found at other momenta in $\pi^- p$ elastic scattering. Thus at 1.43 Gev/c, $R = 1.08 \times 10^{-13}$ cm. has been reported, [43] and at 5.17 Gev/c, a value $R = 1.04 \times 10^{-13}$ cm [44]. This simple optical model in general only appears to fit the data in the diffraction peak; it also predicts secondary maxima, which are not observed at the right position experimentally, if at

all. A more realistic model e.g. a sphere with a diffuse boundary, would probably better fit the experimental data. A more sophisticated optical model has been recently proposed by Serber,[45] but the statistical accuracy of our data at large angles is poor, and it is only in this region that a significant test of the theory can be made. The forward peak in our data contains 95% of the total elastic cross-section up to $\vartheta^* = 42^\circ$.

A recent attempt at a more basic theory for potential scattering was made by Regge[46] and generalised to various high energy processes by Chew and Frautschi[47]. This "Regge-pole" theory predicts that the elastic diffraction scattering may be expressed in the high energy limit by

$$\frac{d\sigma}{dt} = \left(\frac{d\sigma}{dt}\right)_o F(t) \quad (s/s_o)^{2(\alpha(t)-1)} \qquad 5.8$$

if only the single Pomeranchuk-Regge trajectory is involved. Here s is the square of the total centre of mass energy.

The usual differential cross-section is related to the above expression by

$$\frac{d\sigma}{d\Omega} = - \frac{|P^*|^2}{\pi} \frac{d\sigma}{dt} \qquad 5.9$$

For small t, 5.8 may be approximated by

$$\frac{d\sigma}{dt} = \left(\frac{d\sigma}{dt}\right)_o e^{A(s)t} \qquad 5.10$$

where $A(s)$ can be written in the form $a + b \log_e s$.

Fig. 5.3 shows the differential cross-section $\frac{d\sigma}{dt}$ as a function of -t, where t is in Gev^2. The data are consistent with the exponential distribution above. A least squares fit over the region $0.02\ Gev^2 < -t < 0.4\ Gev^2$ yields a value for $\left(\frac{d\sigma}{dt}\right)_o$ of (52.8 ± 4.0) mb. $(Gev)^{-2}$ and a value for A of $(8.53 \pm 0.49)\ (Gev)^{-2}$ (Fig. 5.2(b)). The probability from a χ^2 test was 10%. At an incident momentum of 4.13 Gev/c, Ting et al[48] obtained a value for A of $(8.0 \pm 0.5)\ (Gev)^{-2}$ in the range $0.07\ Gev^2 < -t < 0.4\ Gev^2$. Our data fitted over the same range of t yields a value of $(7.22 \pm 0.60)(Gev)^{-2}$, consistent with the above value. Our value for A is also consistent with the general compilation of A values given by Brandt et al[49].

When one extends the fit to values of -t up to $0.8\ (Gev)^2$ it is clear that the tail of the diffraction peak rises above a purely exponential behaviour. If one fits to the range $0.02\ Gev^2 < -t < 0.8\ Gev^2$, one obtains a value for A of $6.3 \pm 0.4\ (Gev)^{-2}$, considerably smaller than that obtained in the range $0.02\ Gev^2 < -t < 0.4\ Gev^2$. Thus the linear fit only appears adequate for the latter range of -t.

The data can always be fit much better by adding a quadratic term to the exponential i.e.

$$\frac{d\sigma}{dt} = \left(\frac{d\sigma}{dt}\right)_o e^{A't + B't^2} \qquad 5.11$$

This was done for the range $0.02\ Gev^2 < -t < 0.4\ Gev^2$ and the following values of the constants obtained.

$$\left(\frac{d\sigma}{dt}\right)_o = (68.8 \pm 7.96) \text{ mb. Gev}^{-2}$$

$$A' = (12.9 \pm 1.6) \text{ Gev}^{-2}$$

$$B' = (12.7 \pm 4.3) \text{ Gev}^{-4}$$

with a χ^2 probability of 40%.

For this same interval at 10 Gev/c Brandt et al.[49] obtained $A'=(11.4\pm1.1)$ Gev^{-2} and $B' = 8.9 \pm 2.8 \text{ (Gev)}^{-4}$. Thus two bubble chamber experiments give remarkable agreement between the shape of the diffraction peak over the 4-10 Gev/c range. Perl et al., however, using a spark chamber technique in the 3-5 Gev/c range, found values for $A' = (8.9\pm 1.0) \text{ Gev}^{-2}$ and $B' = 1.2 \pm 1.8 \text{ (Gev)}^{-4}$, in disagreement with our values.

One of the predictions of the Regge theory is that the diffraction peak should shrink i.e. A(s) become large with increasing s. A compilation of existing elastic scattering data by Brandt. et.al., shows that whereas p-p elastic scattering shows a definite shrinkage in going from 3-16 Gev/c the π^- p elastic scattering does not. It thus appears that p-p and π-p diffraction elastic scattering present different behaviours in direct contradiction to the Regge theory based on a single trajectory. It may now be necessary to consider the influence of trajectories other than the Pomeranchuk one, if the Regge approach is to provide a complete understanding of diffraction scattering. However, this lately discredited Regge theory provides at present the only known way of predicting the exponential form

of the differential cross-section over such a large range of t.

In the foward direction ($\vartheta^* = t = o$), one can compare $\left(\frac{d\sigma}{dt}\right)_o$ by extrapolating the differential cross-section with that obtained from the total cross-section using the optical theorem. One can show that, under very general conditions [50] that

$$\sigma_{total} = \frac{4\pi}{k} \text{ Im } \left[f(o)\right] \qquad 5.12$$

where $f(o)$ is the elastic scattering amplitude in the forward direction, and $k = |p^*| / \hbar$. Thus

$$\left(\frac{d\sigma}{d\Omega}\right)_o = |f(o)|^2 = |\text{Re} f(o)|^2 + \frac{k^2}{16\pi^2} \sigma^2_{total} \qquad 5.13$$

It is normally assumed from calculations using forward dispersion relations [51], that Re $f(o)$ is small compared with Im $f(o)$ as a high energy approximation. Most diffraction theories are based on a purely imaginary value of $f(\vartheta)$.

If the linear exponential fit is used for the extrapolation of $\frac{d\sigma}{dt}$ to $-t=o$, one obtains a value

$$\left(\frac{d\sigma}{dt}\right)_o = (52.8 \pm 4.0) \text{ mb/Gev}^2$$

The optical theorem point (O.T.P) shown in Fig. 5.3 is deduced from the total cross-section of (32.3 ± 0.7) mb found in this experiment, giving

$\left|\text{Im } f(o)\right|^2 = (53.4 \pm 2.3)$ mb. /Gev^2, Thus $\left|\frac{\text{Re } f(o)}{\text{Im } f(o)}\right|^2 = -0.01 \pm 0.08$, indicating that the extrapolation intersects the axis just below the optical point. If the total cross-section of (30.5 ± 0.5) mb. found in counter experiments [52] (Fig. 5.4) is used to derive the optical point, one finds $\left|\frac{\text{Re } f(o)}{\text{Im } f(o)}\right|^2 = 0.11 \pm 0.09$.

Before any conclusion can be made for the existence of a Re f(o) at this energy, more statistics must be obtained at small $|t|$ values. It seems that if Re f(o) is to be zero at the momentum of the present experiment, the differential cross-section must flatten out for very small $|t|$. Of course, at very small $|t|$, interference between Coulomb and nuclear scattering will become important.

Several authors have reported the existence of a backwards peak in the large angle differential cross-section.[53] No evidence for such a backwards peak is found in the present data, although statistics are poor for large angle scattering.

5.2. Single Pion Production.

In this section, the general qualitative features of the reactions producing one extra pion will be discussed, namely

$$\pi^- p \longrightarrow \pi^- p \, \pi^o \qquad \text{I}$$

$$\pi^- p \longrightarrow \pi^- n \, \pi^+ \qquad \text{II}$$

More detailed discussion of ρ and f^o production is deferred until

the next Chapter.

5.2.1. Effective Mass Distributions.

Fig. 5.5.(a) shows the effective mass distribution for the $\pi^- \pi^o$ system in reaction I. This system has a resonance at 770 Mev identifiable as the ρ^- meson. The phase space curve shown is normalised to background events only, and it is seen that this is consistent with the mass distribution above 1 Gev.

Fig. 5.5.(b) shows the effective mass distribution for the $\pi^+ \pi^-$ system in reaction II. This distribution includes those ambiguous events which were also kinematically consistent with the reaction $\pi^- p \rightarrow \pi^- p + m\pi^o$. However when these events are separately plotted, the effective mass has the same form. This $\pi^+ \pi^-$ system shows two resonances, the ρ^o at 770 Mev and the f^o at 1260 Mev.

The effective mass distributions for the πN systems are shown in Figs. 5.6. (a) - (d). No convincing evidence for isobar formation is seen, except perhaps in the $M\pi^- n$ combinations. The cross-section for the reaction $\pi^- p \rightarrow \pi^+ + N^*$ is found to be (0.09 ± 0.03) mb. The maxima observed at the higher extremity of the $M_{\pi^- n}$ plot, and at the lower extremity of the $M_{\pi^+ n}$ plot, are kinematic reflections of the asymetric decay of the ρ^o. No such marked effect is seen in the equivalent plots for reaction I, in which the ρ^- is produced.

5.2.2. One Pion Exchange Model.

The single pion production channels are largely dominated by the ρ^o

and f^o resonances, and therefore one expects the reactions to be mainly described by the single pion exchange processes of Fig. 5.7 (a) and (b). In this peripheral model, small momentum transfers result from the emission by the nucleon of a virtual pion which scatters on the incident one.

The distribution of events as a function of four-momentum transfer to the nucleon, $-t$, is shown in Figs. 5.9 (a)-(c). The cases shown are for events of the type

$$\pi^- p \rightarrow p + \rho^- \quad (700 \text{ Mev} < M_{\pi^- \pi^o} < 820 \text{ Mev})$$

$$\pi^- p \rightarrow n + \rho^o \quad (700 \text{ Mev} < M_{\pi^+ \pi^-} < 820 \text{ Mev})$$

$$\pi^- p \rightarrow n + f^o \quad (1160 \text{ Mev} < M_{\pi^+ \pi^-} < 1380 \text{ Mev})$$

Each plot shows a strong accumulation of events for small $|t|$. They are compared with the theoretical distribution given by the Selleri modification of the Chow-Low formula (Chapter II), assuming the dominance of OPE. Thus the dependence of the differential cross-section $\frac{d\sigma}{dt}$ on t can be obtained by integrating equation 2.4 over the range of ω^2 in each case. The formula contains a term dependent on the relative angular momentum of the two pions. It is assumed that in the ρ-peak, the π-π scattering is purely p-wave (l=1) and near the f^o purely d-wave (l=2). The form of the differential cross-section becomes :

$$\frac{d\sigma}{dt} = \frac{t}{(t-\mu)^2} F'(t) \qquad 5.15$$

The characteristic feature of the peripheral interaction arises essentially from the $t/(t-\mu^2)^2$ leading term which gives a peak at $-t=\mu^2$. The function $F'(t)$ produces a small shift of the maximum to a higher $-t$ value. It is seen that the shape of the theoretical curves, which have been normalised to the experimental distributions, agree well with the latter up to $-t = 15\mu^2$. The Selleri formula is only expected to hold in this rang..

If the distribution of momentum transfer to the nucleon is presented in a similar way to that in the case of elastic scattering, an interesting point is revealed. Fig. 5.8 shows that up to a value of $-t$ equal to $30\mu^2(0.6\ \text{Gev}^2)$, the four momentum transfer distribution for the ρ^-, ρ^o and f^o regions may all be fitted by an exponential

$$\frac{d\sigma}{dt} = Ce^{At} \qquad 5.15$$

and with the same A-value as is found from a linear fit to the elastic events in the region $(0.02 < -t < 0.4.\ \text{Gev}^2)$ The lines shown in Fig. 5.8 are drawn with this A-value, $A = (8.53 \pm 0.5)\ \text{Gev}^{-2}$. However, in the region where the Selleri formula is expected to be applicable, the two ways of fitting the data are not really distinguishable.

Another test of the validity of the one pion exchange model (OPE) comes from the production ratio of

$$\frac{\pi^- p \rightarrow n\ \rho^o}{\pi^- p \rightarrow p\ \rho^-}$$

This ratio can be calculated from the products of the Clebsch-Gordon coefficients for the upper and lower vertices of graphs 5.7 (a) and (b). If the ρ meson is produced exclusively by single pion exchange and in a pure T=1 state, it can be shown that this ratio should be two. The experimental result for all values of -t in the ρ region gives a ratio of (1.67 ± 0.42), where the error quoted allows for the uncertainty in subtracting background. This ratio is in agreement with that found in experiments at other incident momenta.

Trieman and Yang[54] proposed a test for the validity of a model with a zero spin exchange particle. Since the pion which propagates between the two vertices of diagrams 5.7 (a) and (b) is spinless, the angular distribution of the two vertices should be uncorrelated. The system is best visualised in the rest frame of the incident particle, the anti-laboratory system. In this frame (Fig. 5.7(c)), the lines of flight of the incident and final nucleons define the plane P_N, while the two final pions define a plane P_π, which intersect along the line of flight of the virtually exchanged pion. The OPE model implies that the angle α_{TY} between the two planes should be uniformly distributed where

$$\cos \alpha_{TY} = \vec{n}_1 . \vec{n}_2$$

$$\vec{n}_1 = \frac{\vec{P}_{in} \wedge \vec{P}_{out}}{|\vec{P}_{in} \wedge \vec{P}_{out}|} \quad , \quad n_2 = \frac{\vec{\pi}^- \wedge \vec{\pi}^o}{|\vec{\pi}^- \wedge \vec{\pi}^o|}$$

p, and π being nucleon and pion momenta. Fig. 5.10 shows the distribution of the angle α_{TY} for all -t values for reactions I and II, and is consistent with isotropy, indicating the dominance of the OPE mechanism in single pion production. The distribution of those events with $-t \leq 15\ \mu^2$ are also shown. The same distribution is obtained, which is to be expected since the reactions are dominated by peripheral i.e. low $|t|$ processes.

5.2.3. Angular and Momentum distributions.

Fig. 5.11 shows the centre of mass momentum distributions for each particle in reactions I and II. These distributions clearly reflect the fact that single pion production is dominated by pion resonance production. The sharp peaking at 1.2 Gev/c in the proton momentum, and at 0.95 Gev/c and 1.2 Gev/c in the neutron momentum indicate the two-body nature of the production processes. The peak in the π^- momentum in reaction II arises from the asymmetric decay of the ρ^o in its own rest system, in which the π^- remembers its initial forward direction before formation of the resonance. This is not so marked in the π^- momentum in reaction I, in which the $\bar{\rho}$ decays symmetrically.

Fig. 5.12 (a) - (f) shows the centre of mass angular distribution for each particle in reaction I and II. The backward peaking of the nucleon distributions and corresponding forward peaking of the π^- distributions arises from the peripheral nature of the interactions. Again, due to the asymmetric decay of the ρ^o in which the π^- goes

forward, we expect the π^+ in reaction II to show a greater tendency to go backward in the overall centre of mass system than in the case for the π^o in reaction I. Comparing Figs. 5.12 (c) and (f), this is seen to be the case.

5.3 Multipion Production.

All distributions discussed in this section have been derived from the measured quantities directly as a fit cannot be carried out for the reactions involving more than one missing neutral particle. The reactions studied were

$$\pi^- p \rightarrow n\,\pi^+\,\pi^- + m\,\pi^o \qquad \text{III}$$

$$\pi^- p \rightarrow p\,\pi^-\,\pi^o + m\,\pi^o \qquad \text{IV}$$

The high cross-section for reaction III (5.57 ± 0.17) mb., may indicate that ω^o production together with a neutron has an appreciable cross-section. The effective mass of the $\pi^- \pi^+$ system is shown in Fig. 5.13 with superimposed normalised phase space curves for the production of $N + 3\pi$, and $N + 4\pi$. Some ρ^o formation appears to be present, as is expected by comparison with the charge symmetric reaction $\pi^- p \rightarrow p\,\pi^+\pi^-\pi^-$ studied in an earlier part of this experiment [55]. The broad peak at 430 Mev is difficult to explain by superposition of phase space curves assuming that $N + 5\pi$ is small. A similar effective mass distribution was obtained by combining $\pi^+ \pi^-$ effective mass combinations from reactions

$$\pi^- p \longrightarrow p \pi^+ \pi^- \pi^-$$

$$\pi^- p \longrightarrow p \pi^+ \pi^- \pi^- \pi^o$$

which showed a significant departure from background at 500 Mev[55], and a small deviation at 400 Mev. These peaks were identified with the resonances at 395 Mev and 520 Mev postulated by Samios et al.[56] However, in the present distribution, the departure from phase space is a very broad peak, and could possibly be explained by the decay products from the ω-meson or by an s-wave interaction near threshold.

Fig. 5.14 shows the effective mass of the $p\pi^-$ system from reaction IV . No significant isobar formation is seen. The missing mass squared distribution for this reaction has also been plotted, and is shown in Fig. 5.15. The narrow peak at $M^2 = 0.31$ Gev^2 presumably arises from neutral η decay, and gives a cross-section for the reaction $\pi^- p \rightarrow p \pi^- \eta$ of (0.11 ± 0.04) mb., if one assumes that 72% of all η-mesons decay neutrally [57]. This cross-section is compatible with that found from the $\pi^+ \pi^- \pi^o$ mass combinationsin the reaction $\bar{\pi}p \rightarrow \pi^- p \pi^+ \pi^- \pi^o$ which gave an upper limit for η production of (0.16 ± 0.07) mb.[55]

The centre of mass momentum distributions for reactions III and IV are shown in Fig. 5.16 and 5.17. No significant departures from background are seen. In general, the momentum distributions are less sensitive to the peripheral model than the centre of mass angular distributions, which are shown in Figs. 5.18 and 5.19. The proton from reaction IV keeps

predominantly its backward direction, and the π^- from each reaction is still peaked forward. The π^+ seems to be emitted isotropically. This peaking of the proton and π^- is not as strong as in the case of reaction I and II, indicating that with increasing multiplicity the peripheral production process is becoming less important. This general feature was also concluded from the study of the charged four prong events.

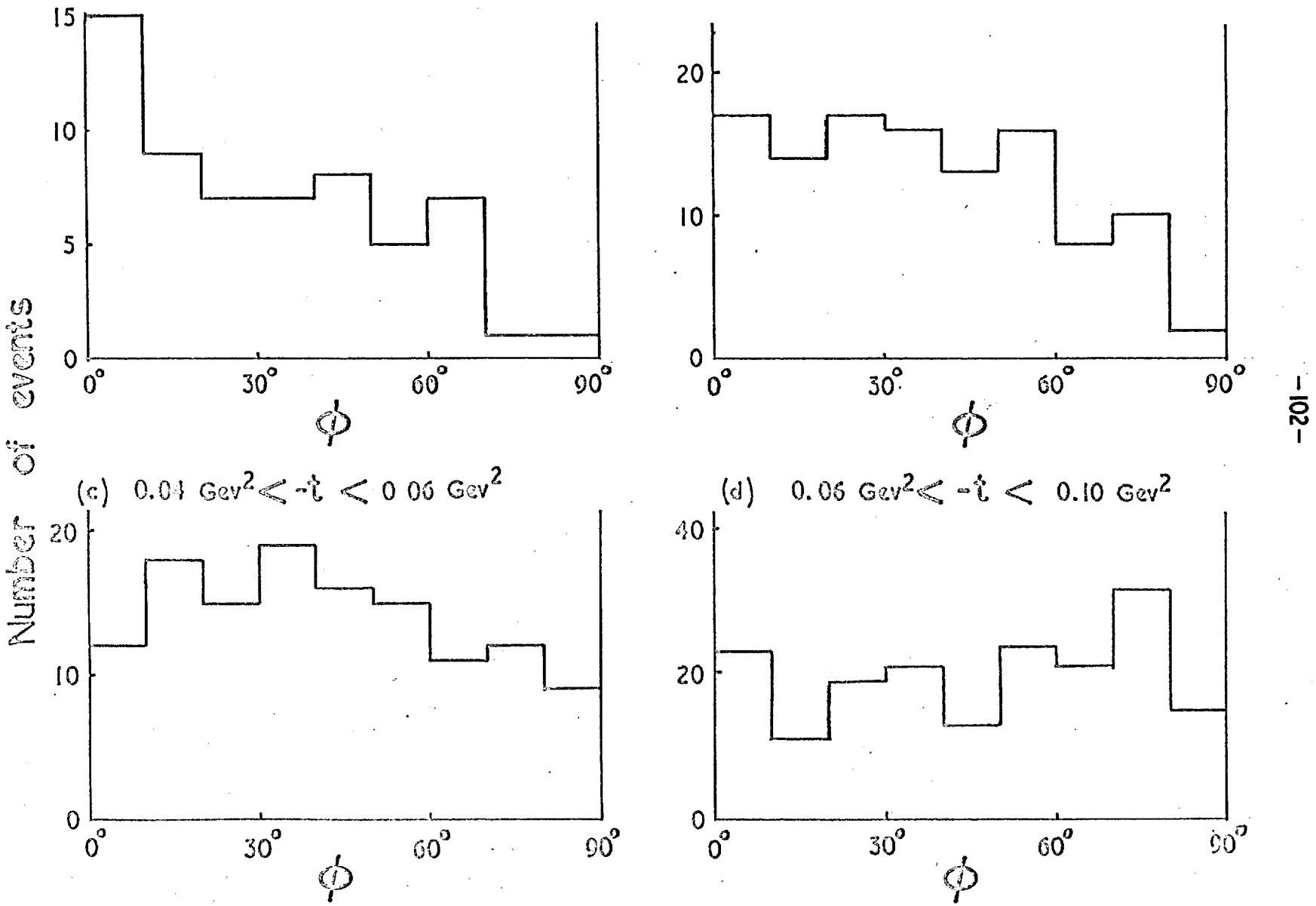

Fig. 5.1

ELASTIC EVENTS AZIMUTHAL LOSS

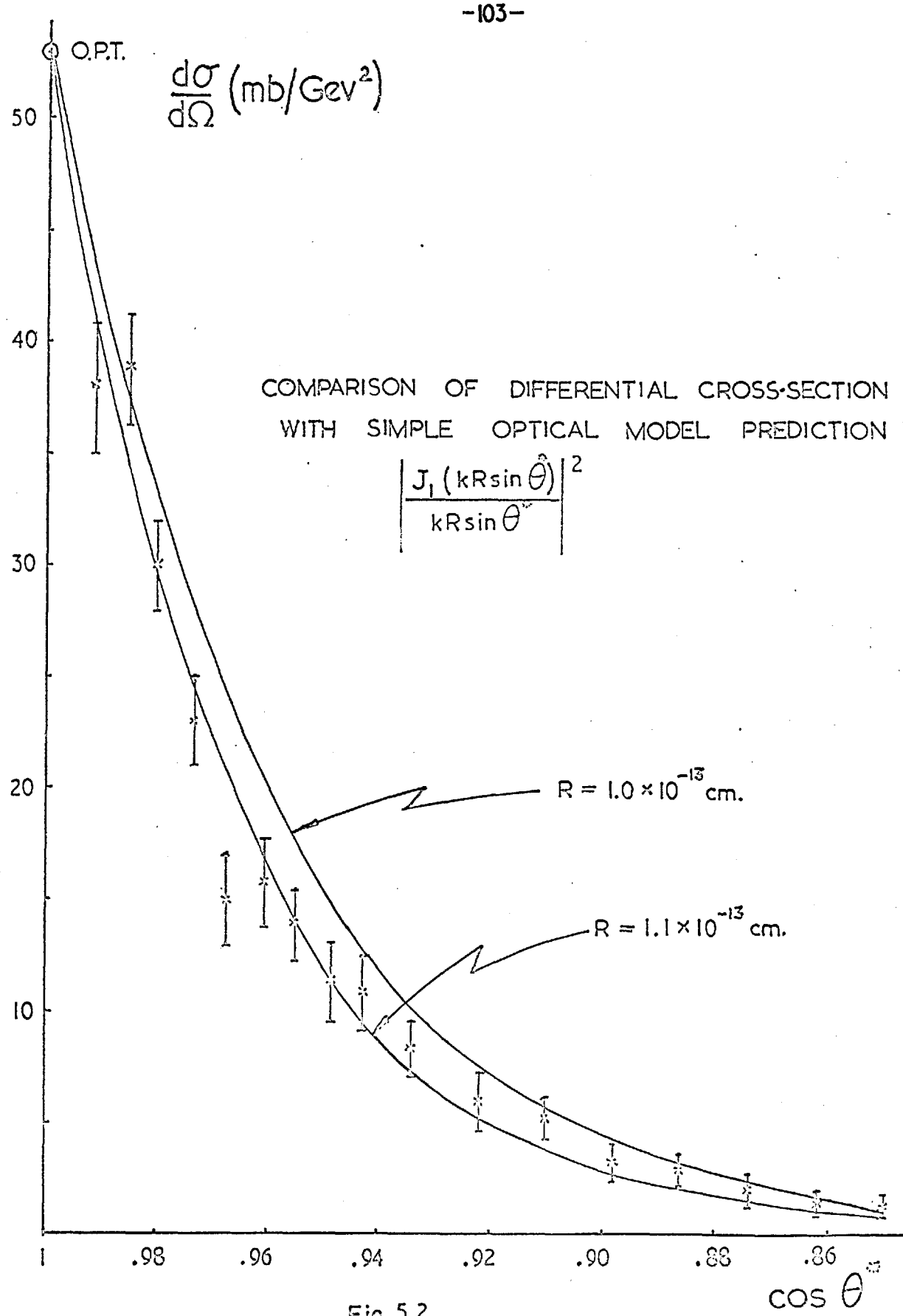
O.P.T.
$\frac{d\sigma}{d\Omega}$ (mb/Gev^2)
50
40
30
20
10
COMPARISON OF DIFFERENTIAL CROSS-SECTION
WITH SIMPLE OPTICAL MODEL PREDICTION
$\left|\frac{J_1(kR\sin\theta)}{kR\sin\theta}\right|^2$
R = 1.0 × 10^{-13} cm.
R = 1.1 × 10^{-13} cm.
1
.98
.96
.94
.92
.90
.88
.86
cos θ

Fig. 5.2

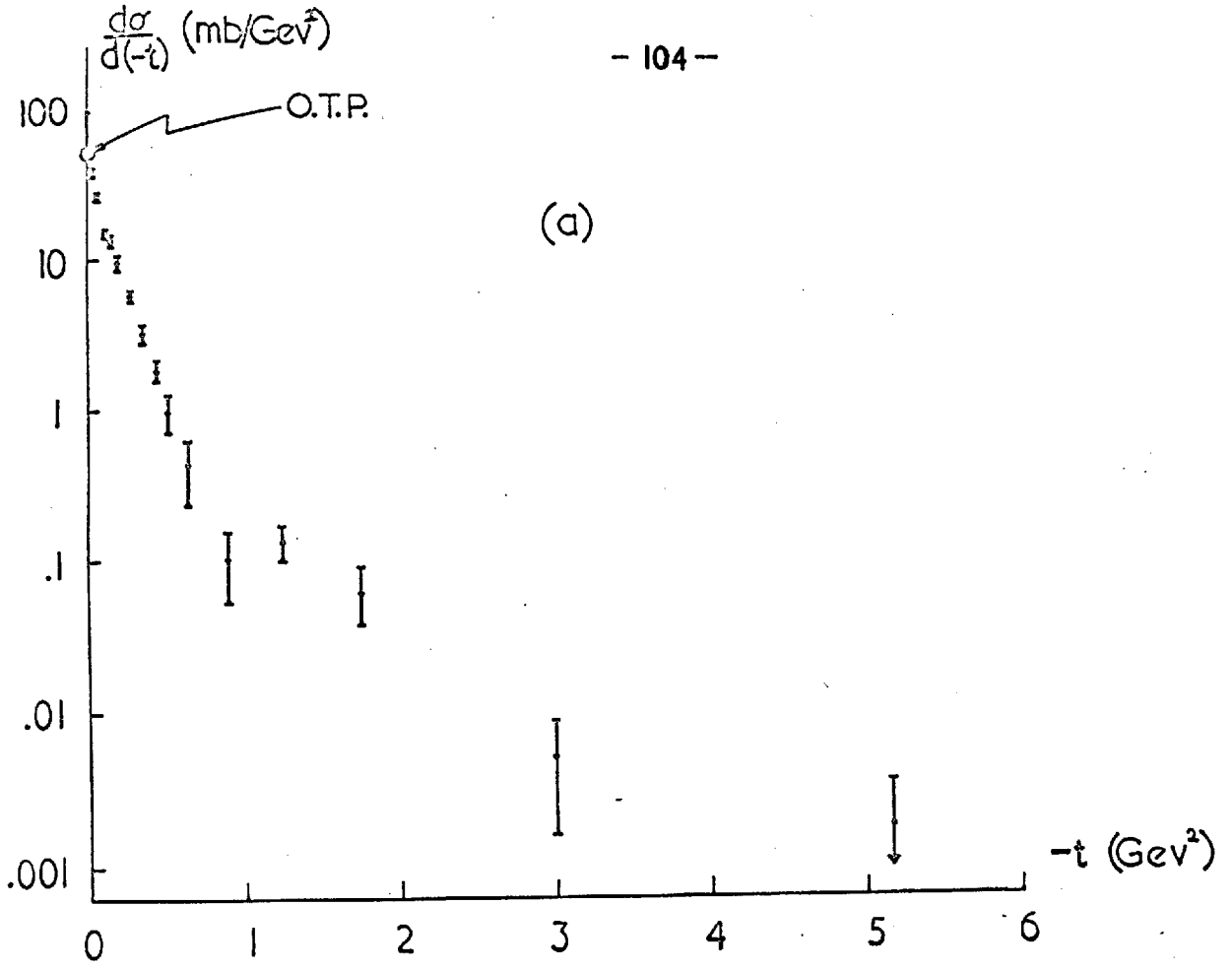
dσ/d(-t) (mb/Gev²)
O.T.P.
(a)
100
10
1
.1
.01
.001
0
1
2
3
4
5
6
-t (Gev²)

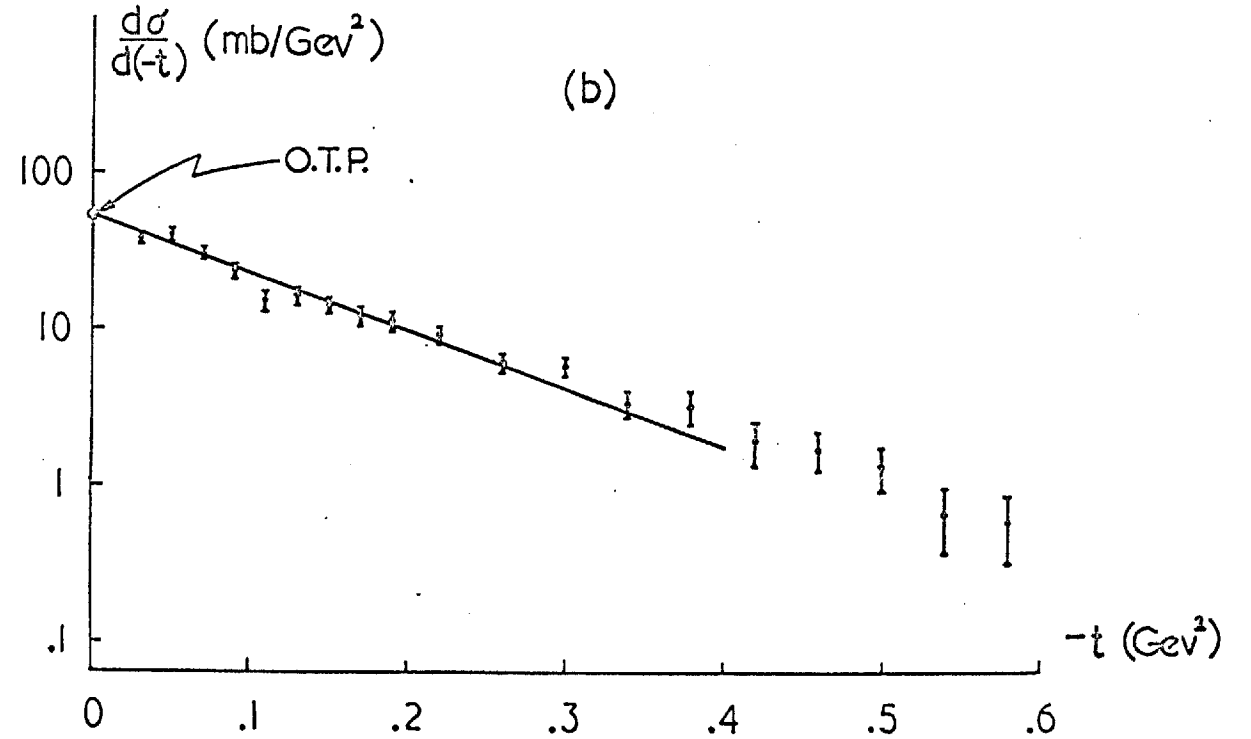
dσ/d(-t) (mb/Gev²)
(b)
O.T.P.
100
10
1
.1
0
.1
.2
.3
.4
.5
.6
-t (Gev²)

Fig. 5.3

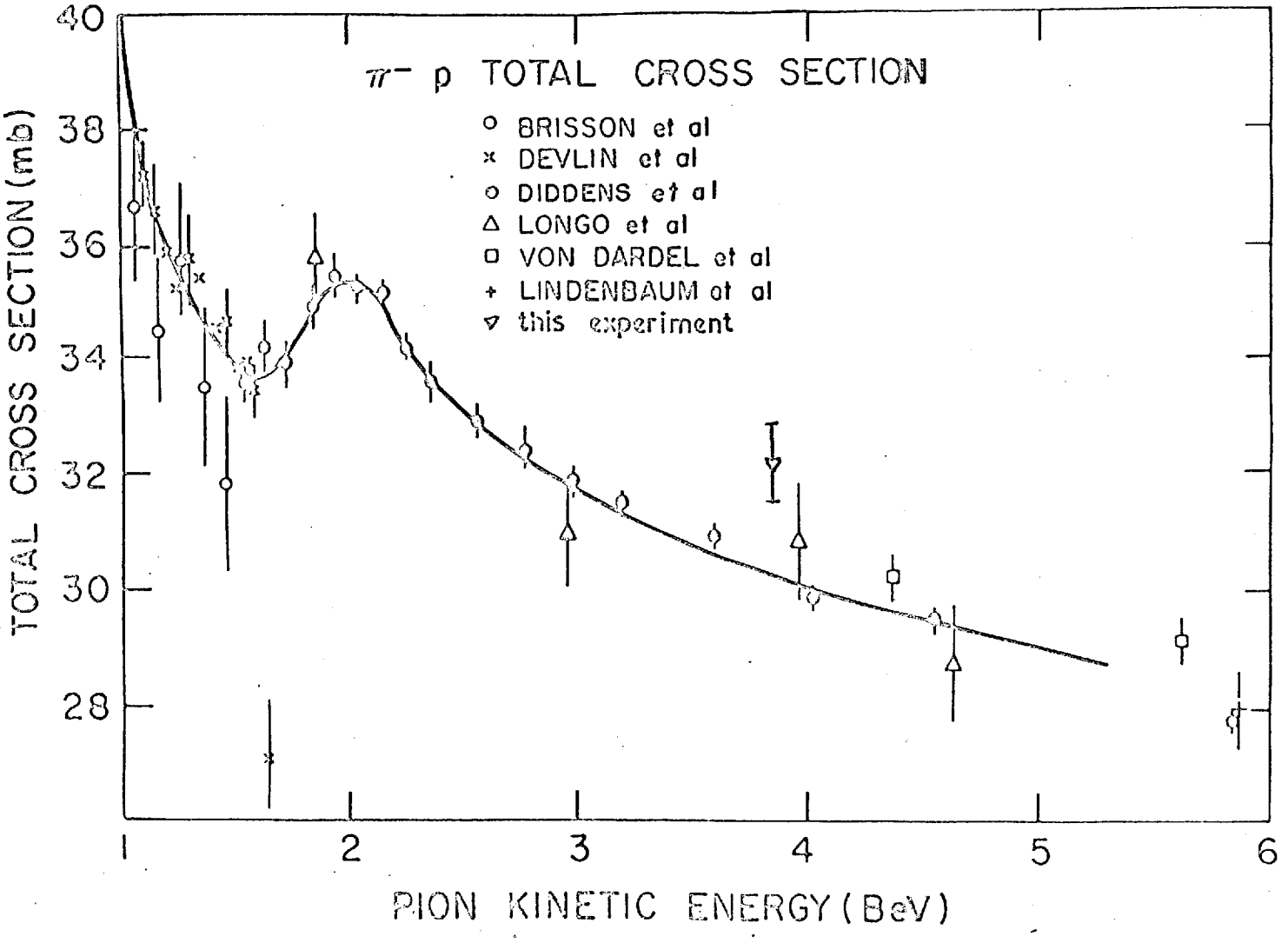
π^- p TOTAL CROSS SECTION
BRISSON et al
DEVLIN et al
DIDDENS et al
LONGO et al
VON DARDEL et al
LINDENBAUM et al
this experiment
TOTAL CROSS SECTION (mb)
40
38
36
34
32
30
28
1
2
3
4
5
6
PION KINETIC ENERGY (BeV)

Fig. 5.4

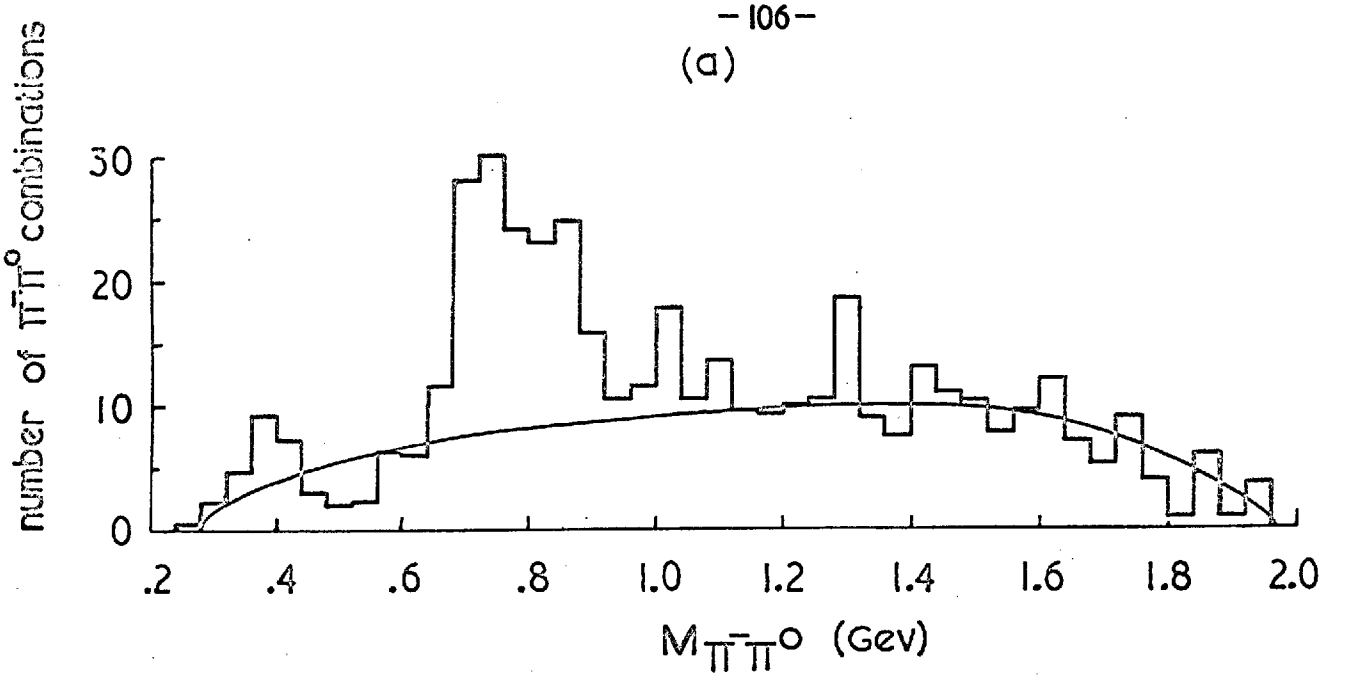
(a)
number of $\pi^-\pi^0$ combinations
30
20
10
0
.2
.4
.6
.8
1.0
1.2
1.4
1.6
1.8
2.0
$M_{\pi^-\pi^0}$ (Gev)

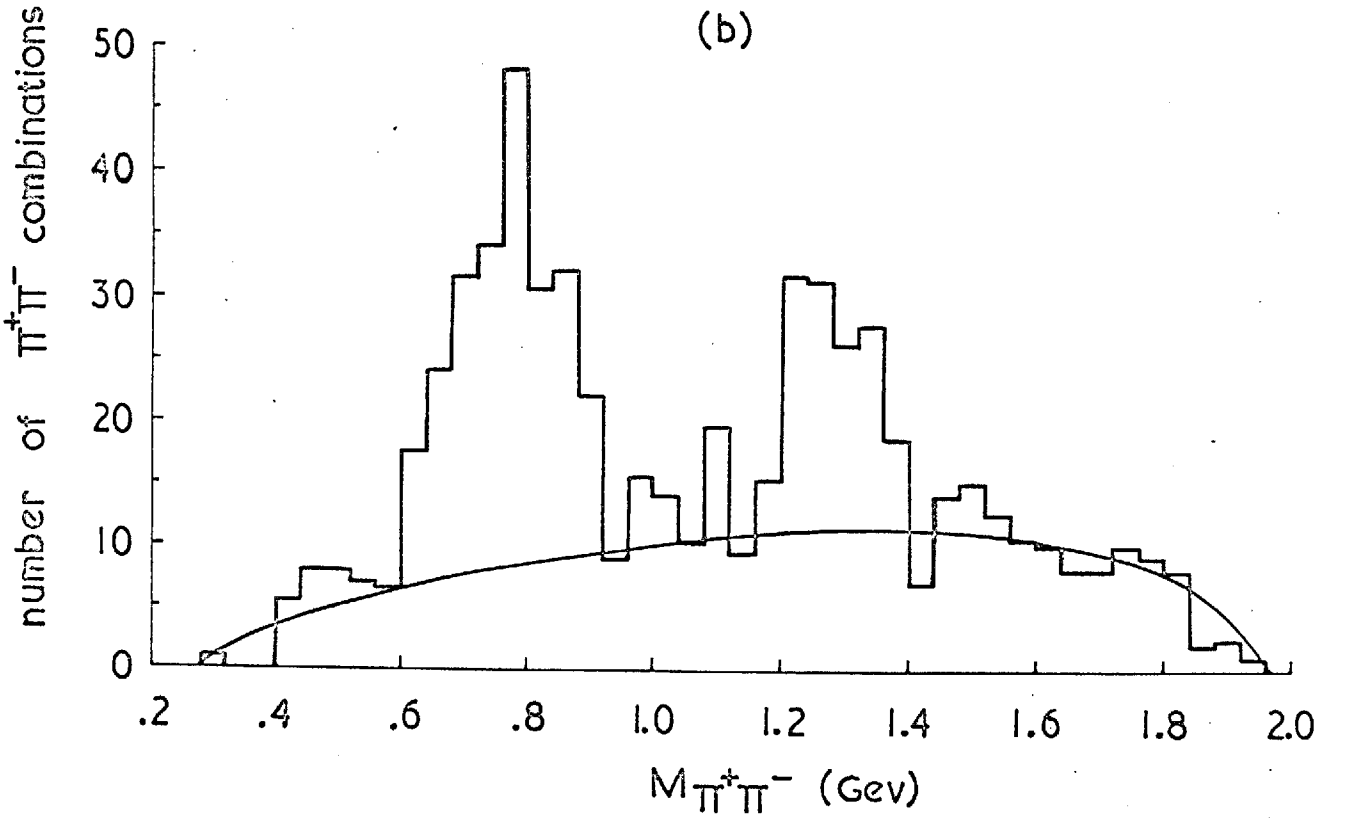
(b)
number of $\pi^+\pi^-$ combinations
50
40
30
20
10
0
.2
.4
.6
.8
1.0
1.2
1.4
1.6
1.8
2.0
$M_{\pi^+\pi^-}$ (Gev)

Fig. 5.5

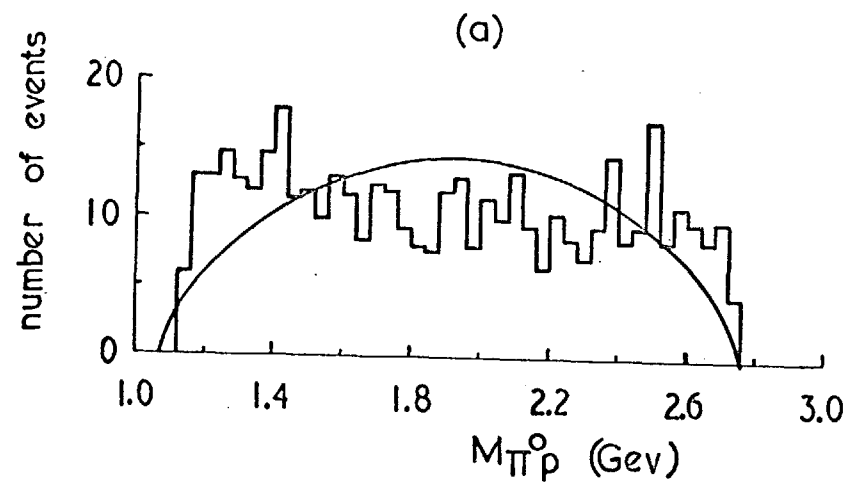
(a)
number of events
20
10
0
1.0
1.4
1.8
2.2
2.6
3.0
$M_{\pi^0 p}$ (Gev)

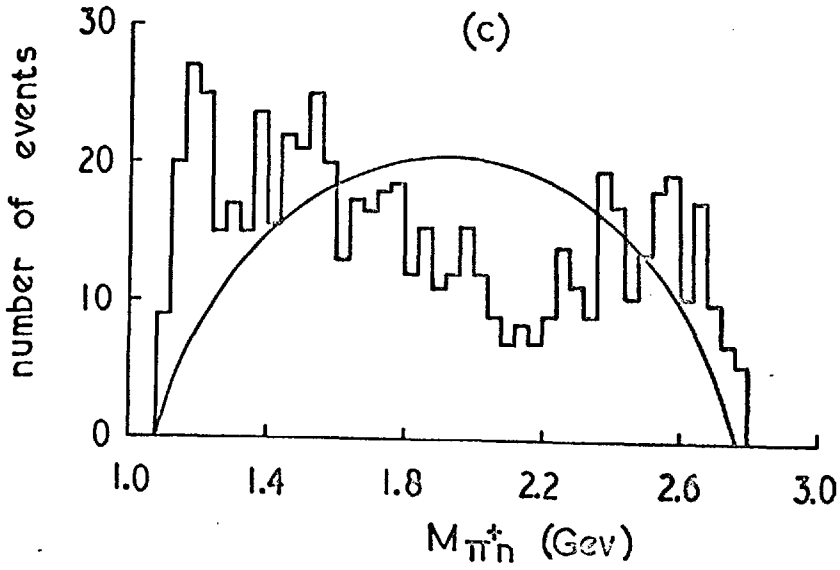
(c)
number of events
30
20
10
0
1.0
1.4
1.8
2.2
2.6
3.0
$M_{\pi^+ n}$ (Gev)

Fig. 5.6

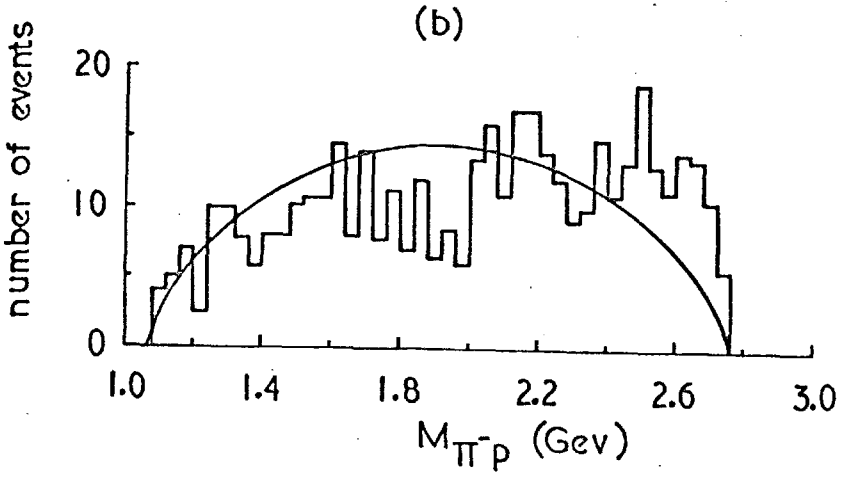
(b)
number of events
20
10
0
1.0
1.4
1.8
2.2
2.6
3.0
$M_{\pi^- p}$ (Gev)

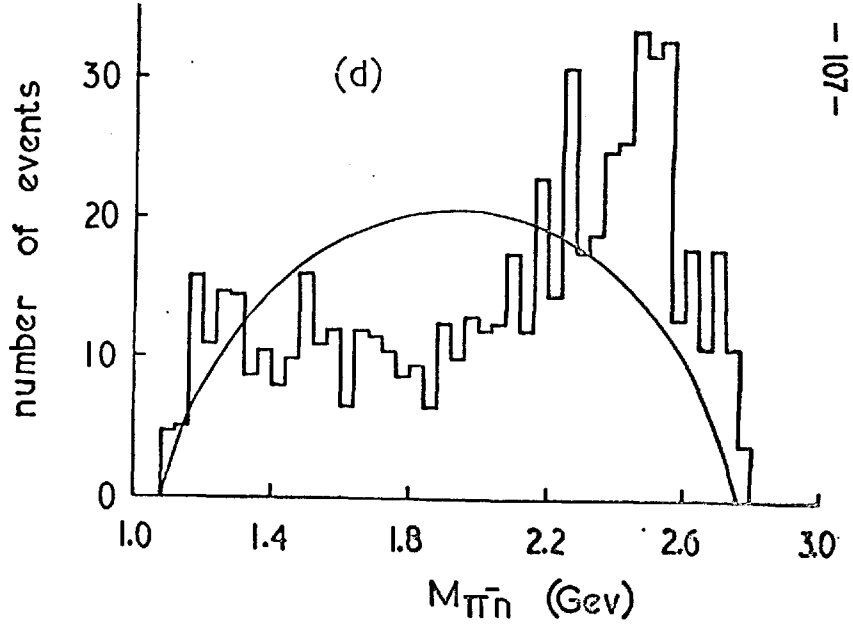
(d)
number of events
30
20
10
0
1.0
1.4
1.8
2.2
2.6
3.0
$M_{\pi^- n}$ (Gev)

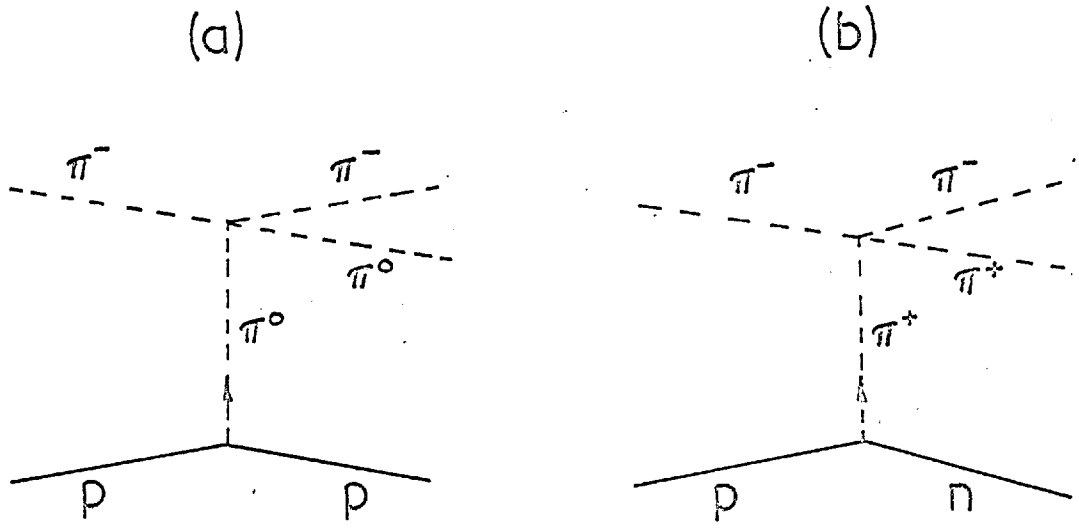

SINGLE PION EXCHANGE DIAGRAMS

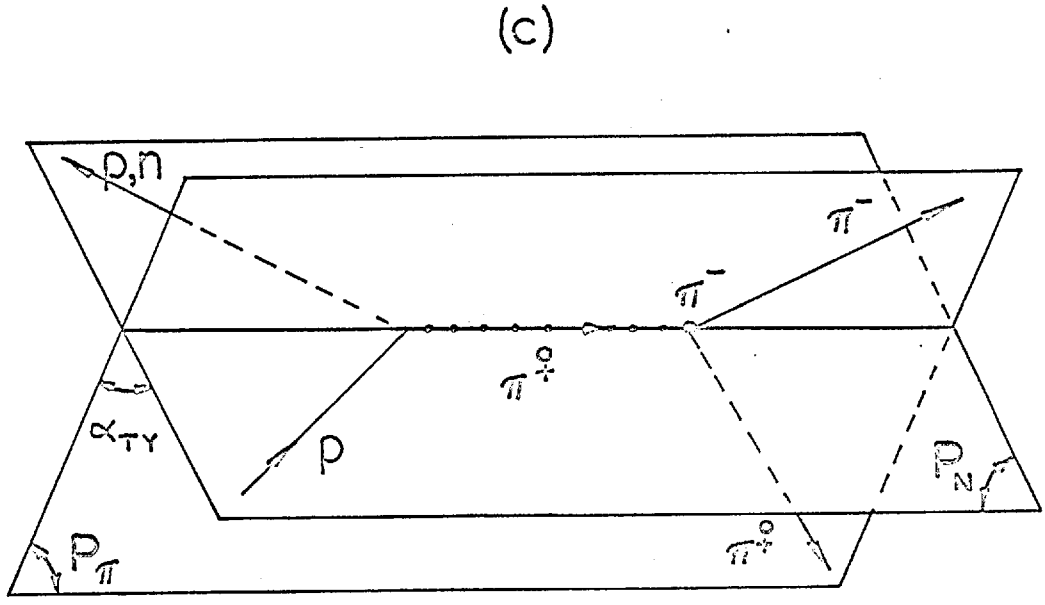

TREIMAN YANG TEST

Fig. .7

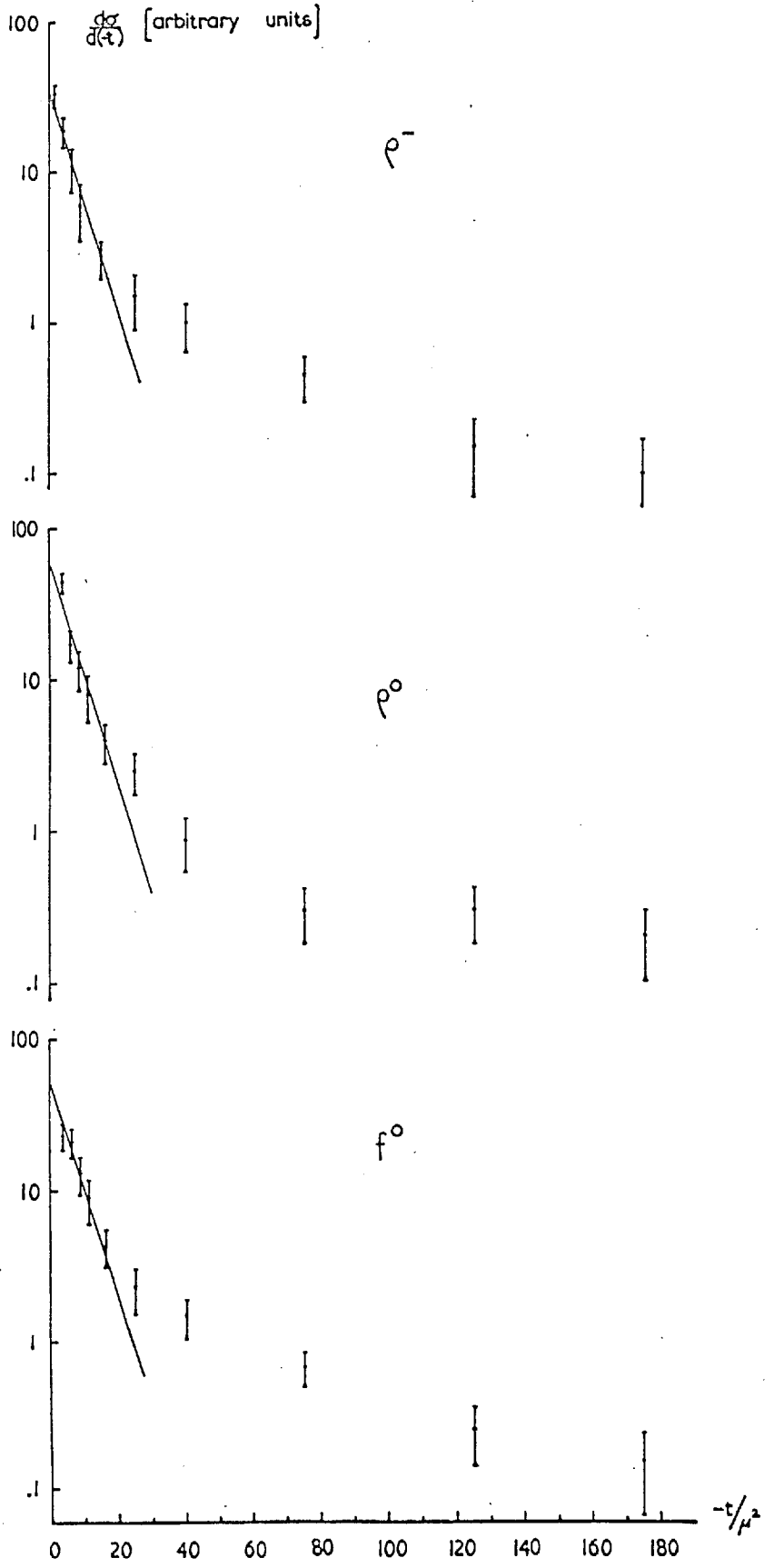
$\frac{d\sigma}{d(-t)}$ [arbitrary units]
100
10
1
.1
ρ^-
ρ^0
f^0
0
20
40
60
80
100
120
140
160
180
$-t/\mu^2$

Fig. 5.8

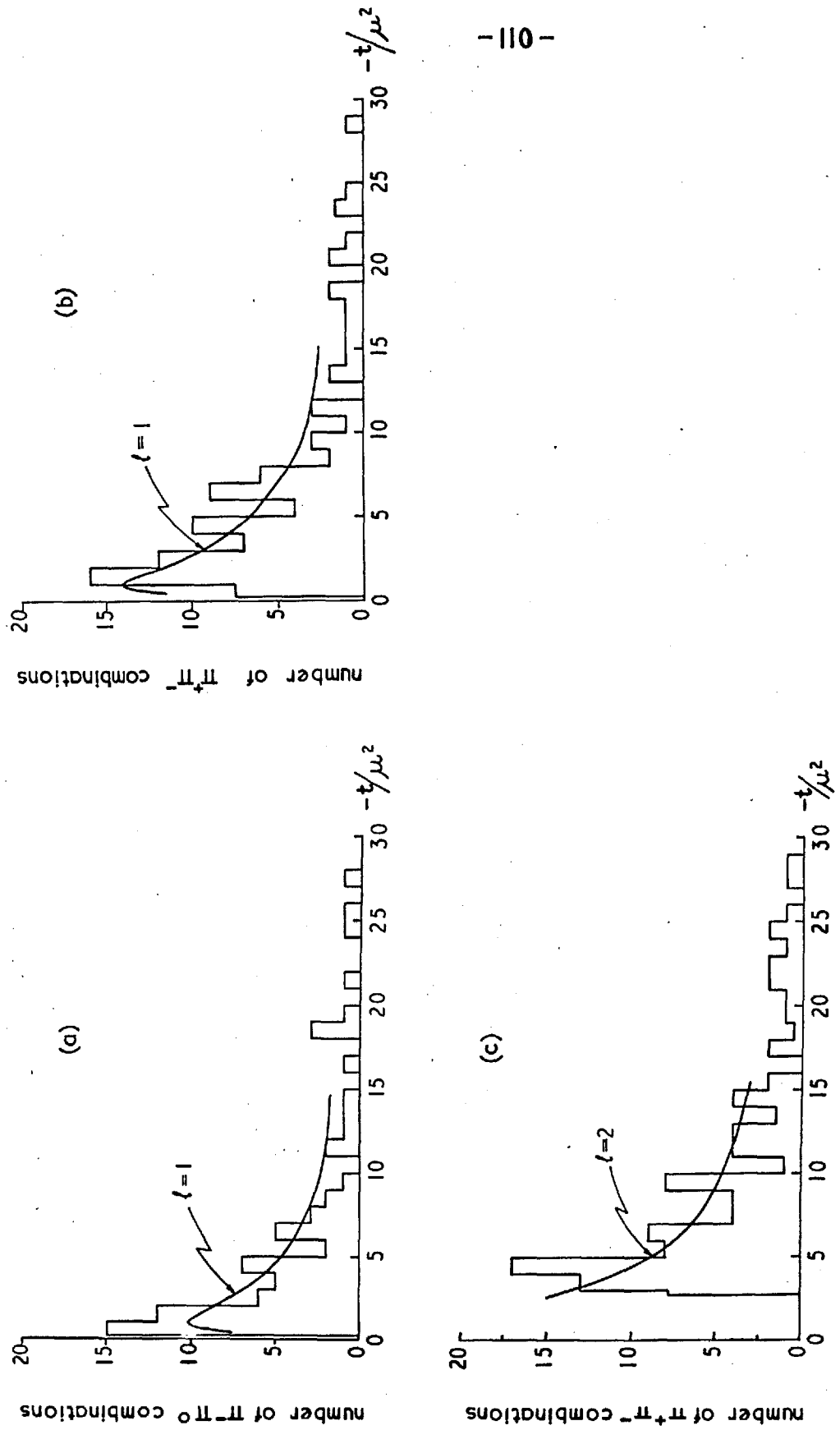
(a)
(b)
(c)
$\ell = 1$
$\ell = 1$
$\ell = 2$
number of $\pi^-\pi^0$ combinations
number of $\pi^+\pi^-$ combinations
number of $\pi^+\pi^-$ combinations
$-t/\mu^2$
0
5
10
15
20
25
30

Fig. 5.9

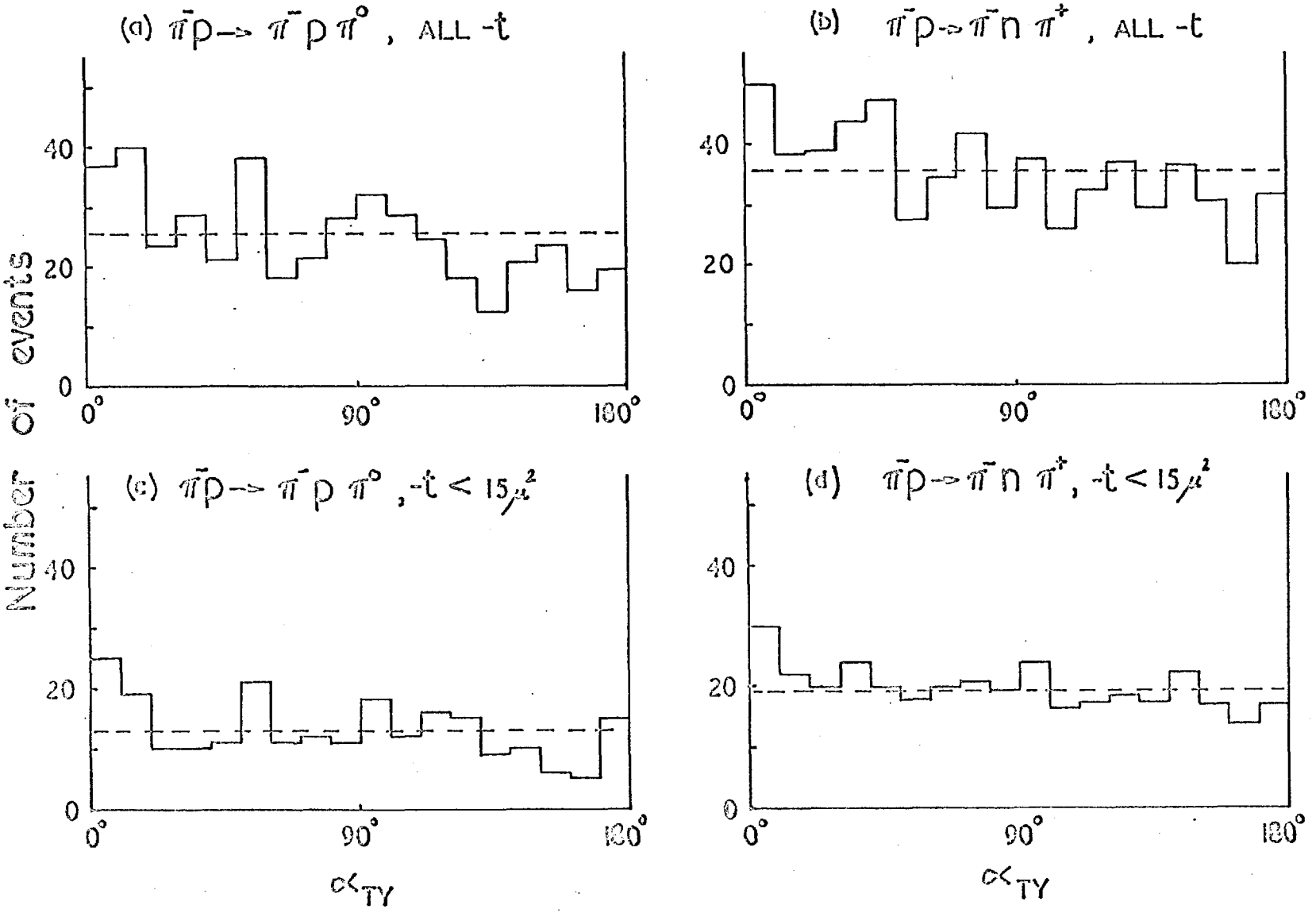

TREIMAN – YANG ANGLE DISTRIBUTIONS

Fig. 5.10

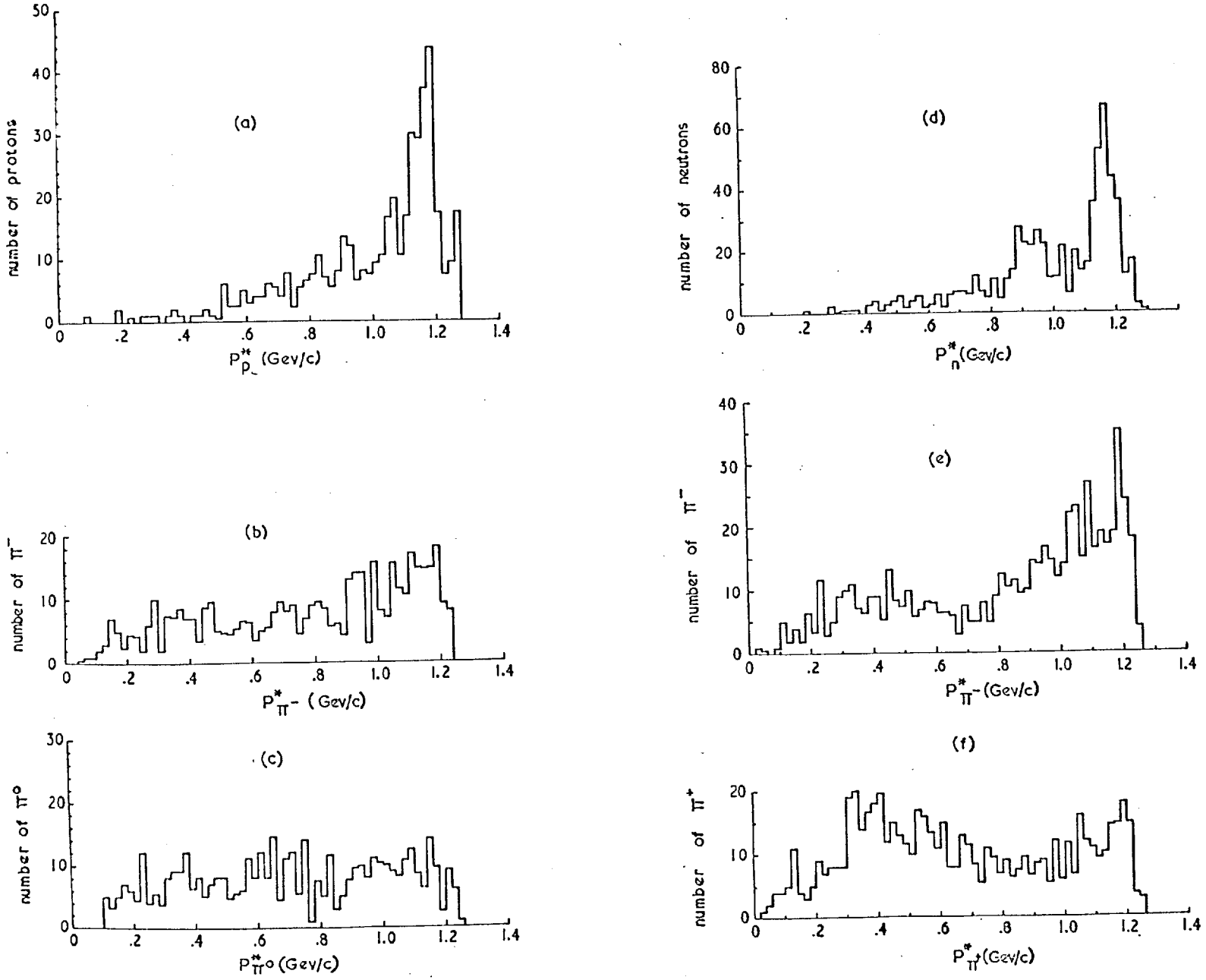
(a)
number of protons
$P^*_{p^-}$ (Gev/c)
(b)
number of π^-
$P^*_{\pi^-}$ (Gev/c)
(c)
number of π^o
$P^*_{\pi^o}$ (Gev/c)
(d)
number of neutrons
P^*_n(Gev/c)
(e)
number of π^-
$P^*_{\pi^-}$(Gev/c)
(f)
number of π^+
$P^*_{\pi^+}$(Gev/c)

Fig. 5.11

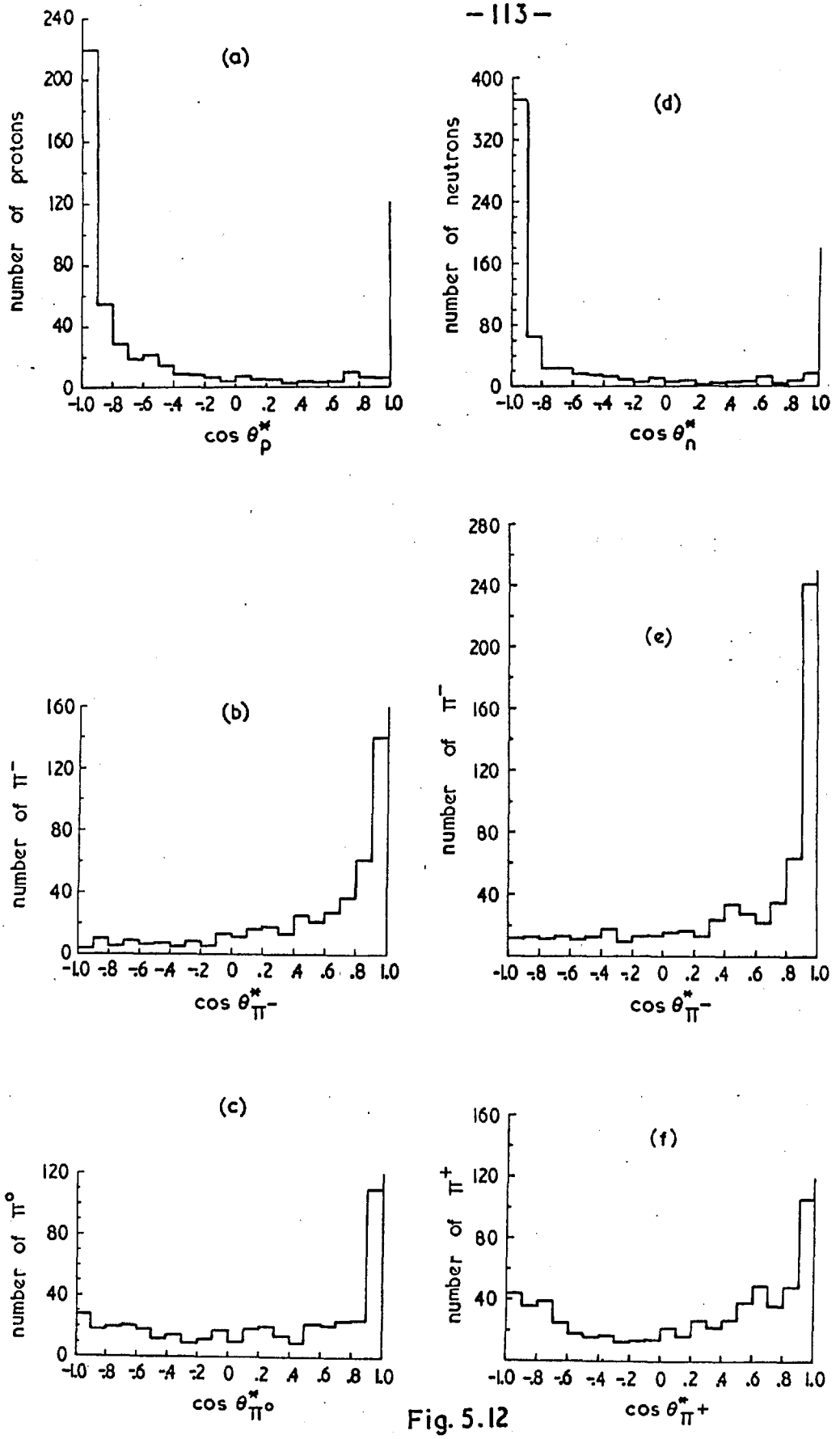
(a)
number of protons
240
200
160
120
80
40
0
-1.0 -.8 -.6 -.4 -.2 0 .2 .4 .6 .8 1.0
cos θ*p
(d)
number of neutrons
400
320
240
160
80
0
-1.0 -.8 -.6 -.4 -.2 0 .2 .4 .6 .8 1.0
cos θ*n
(b)
number of π⁻
160
120
80
40
0
-1.0 -.8 -.6 -.4 -.2 0 .2 .4 .6 .8 1.0
cos θ*π⁻
(e)
number of π⁻
280
240
200
160
120
80
40
-1.0 -.8 -.6 -.4 -.2 0 .2 .4 .6 .8 1.0
cos θ*π⁻
(c)
number of π°
120
80
40
0
-1.0 -.8 -.6 -.4 -.2 0 .2 .4 .6 .8 1.0
cos θ*π°
(f)
number of π⁺
160
120
80
40
-1.0 -.8 -.6 -.4 -.2 0 .2 .4 .6 .8 1.0
cos θ*π⁺

Fig. 5.12

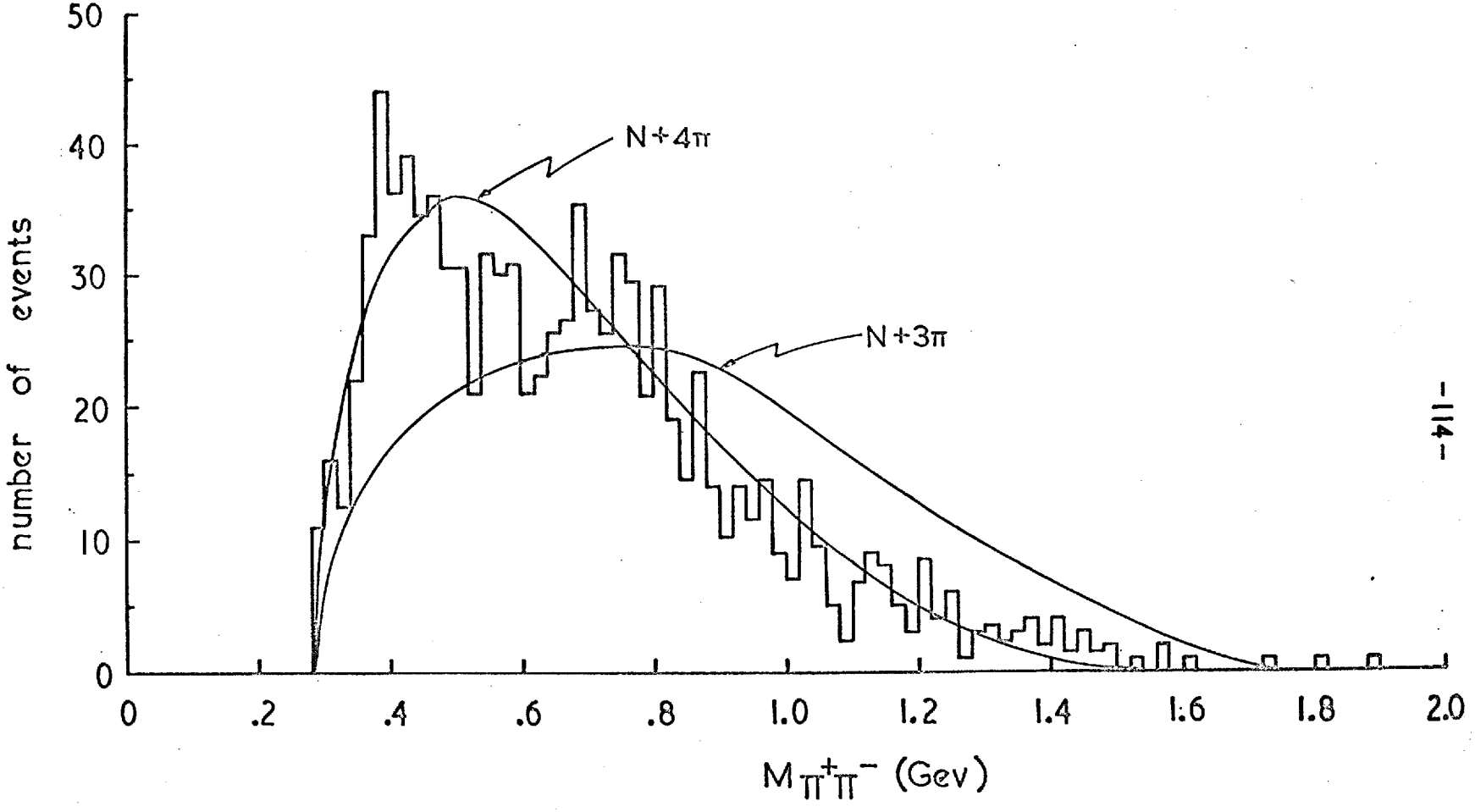
50
40
30
20
10
0
number of events
N+4π
N+3π
0
.2
.4
.6
.8
1.0
1.2
1.4
1.6
1.8
2.0
$M_{\pi^+\pi^-}$ (Gev)

Fig. 5.13

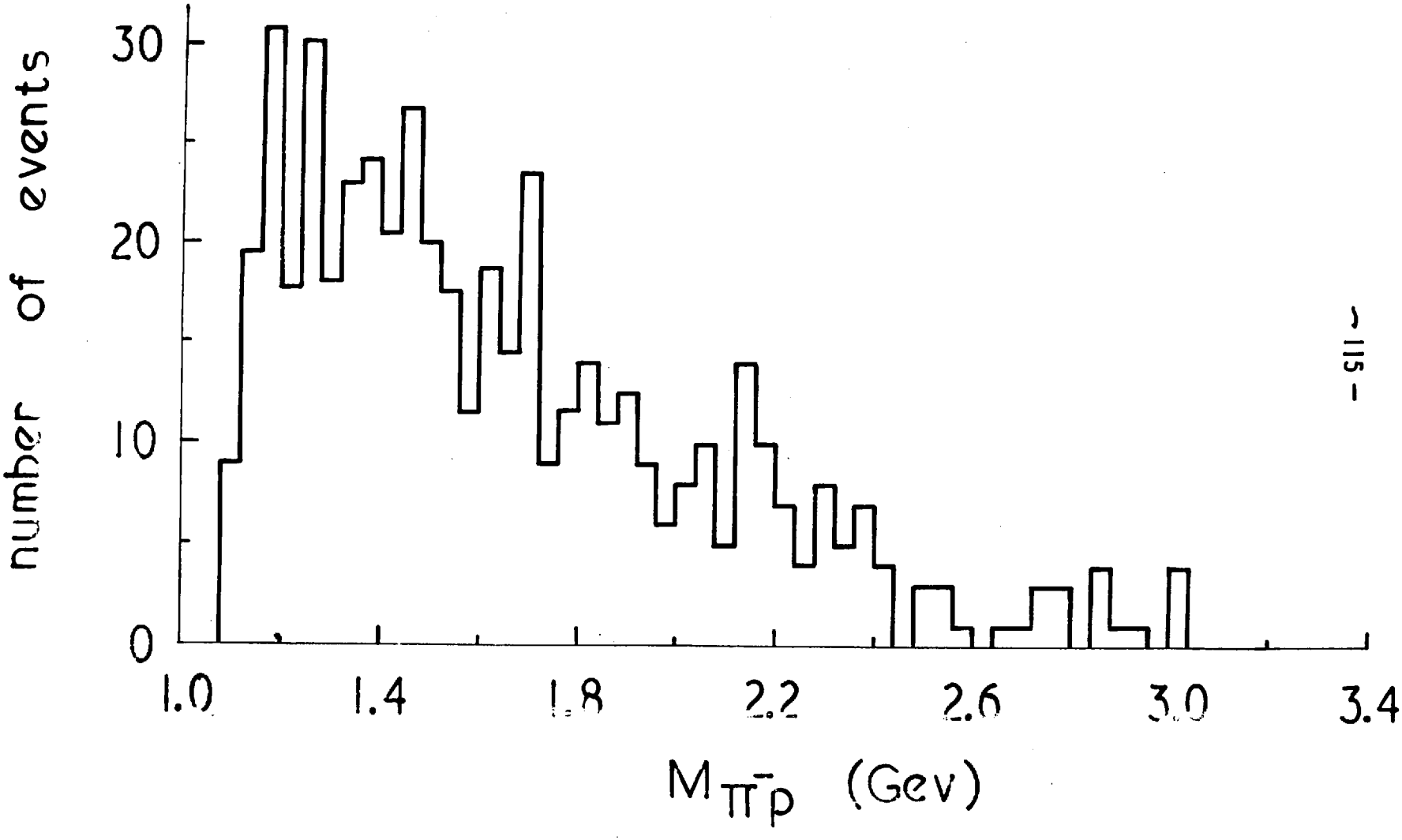

Fig. 5.14

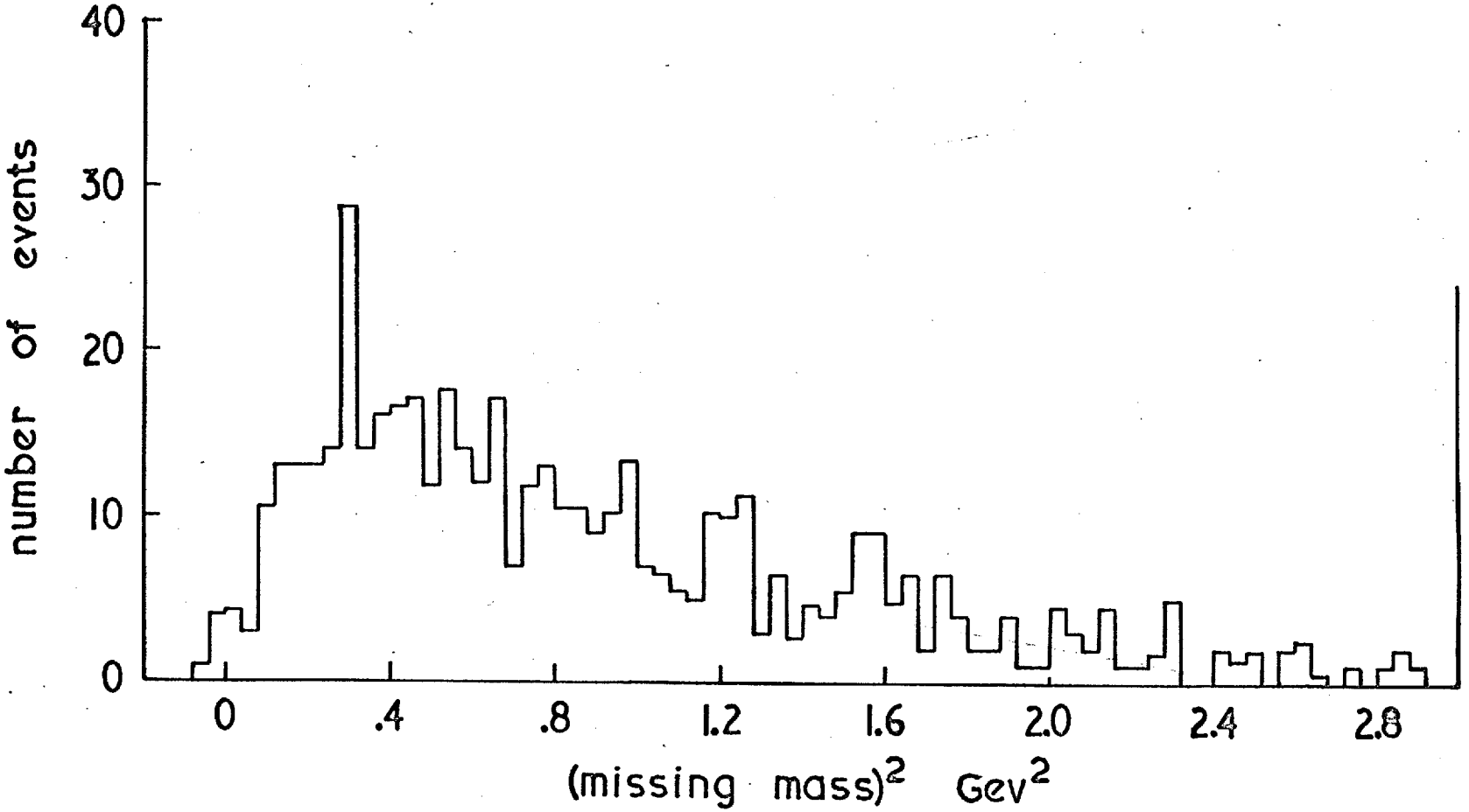
40
30
20
10
0
number of events
0
.4
.8
1.2
1.6
2.0
2.4
2.8
(missing mass)^2 Gev^2

Fig. 5.15

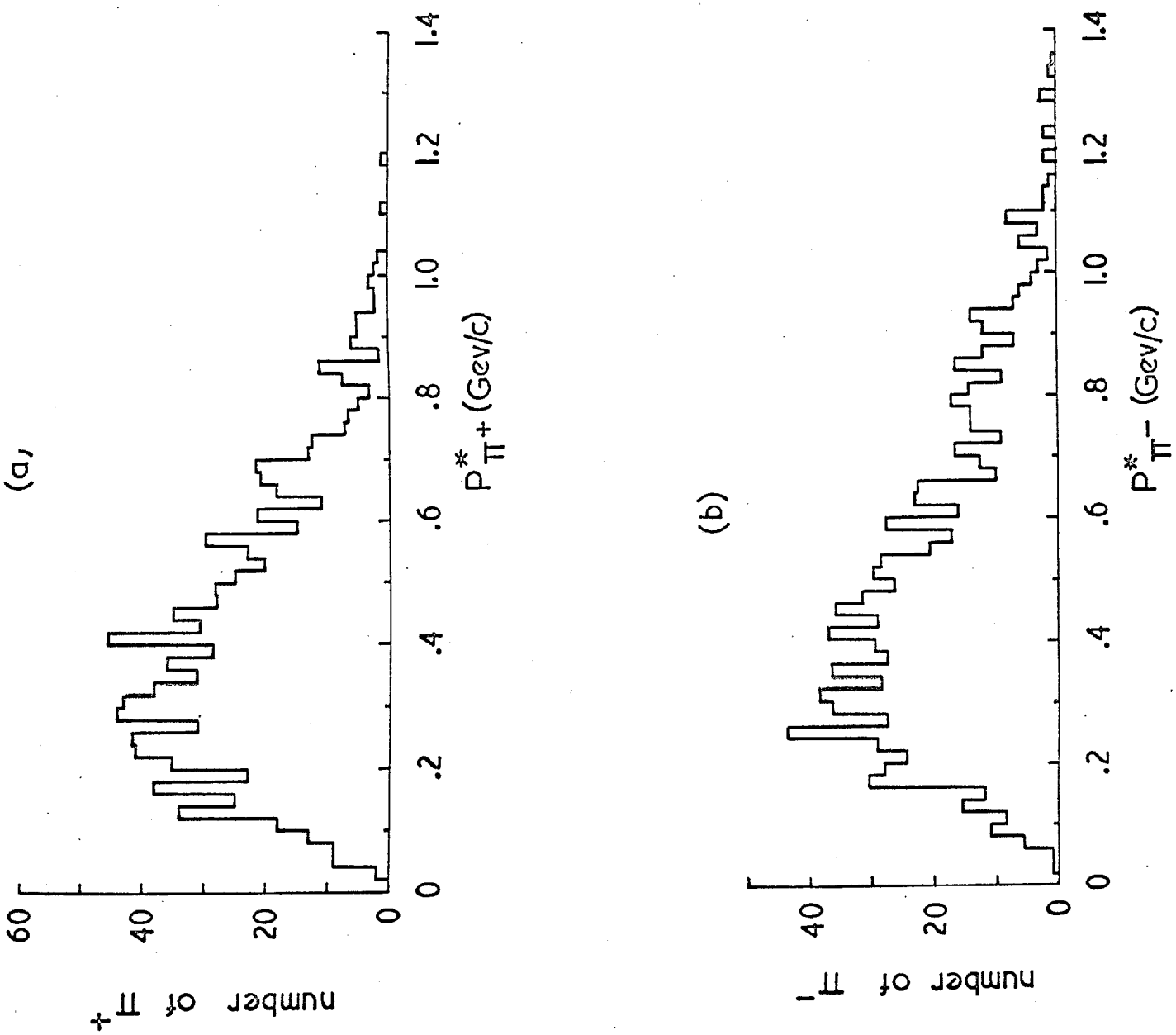
(a)
number of π^+
0
20
40
60
0
.2
.4
.6
.8
1.0
1.2
1.4
$P^*_{\pi^+}$ (Gev/c)
(b)
number of π^-
0
20
40
0
.2
.4
.6
.8
1.0
1.2
1.4
$P^*_{\pi^-}$ (Gev/c)

Fig. 5.16

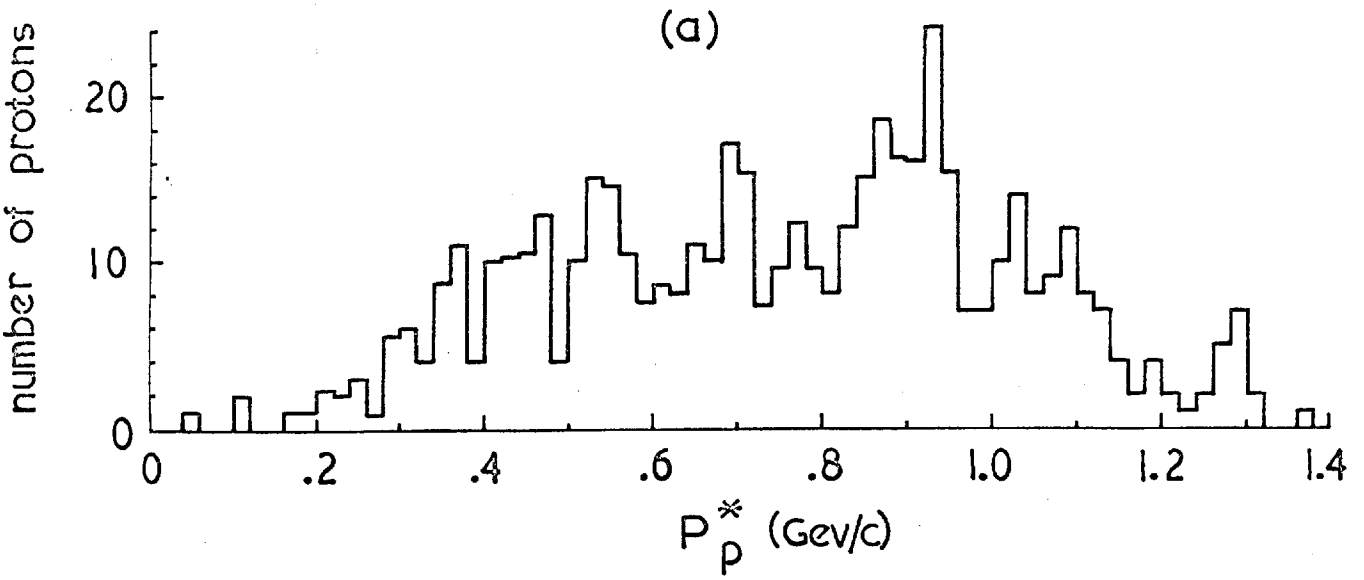
(a)
number of protons
20
10
0
0
.2
.4
.6
.8
1.0
1.2
1.4
P_p^* (Gev/c)

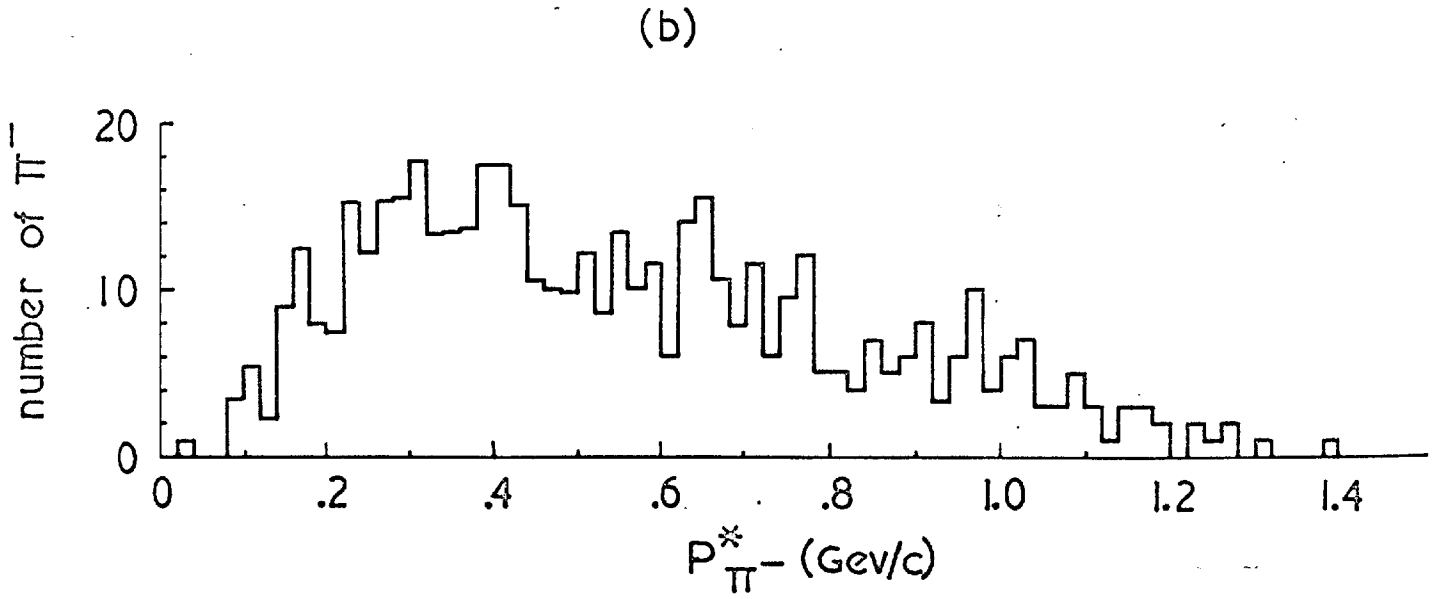
(b)
number of π^-
20
10
0
0
.2
.4
.6
.8
1.0
1.2
1.4
$P_{\pi^-}^*$ (Gev/c)

Fig. 5.17

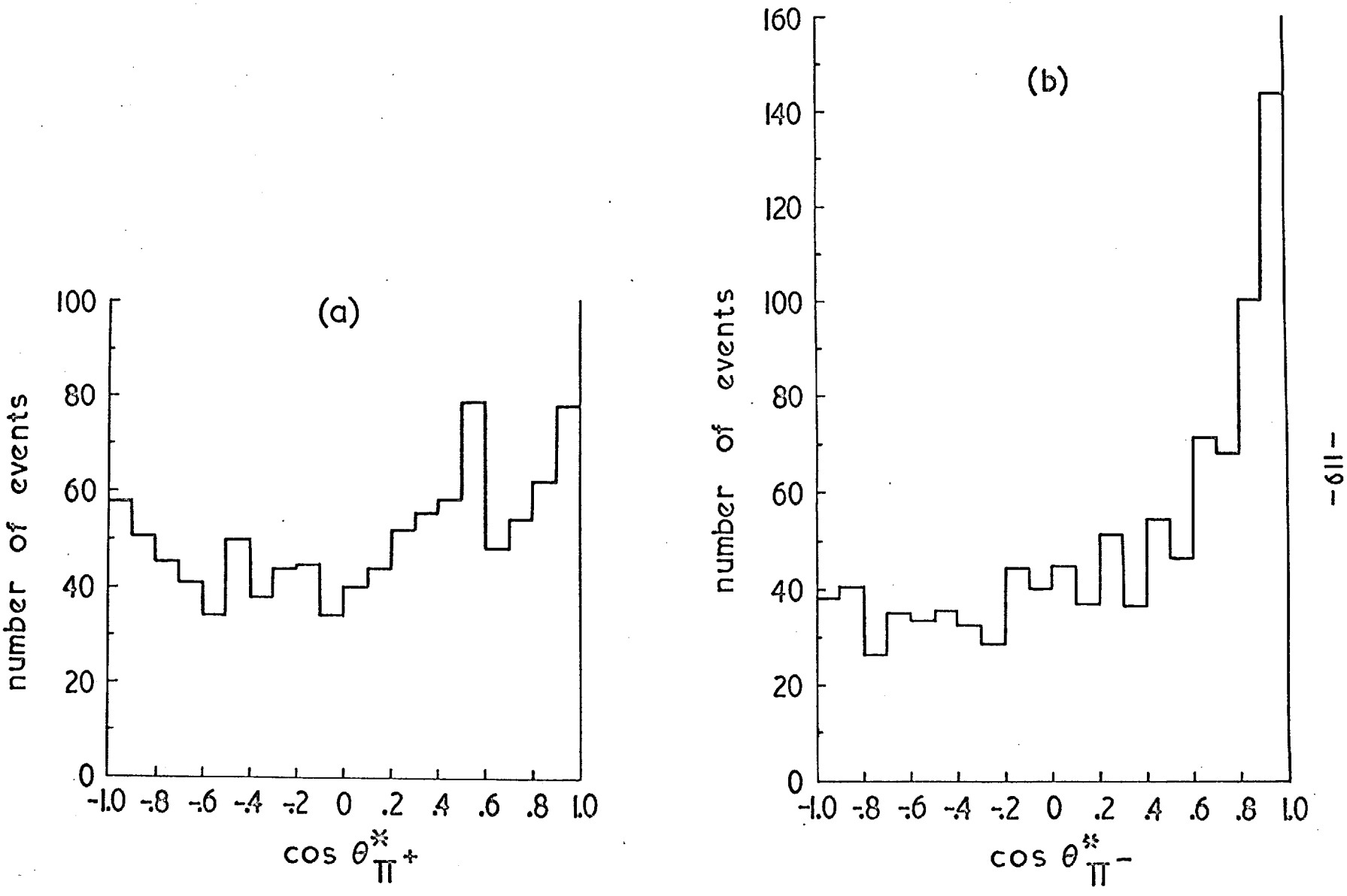
(a)
number of events
100
80
60
40
20
0
-1.0 -.8 -.6 -.4 -.2 0 .2 .4 .6 .8 1.0
cos θ* π+
(b)
number of events
160
140
120
100
80
60
40
20
0
-1.0 -.8 -.6 -.4 -.2 0 .2 .4 .6 .8 1.0
cos θ* π-

Fig. 5.18

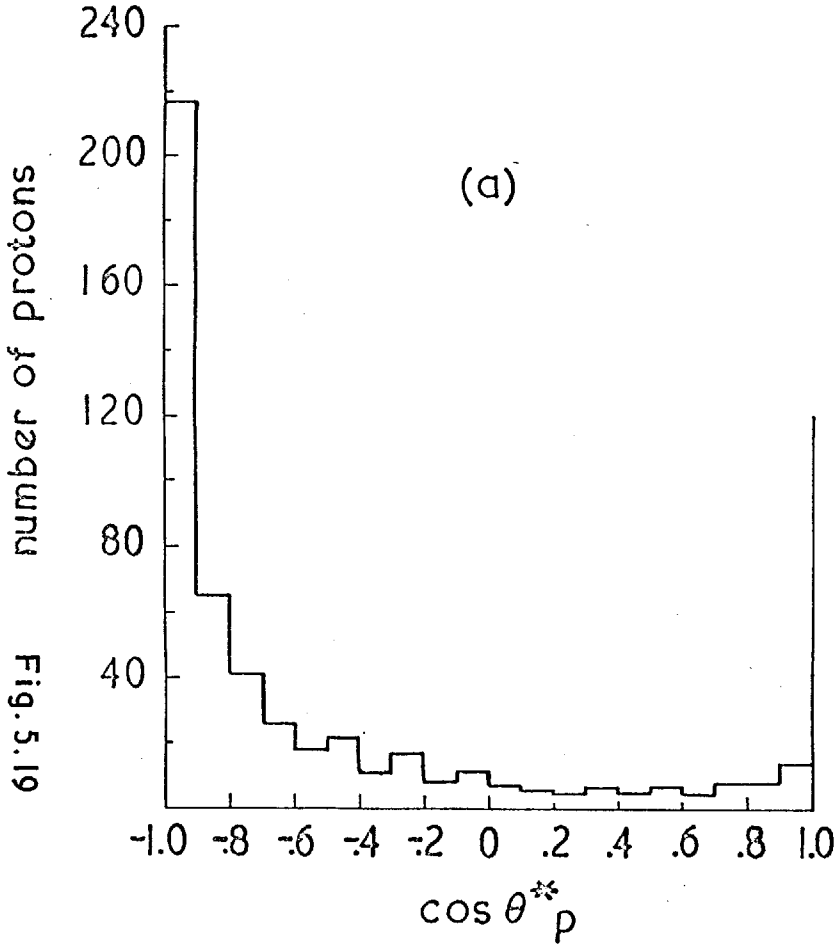
(a)
number of protons
240
200
160
120
80
40
-1.0 -.8 -.6 -.4 -.2 0 .2 .4 .6 .8 1.0
cos θ*p

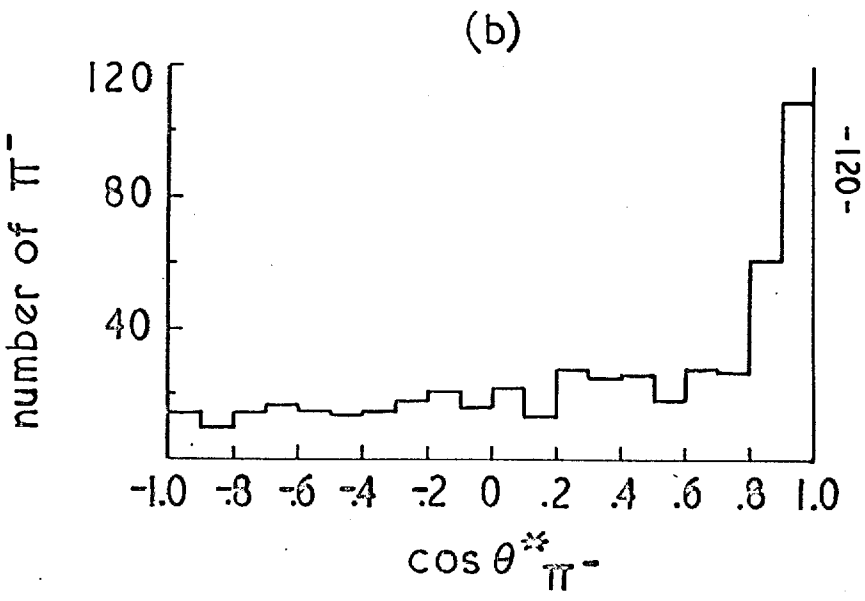
(b)
number of π⁻
120
80
40
-120-
-1.0 -.8 -.6 -.4 -.2 0 .2 .4 .6 .8 1.0
cos θ*π⁻

Fig. 5.19

CHAPTER VI

RESONANCE PRODUCTION

In this Chapter, the properties of the production and decay of both ρ and f^o mesons will be discussed in detail. The ρ^- was seen in the $\pi^- \pi^o$ system in reaction $\pi^- p \rightarrow p \pi^- \pi^o$ (I), and both ρ^o and f^o were seen in the $\pi^+ \pi^-$ system in the reaction $\pi^- p \rightarrow n \pi^+ \pi^-$ (II).

6.1. Mass Values and Widths.

The central values of both ρ^- and ρ^o were at (770±20) Mev, as seen in Figs. 5.5(a) and (b). The f^o has a central value of (1260±20) Mev. The computation of the width or lifetime of a resonant state depends on the assumption of a Breit-Wigner form for the resonance. This computation is made difficult due to uncertainty in subtracting background events. The widths quoted below were obtained from effective mass distributions plotted in 20 Mev intervals. The full widths at half maximum above phase space background were estimated to be Γ_{ρ^o} = (200±30) Mev, Γ_{ρ^-} = (180±30) Mev, Γ_{f^o} = (160±30) Mev. In these widths experimental errors estimated at 20 Mev, have not been unfolded. These widths represent a lifetime of the resonant states of about 10^{-23} sec., which is the same order of time as that taken for the resonance to escape the range of nuclear forces.

The central values are in agreement with those found by other workers, but the widths noticeably larger. Roos[15], in a review article on resonant states, has listed the masses and widths of all resonances found to date,

and quotes the following values for masses and widths of, ρ^-, ρ^o, f^o, averaged over all experiments finding them. All values are expressed in Mev.

$$M_{\rho^-} = (757 \pm 5); \; \Gamma_{\rho^-} = 120 \pm 10.$$

$$M_{\rho^o} = (751 \pm 6); \; \Gamma_{\rho^o} = 110 \pm 10.$$

$$M_{f^o} = 1253 \pm 20; \; \Gamma_{f^o} = 100 \pm 50.$$

There appears to be some evidence for increasing widths with increasing incident momentum. In particular, the following results were obtained for widths of ρ, and f^o, for incident pion momenta above 3Gev/c, and from single pion production reactions only.

Incident Pion Momentum (Gev/c)	Γ_{ρ^o}(Mev)	Γ_{ρ^-}(Mev)	Γ_{f^o}(Mev)	Reference.
3.0	130±30	130±30	70±20	Selove et al[27]
3.3	175	125	200	Guiragossian[69]
4.0	200±30	180±30	160±30	this experiment
6.1	~250	-	~200	Veillet et al[70]

Our increased widths seem to represent a real effect, since the experimental errors in the individual mass values (20 Mev) are negligible compared with the widths. In particular, our widths appear significantly larger than those found by Selove et al., especially in the case of f^o.

The width of the ρ^0 from the reaction $\pi^- p \rightarrow p \pi^+ \pi^- \pi^-$ studied in an earlier part of this experiment [55] was 130 ± 30 Mev. Samios et al[56] studied the same reaction at an incident momentum of 4.7 Gev/c and found a width of 170 ± 30 Mev for the ρ^0, consistent with our value.

6.2. Production Mechanisms of ρ and f^0.

From the effective mass distributions corresponding to events with all values of t, the cross-sections for production of ρ^-, ρ^0, and f^0 are found to be:

$$(\pi^- p \rightarrow n\rho^0) = (0.75 \pm 0.13) \text{ mb.}$$

$$(\pi^- p \rightarrow p\rho^-) = (0.45 \pm 0.08) \text{ mb.}$$

$$(\pi^- p \rightarrow n + f^0 \rightarrow \pi^+\pi^-) = (0.42 \pm 0.06) \text{ mb.}$$

Comparison of two prong and four prong events shows that the branching ratio $\left(\frac{f^0 \rightarrow \pi^+ \pi^+ \pi^- \pi^-}{f^0 \rightarrow \pi^+ \pi^-} \right) \leq 0.08 \pm 0.06$. No estimate of $f^0 \rightarrow K^+K^-$ has been made from our data. Calculations have suggested that $\frac{f^0 \rightarrow K^+K^-}{f^0 \rightarrow \pi^+\pi^-} \sim 0.1$ [58]. Hagopian[59] has presented some evidence for this decay mode and quotes a value of 0.1 ± 0.06 for the above ratio.

Our cross-section for f^0 production is consistent with that predicted from a calculation by Aitcheson[60].

The decay of the ρ^0 into four pions is also negligibly small. In the four prong events, only one event was seen in the 4π combinations in the ρ-region.

Figs. 6.1 and 6.2 show the Chew-Low plots for reactions I and II. These

again show how both the $\rho^{\pm,0}$ and f^0 are produced predominantly with low $|t|$. Fig. 6.3 shows the centre of mass angular distributions of the $\pi\pi$ systems in the regions of the ρ and f^0, again indicating the peripheral nature of the production processes. Selove et al.,[27] found a much weaker concentration of low $|t|$ events for the f^0 resonance. Of course, the concentration of low $|t|$ events for the mass region of the f^0 is not expected to be as great as for the ρ mass region. Fig. 6.2 shows the kinematic cut-off preventing the production of f^0 with $-t \leq 3\mu^2$. Lower values of $|t|$ can be reached with increasing incident momenta.

The presence of the resonant systems can be seen from the Dalitz plots of $(M_{\pi\pi}/\mu)^2$ against $(M_{\pi N}/\mu)^2$ for reactions I and II, shown in Fig. 6.4. The same plots, but with $-t \leq 15\ \mu^2$, are shown in Fig. 6.5. These latter plots show the resonance bands more clearly. The bands marked in the diagrams would correspond to the formation of the isobar, $N^*(3/2, 3/2)$. The events in the f^0 peak region, having mass values between $70\mu^2$ and $100\mu^2$, are seen to cluster on the right and left extremities of the plot for reaction II, heavily overlapping the isobar bands. Isobar formation cannot occur with single pion exchange in these reactions. If one considers that isobars could be formed either by ρ exchange (Figs. 6.6), or by a statistical model process, products of Clebsch-Gordon coefficients for upper and lower vertices indicate that one should expect equal cross-sections for the $N^*(n\pi^+)$ and $N^*(p\pi^0)$ isobar channels. It is seen, however, that there is no clustering in the isobar band $(p\pi^0)$ corresponding to f^0 mass

values in the Dalitz plot for reaction I. As will be seen below, this distribution of events can be readily explained by the decay of the spin two f^{o} meson. Incidentally, the Dalitz plot for reaction II displays conveniently, the asymmetric decay of the ρ^{o}.

6.3. Pion-Pion Scattering.

Figs. 6.7 and 6.8 show scatter diagrams of $(\frac{M_{\pi\pi}}{\mu})^2$ against the angle ϑ_{π^-} defined by

$$\cos\vartheta_{\pi^-} = \frac{(\vec{p}_{\pi^-} \wedge \vec{p}_{\pi^- \text{incident}})}{|(\vec{p}_{\pi^-} \wedge \vec{p}_{\pi^- \text{incident}})|} \qquad 6.1$$

where the incoming and outgoing π^- momenta are in the rest frame of the $\pi\pi$ system.

If only low $|t|$ events are selected, ϑ_{π^-} approximately represents the $\pi\pi$ scattering angle. Real $\pi - \pi$ scattering could only be studied if the unphysical limit $-t = -\mu^2$ were reached. Hagopian [59] has estimated the uncertainty of scattering angle due to the virtual pion being off the mass shell as

$$\Delta(\cos\vartheta_{\pi^-}) = \frac{t-1}{\omega^2}(1-\cos\vartheta_{\pi^-}) \qquad 6.2$$

Only events with $-t \lesssim 15\mu^2$ were therefore used. From these scatter diagrams one obtains in the ρ^- region, the characteristic $\ell=1$ $\cos^2\vartheta$ distribution. In the ρ^{o} region one obtains an asymmetrical distribution. Fig. 6.9 shows, for both reactions, the forward-backward asymmetry of this

scattering angle distribution as a function of the $\pi\pi$ effective mass. Where $\pi\pi$ scattering is dominated by a resonance, and no background exists, this asymmetry (F-B)/(F+B) will be zero. This criterion is satisfied at the ρ^- resonance energy for the $\pi^- \pi^o$ combination, but not for the $\pi^+ \pi^-$, as has been reported by several experimenters [32][61], and seems independent of incident energy. In our data, removal of the events in the 'ω' mass band does not remove the asymmetry, and hence does not seem to be caused by the postulated $\omega \rightarrow 2\pi$ decay mode[62] (see below).

Another explanation of this asymmetry could be the existence of some S-wave or D-wave background interference with the resonant p-wave. Selove et al[27] carried out a phase shift analysis of the $\pi\pi$ scattering. Although serious doubts can be cast on the methods used, their results did indicate the presence of a large T=0 S-wave phase shift and a small T=0 D-wave phase shift in the $\pi^+ - \pi^-$ scattering. This T= 0 wave cannot, of course, be present in $\pi^- \pi^o$ scattering. A phase shift analysis has not been carried out with the present data.

The asymmetry parameter also becomes zero for the $\pi^+ \pi^-$ combination at the mass of the f^o-meson, which is some confirmatory evidence for the interpretation of the f^o meson as a resonance in $\pi - \pi$ elastic scattering. The f^o meson is seen only in a T_z=0 isotopic spin state in the reaction

$$\pi^- p \quad — \quad n + f^o \hookrightarrow \pi^+ \pi^-$$

It is not seen in the reactions

$$\bar{\pi}\, p \longrightarrow p + f^{-} \hookrightarrow \pi^{-}\ \pi^{o}$$

$$\pi^{+} p \longrightarrow p + f^{+} \hookrightarrow \pi^{+}\ \pi^{o} \qquad (57)$$

which leads to the unambiguous assignment T=0. As the f^{o} has a large width, it presumably decays by strong interactions into the T=0 dipion system; it must have even spin, since pions obey Bose-Einstein statistics demanding symmetrical overall wave function. Two methods of determining the f^{o}-spin have been attempted with our data.

Firstly, the $\pi\pi$ scattering angle, ϑ_{π^-}, was compared with that expected from a resonance in a given angular momentum state. The angular distributions expected for a spin zero, two, and four are just the Legendre polynomials associated with a unique l-state.

i.e. $\left(\frac{d\sigma}{d\Omega}\right)_{l=o} = 1$; $\left(\frac{d\sigma}{d\Omega}\right)_{l=2} = \left|\frac{1}{2}(3\cos^2\vartheta-1)\right|^2$

$$\left(\frac{d\sigma}{d\Omega}\right)_{l=4} = \left|\frac{1}{8}\ (35\cos^4\vartheta - 30\cos^2\vartheta+3)\right|^2$$

The experimental distribution for events with $-t \leq 15\mu^2$, $70\mu^2 < \omega^2 < 100\mu^2$ and theoretical curves for spin two and four are shown in Fig. 6.11(a). Fig. 6.11(b)(c) shows the experimental distribution for events either side of the f^{o} resonance region. It can be seen that the distribution is inconsistent with spin zero and most consistent with spin two, although the expected hump at $\cos\vartheta_{\pi^-} = o$ is not seen convincingly in our data. It

must be remembered, however, that the uncertaintly due to off the mass shell scattering can be as large as 20% in the sample of f^o mesons found (equation 6.2). From the experimental distribution, one can also see how the clustering of f^c events is the isobar regions of the Dalitz plot occurs. The pions go preferentially forward and backward with respect to the f^o mesons, and hence with respect to the nucleon. Hence there is a preference for high and low πN masses along the f^o band of the plot.

Secondly, the $\pi\pi$ scattering cross-section was calculated for the ρ^o and f^o mass regions, using the Selleri modified Chew-Low formula, as described in Chapter 2.(equation 2.3). Only those events with $-t \leq 15\mu^2$ were selected for the integration over t. Figs. 6.12(a) and (b) show the cross-sections for the ρ^- and ρ^o region of the $\pi^- \pi^o$ and $\pi^+ \pi^-$ combinations respectively. It is seen that the formula is in excellent agreement with the cross-section of $12\pi\lambda\!\!\!^{-2}$ = 120 mb, expected at the peak of the ρ-resonance for 1 :1 $\pi\pi$ elastic scattering. This confirms the use of the Selleri formula, and therefore the formula was used with some confidence to deduce the $\pi - \pi$ cross section in the region of the f^o resonance. The inelasticity of $\pi\pi$ scattering is assumed small in the f^o region. (i.e. $\pi\pi \rightarrow$ KK assumed negligible). Fig. 6.12(c) compares the calculated cross-sections for a spin two resonance with that expected from the geometrical cross-section. The latter for a spin two resonance should be $\frac{4}{9}$ .20 $\pi\lambda\!\!\!^{-2}$ (31 mb. at f^o peak), allowance being made for

the π^o π^o decay mode of the f^o. It is seen that the calculated cross-sections are in good agreement with the expected value. The cross-section calculations were also carried out for an $l=0$ and $l=4$ spin assignment (The Selleri formula being l-dependent) and found to be in marked disagreement with the expected $\frac{4}{9} \cdot 4\pi\lambda^2$ and $\frac{4}{9} \cdot 36\pi\lambda^2$ expected from geometrical cross-sections.

The peak values thus found were :-

$(\pi^+ \pi^- \rightarrow \pi^+ \pi^-)$; ρ^o, = 105 ± 10 mb.

$(\pi^- \pi^o \rightarrow \pi^- \pi^o)$, ρ^-, 145 ± 15 mb.

$(\pi^+ \pi^- \rightarrow \pi^+ \pi^-)$, f^o, 26 ± 5 mb.

A similar value for the $\pi\pi$ cross-section for the ρ^o peak of (108±16)mb., again using the Selleri formula was found at an incident momentum of 1.59 Gev/c[32]. The only other group to calculate the $\pi\pi$ cross-section at the f^o peak, Selove et al., [27] found (5+1) mb. However, they used the Chew-Low formula without the Selleri correction. Their values for the $\pi\pi$ cross-section at the ρ^o and ρ^- peaks are also much lower than the expected geometrical values.

6.4 Two pion decay of the ω -meson.

It has been postulated that the presence of the ω^o meson in the mass region of the ρ^o could influence the ρ^o decay. The ω^o can decay into two pions only through an electromagnetic interaction. Glashow[63] suggested that the small $\rho - \omega$ mass difference may cause

electromagnetic interference between the two states to enhance this G-forbidden $\omega \rightarrow 2\pi$ decay. Bernstein and Feinberg[63] have suggested that this forbidden decay may be observed in the $\pi^+ \pi^-$ mass spectrum as a spike superimposed upon the broad ρ peak. Several experimenters have reported indications of structure in the ρ peak. Walker et al[64], found two distinctly different $\pi^+ \pi^-$ mass distributions in the ρ region at their two incident momenta of 1.9 and 2.1 Gev/c. They estimated a branching ratio for $\left(\omega \rightarrow 2\pi / \omega \rightarrow 3\pi \right)$ of 0.15 at 2.1 Gev/c. Firkinger et al[62], at an incident π^- momentum of 1.7 Gev/c, found a small excess of events at a mass of 790 Mev in the four-momentum range $0.25\ \text{Gev}^2 \leq -t \leq 0.7\ \text{Gev}^2$, and deduced a lower limit for $\left(\omega \rightarrow 2\pi / \omega \rightarrow 3\pi \right)$ of 0.05.

In the present data, there appears to be a slight excess of events at masses between 760 and 800 Mev. However, selection of events for different regions of momentum transfer indicates that these 'ω'-events are not preferentially associated with any particular region of momentum transfer. Fig. 6.10(b) and (c) shows the $\pi^+ \pi^-$ effective mass distribution for -t greater and smaller than $7\ \mu^2$. More statistics are required before any conclusion can be reached.

6.4. Conclusion.

In this experiment, two pion-pion resonances have been observed, the ρ and f^0 meson. The ρ -resonance had further confirmation of its properties, and more evidence for the asymmetry in the decay of the

ρ^{o} was obtained. No evidence for $\rho - \omega$ mixing was observed. To further understand this difference in ρ^{o} and ρ^{-} behaviour, more statistical accuracy is required to enable an unambiguous determination of $\pi\pi$ scattering phase shifts. The large widths are not readily explained, although some incident energy dependence can be seen by comparison with other experiments. Isobar formation appears to be negligible at this energy, compared with experiments at lower energies, although the only pure isospin state, $n\,\pi^{-}$ $(T = {}^{3}/_{2},\ T_{z} = -{}^{3}/_{2})$, can only be formed by the exchange of a doubly charged particle. It is to be expected that as the incident momentum increases peripheral production mechanisms become more important, giving the nucleon less chance to resonate with the pions.

Previous experiments had been unable to determine the spin of the f^{o} unambiguously. In the present experiment, the decay angular distributions and a calculation of the $\pi - \pi$ cross-sections has led to an assignment of spin two. The properties of the f^{o} meson can thus be summarised as follows: mass, (1260 ± 20) Mev, $\Gamma = (160 \pm 30)$ Mev, $J^{PG} = 2^{++}$. It has been suggested that this f^{o} resonance satisfies all the requirements of a Regge-pole "vacuum trajectory" particle[65]. However, as confirmed from a study of elastic scattering in this experiment, there appears to be no shrinkage of the diffraction peak with increasing energy, a necessary requirement if a single Regge trajectory is to dominate the scattering. Thus, at present, the simple Regge theory cannot explain existing data. An important test of the theory would consist of studying the $\pi - \pi$ system at higher

effective masses, to look for higher spin states along the trajectory. Recently, a second trajectory has been postulated, which should manifest itself as a T=0 $\pi\pi$ resonance at 1800 Mev.(66)

Thus it appears there are many reasons for doing an experiment at higher incident momenta. To produce a larger number of peripheral f^{o}'s, a higher incident momentum is required, say 6-7 Gev/c. With low $|t|$ the off-energy shell effect is smaller, and hence the interpretation in terms of $\pi - \pi$ scattering more certain. The same experiment would also be useful to explore the $\pi - \pi$ system at higher mass-values. At 6-7 Gev/c, however, bubble chamber experiments would be pushed to the limit of their accuracy, unless the distortions in present bubble chambers can be reduced significantly.

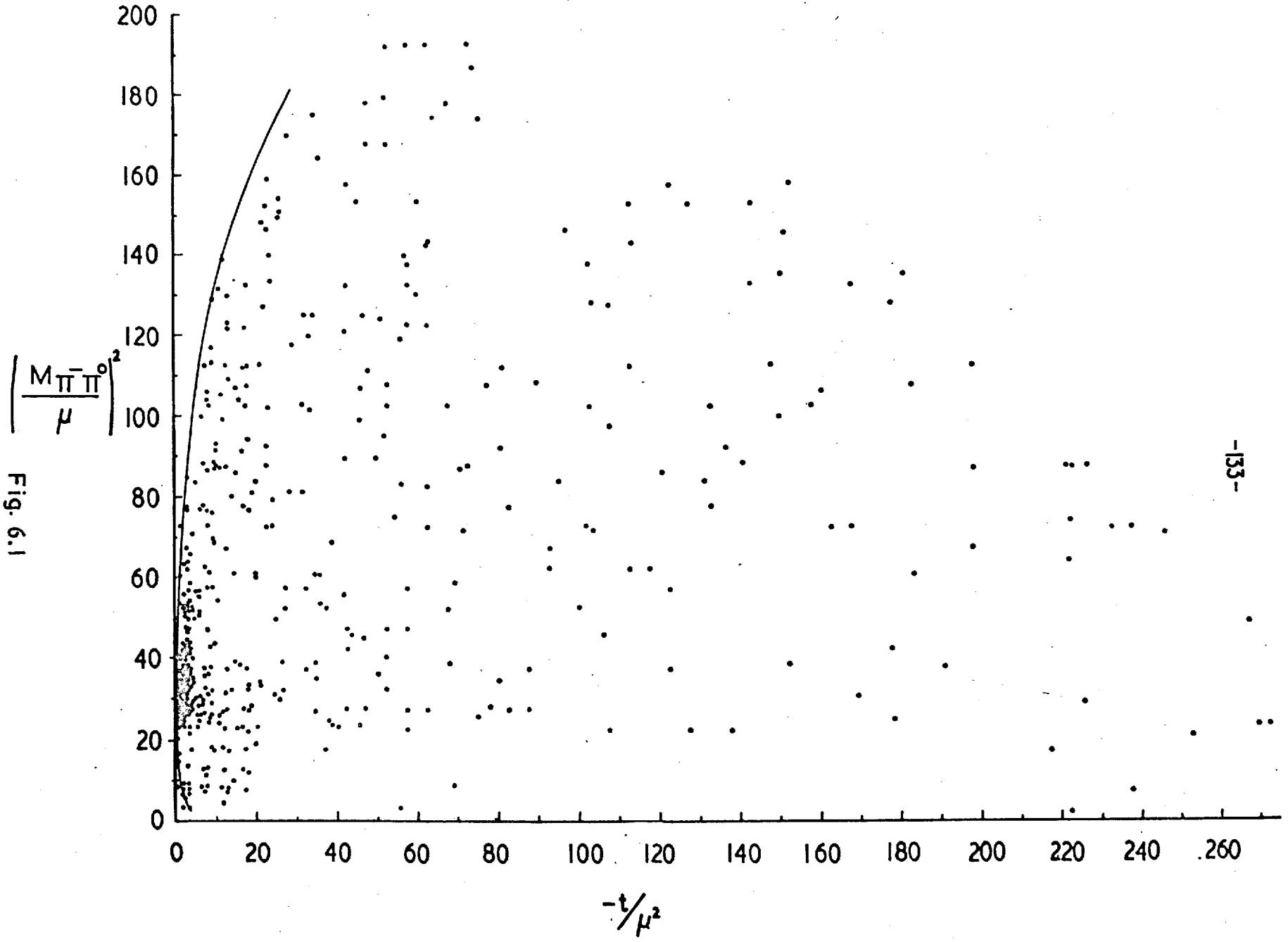
200
180
160
140
120
100
80
60
40
20
0
$\left|\frac{M_{\pi^-\pi^0}}{\mu}\right|^2$
0
20
40
60
80
100
120
140
160
180
200
220
240
260
$-t/\mu^2$

Fig. 6.1

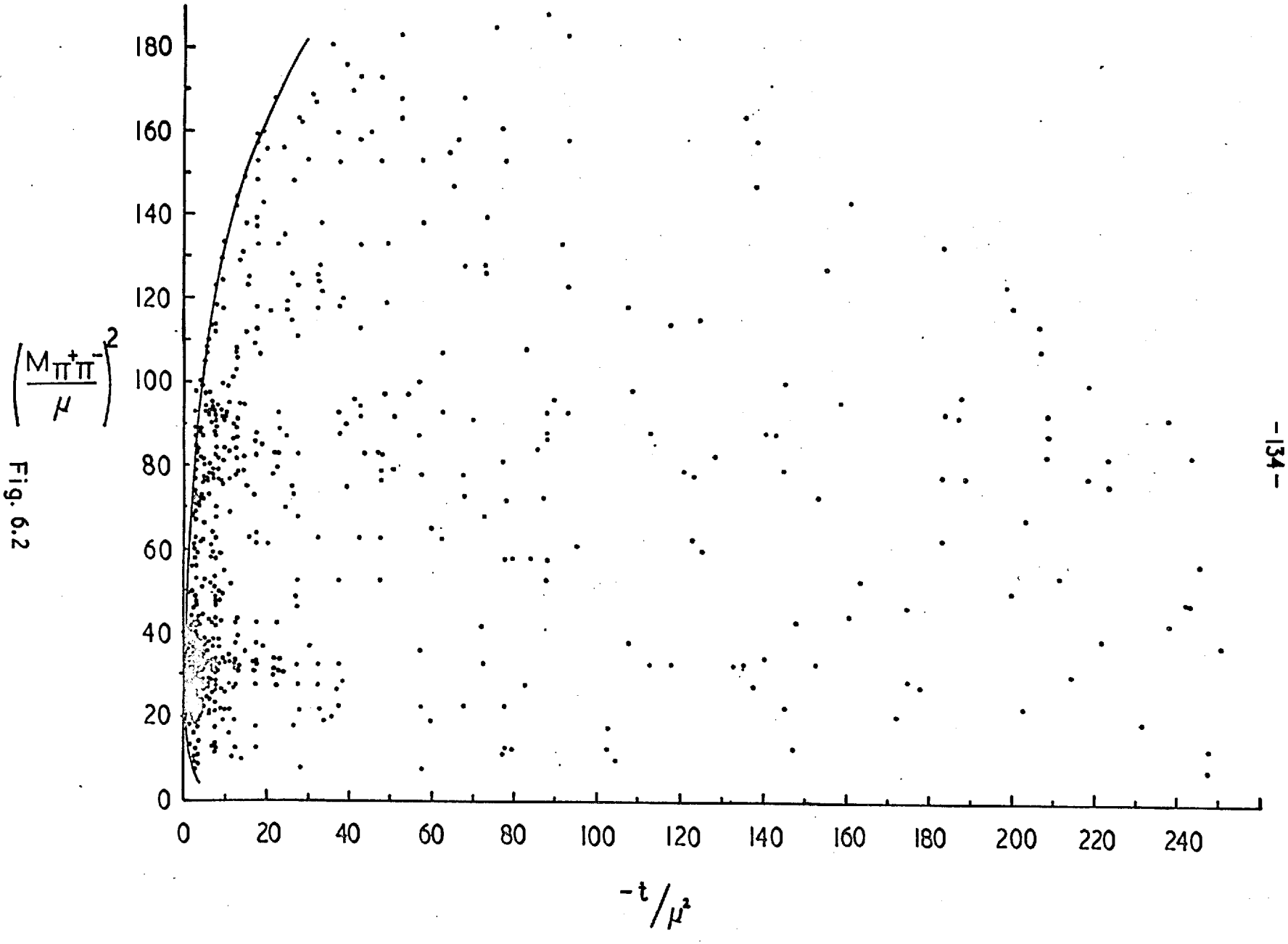
$\left(\frac{M_{\pi^+\pi^-}}{\mu}\right)^2$
180
160
140
120
100
80
60
40
20
0
0
20
40
60
80
100
120
140
160
180
200
220
240
$-t/\mu^2$

Fig. 6.2

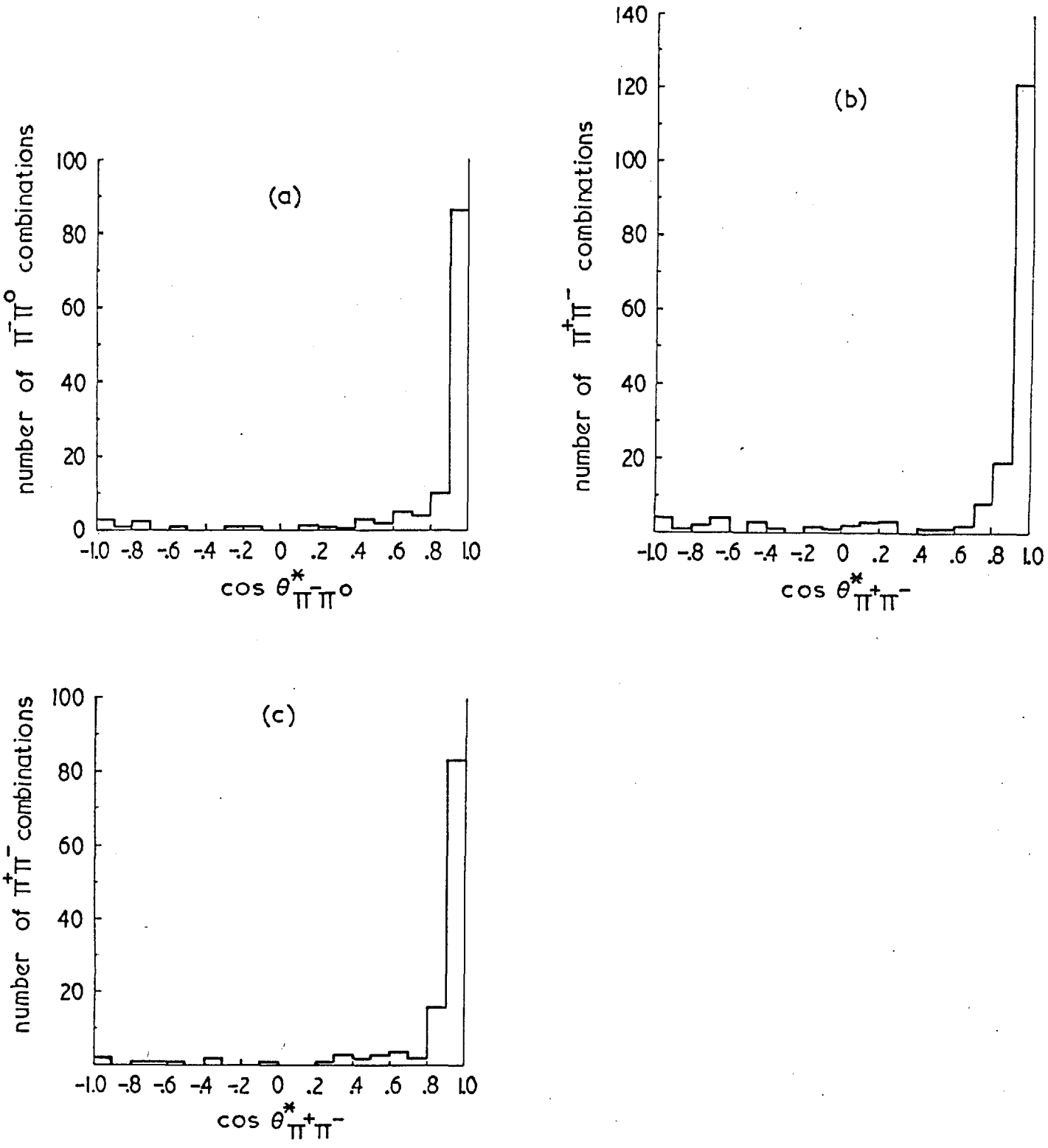
(a)
number of $\pi^-\pi^0$ combinations
100
80
60
40
20
0
-1.0 -.8 -.6 -.4 -.2 0 .2 .4 .6 .8 1.0
$\cos\theta^*_{\pi^-\pi^0}$
(b)
number of $\pi^+\pi^-$ combinations
140
120
100
80
60
40
20
-1.0 -.8 -.6 -.4 -.2 0 .2 .4 .6 .8 1.0
$\cos\theta^*_{\pi^+\pi^-}$
(c)
number of $\pi^+\pi^-$ combinations
100
80
60
40
20
-1.0 -.8 -.6 -.4 -.2 0 .2 .4 .6 .8 1.0
$\cos\theta^*_{\pi^+\pi^-}$

Fig. 6.3

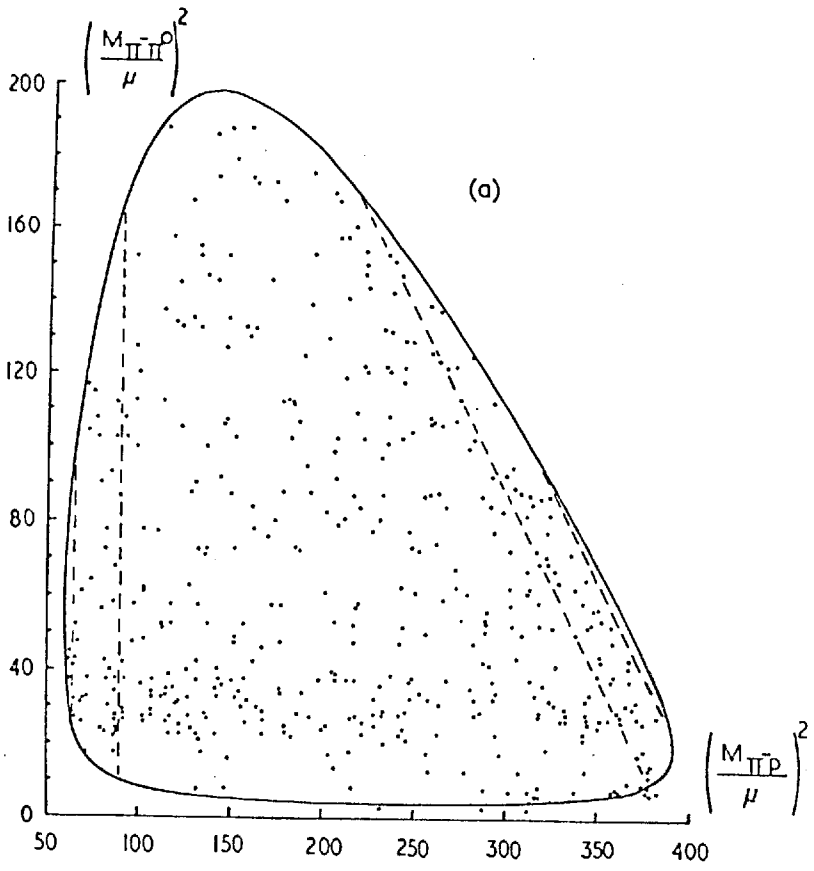
$\left(\frac{M_{\pi^-\pi^0}}{\mu}\right)^2$
200
160
120
80
40
0
50
100
150
200
250
300
350
400
(a)
$\left(\frac{M_{\pi^-p}}{\mu}\right)^2$

Fig. 6.4

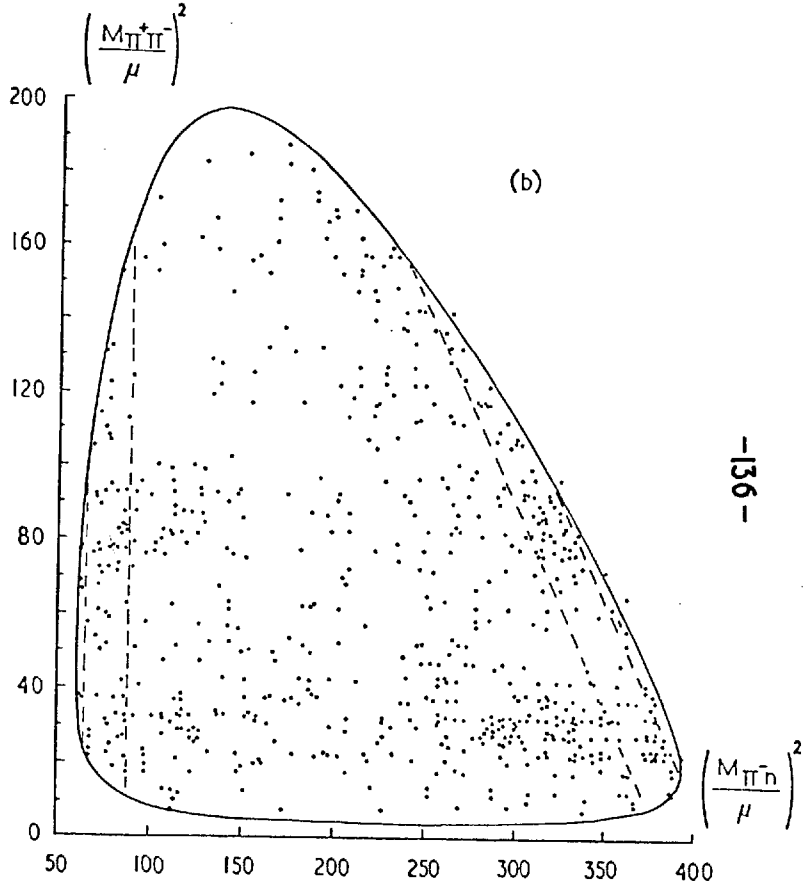
$\left(\frac{M_{\pi^+\pi^-}}{\mu}\right)^2$
200
160
120
80
40
0
50
100
150
200
250
300
350
400
(b)
$\left(\frac{M_{\pi^-n}}{\mu}\right)^2$

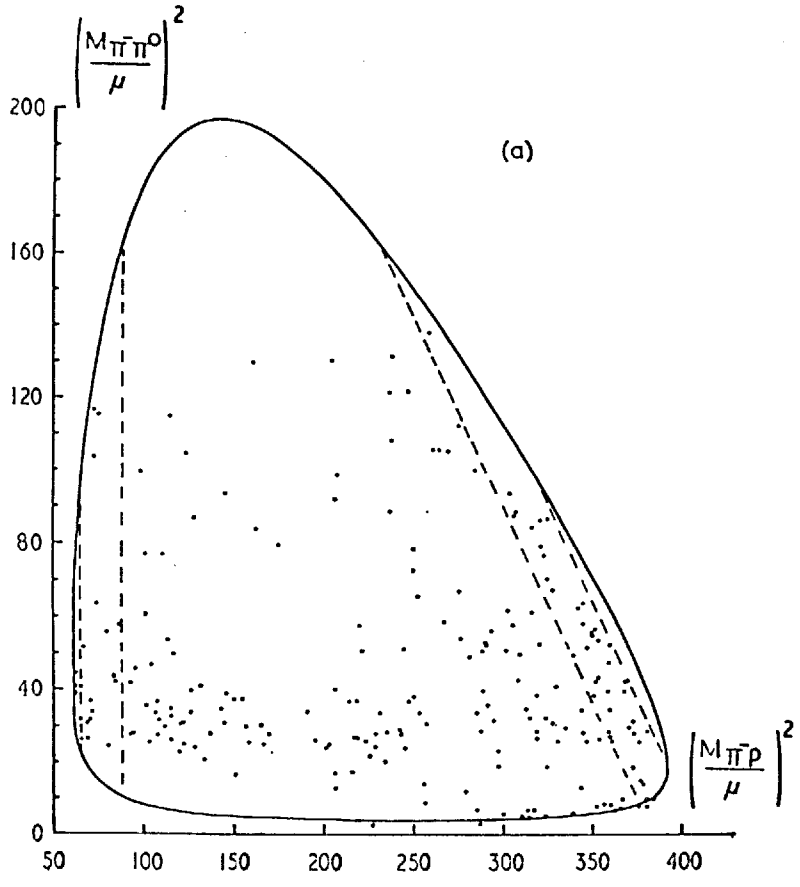
$\left(\frac{M_{\pi^-\pi^0}}{\mu}\right)^2$
(a)
200
160
120
80
40
0
50
100
150
200
250
300
350
400
$\left(\frac{M_{\pi^-p}}{\mu}\right)^2$

Fig. 6.5

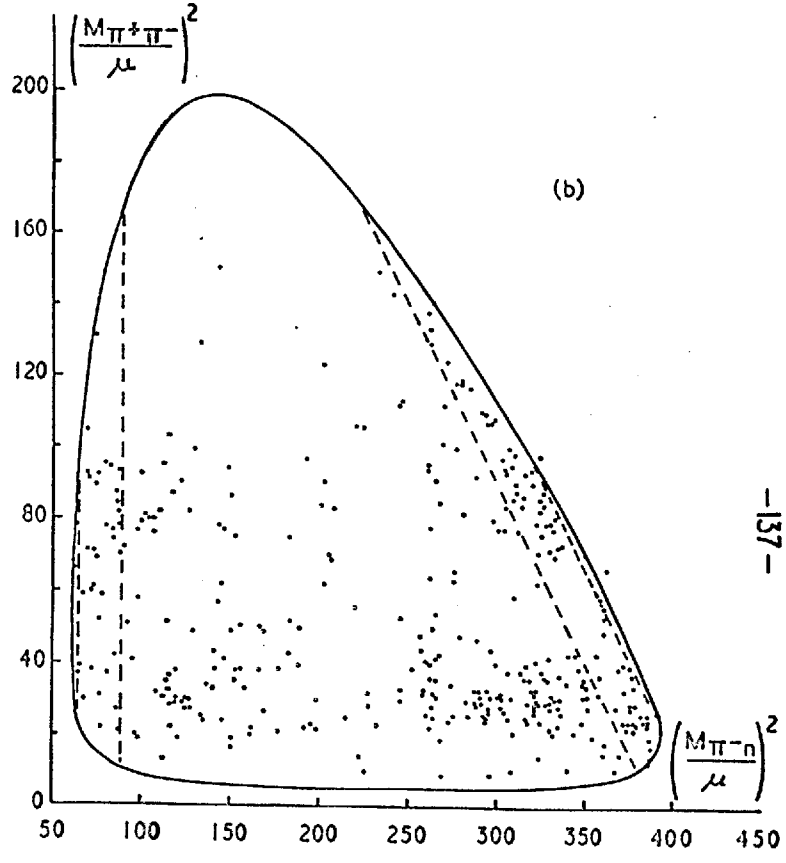
$\left(\frac{M_{\pi^+\pi^-}}{\mu}\right)^2$
(b)
200
160
120
80
40
0
50
100
150
200
250
300
350
400
450
$\left(\frac{M_{\pi^-n}}{\mu}\right)^2$

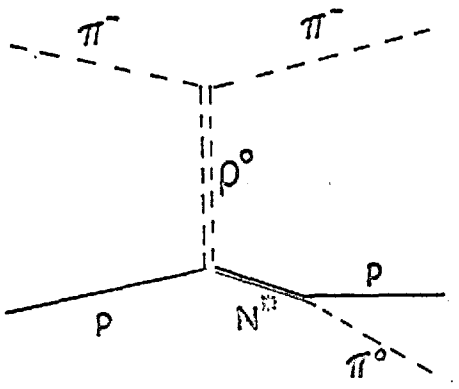

(a) $\pi^- p \rightarrow N^{*} \pi^-$
$\hookrightarrow p \pi^0$

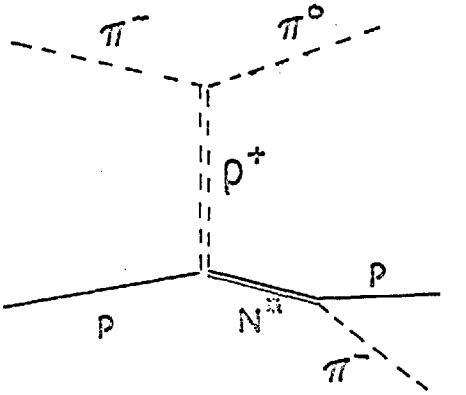

(b) $\pi^- p \rightarrow N^{*} \pi^0$
$\hookrightarrow p \pi^-$

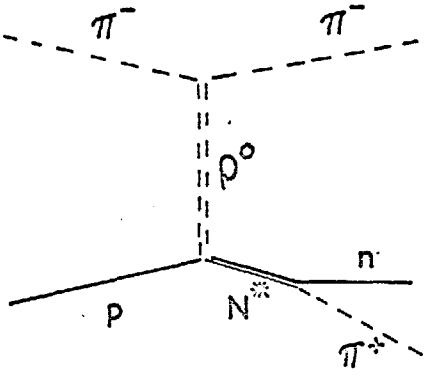

$\pi^- p \rightarrow N^{*} \pi^-$
$\hookrightarrow n \pi^+$

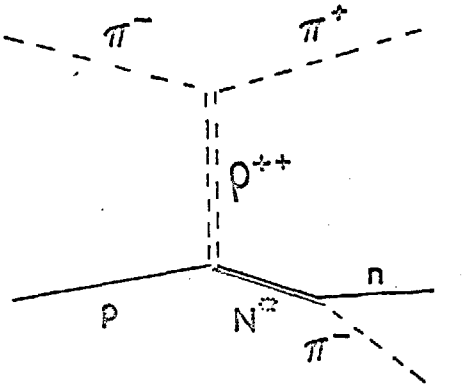

$\pi^- p \rightarrow N^{*} \pi^+$
$\hookrightarrow n \pi^-$

ISOBAR PRODUCTION BY ρ-EXCHANGE

Fig. 6.6

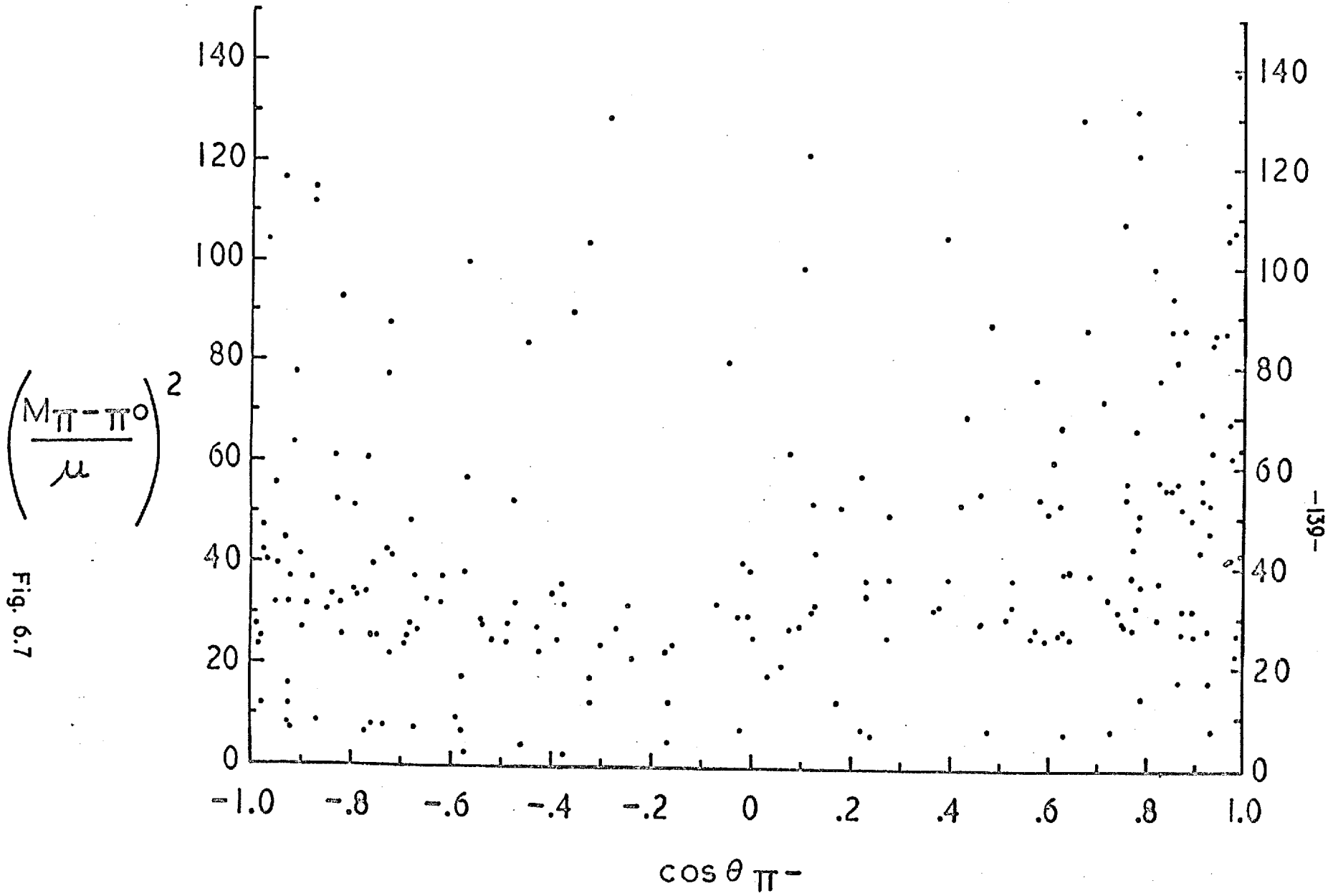
$\left(\frac{M_{\pi^-\pi^0}}{\mu}\right)^2$
140
120
100
80
60
40
20
0
-1.0
-.8
-.6
-.4
-.2
0
.2
.4
.6
.8
1.0
$\cos\theta_{\pi^-}$

Fig. 6.7

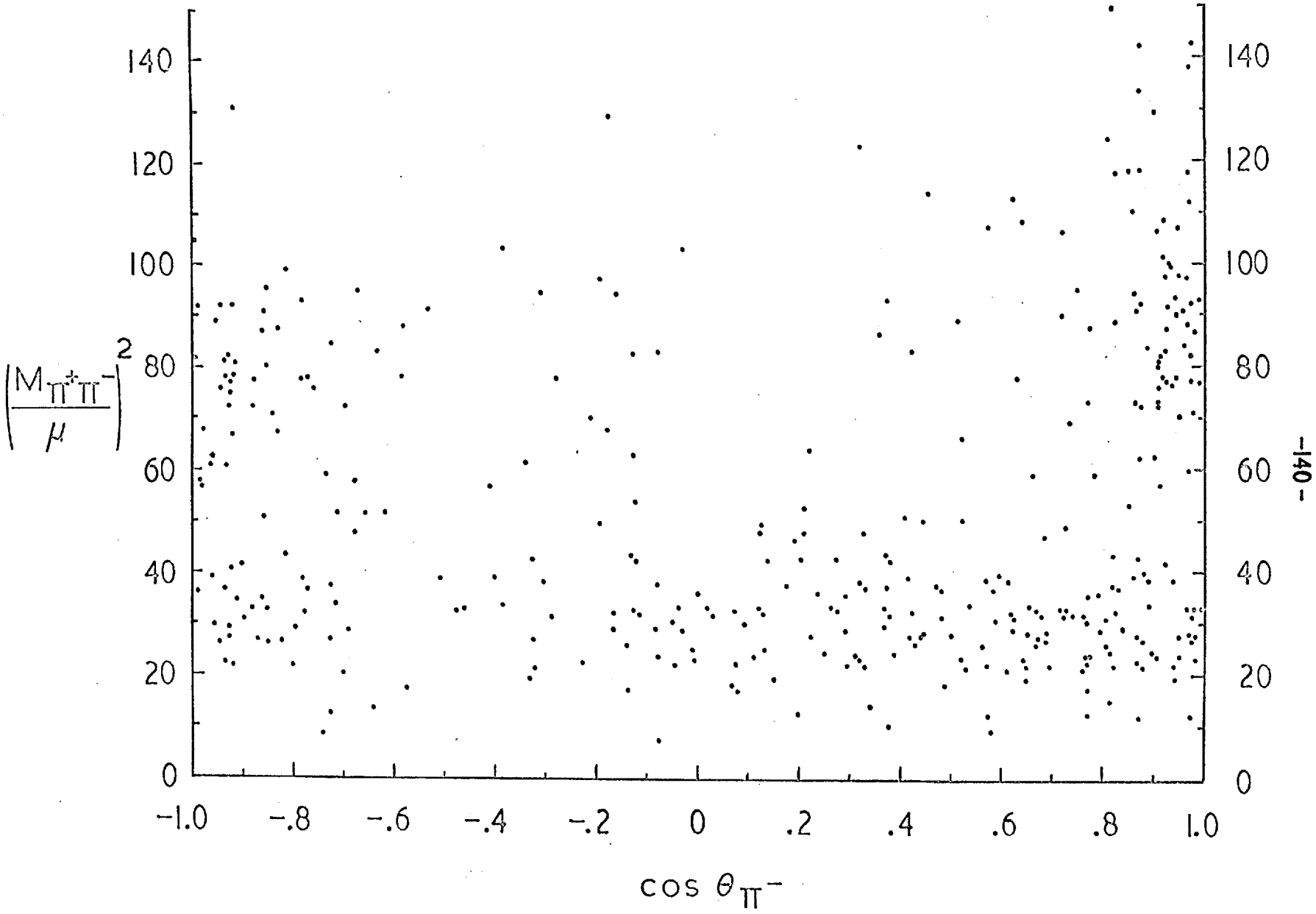
140
120
100
80
60
40
20
0
$\left(\frac{M_{\pi^+\pi^-}}{\mu}\right)^2$
-1.0
-.8
-.6
-.4
-.2
0
.2
.4
.6
.8
1.0
$\cos\theta_{\pi^-}$

Fig. 6.8

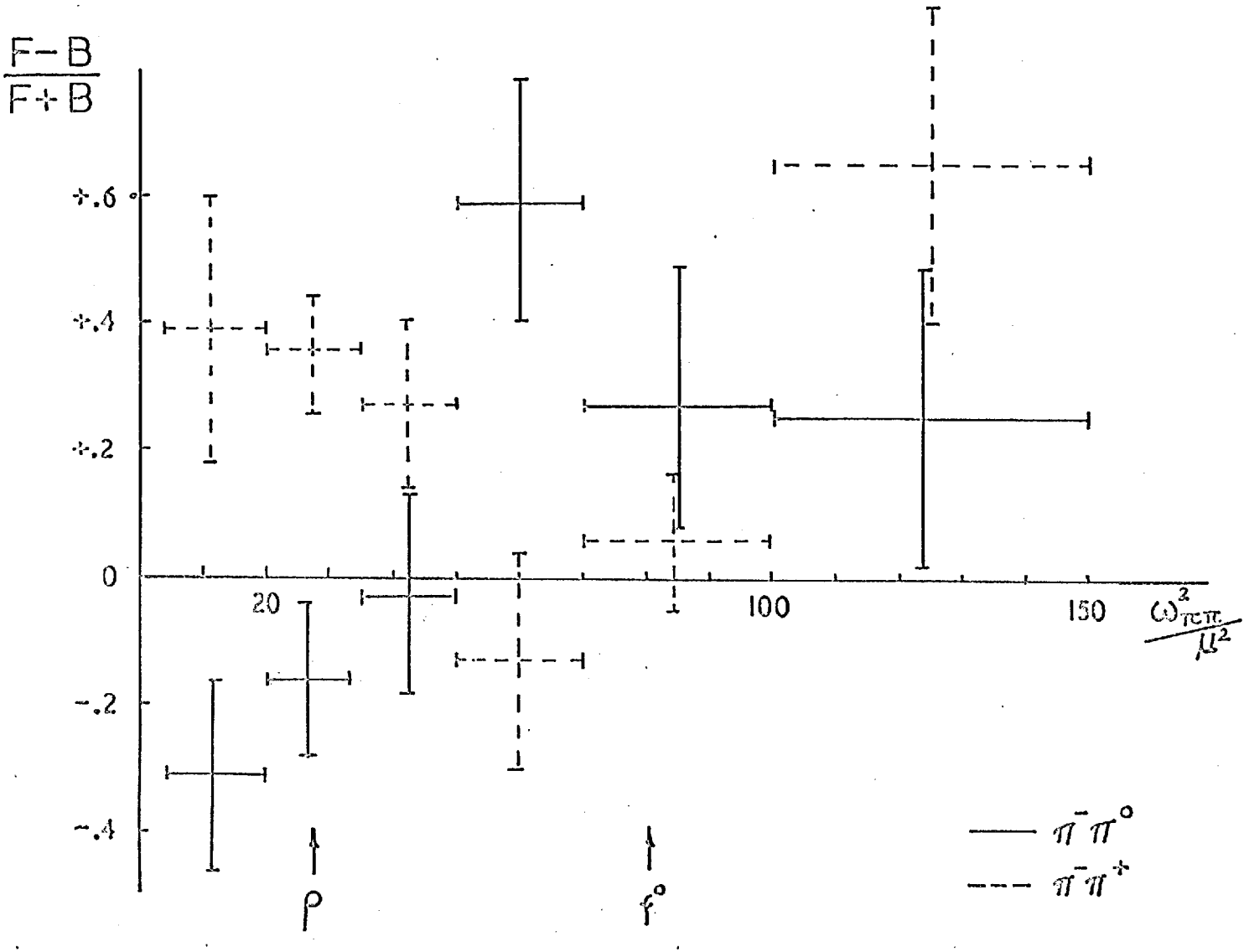

FORWARD - BACKWARD DECAY ASYMMETRY

Fig. 6.9

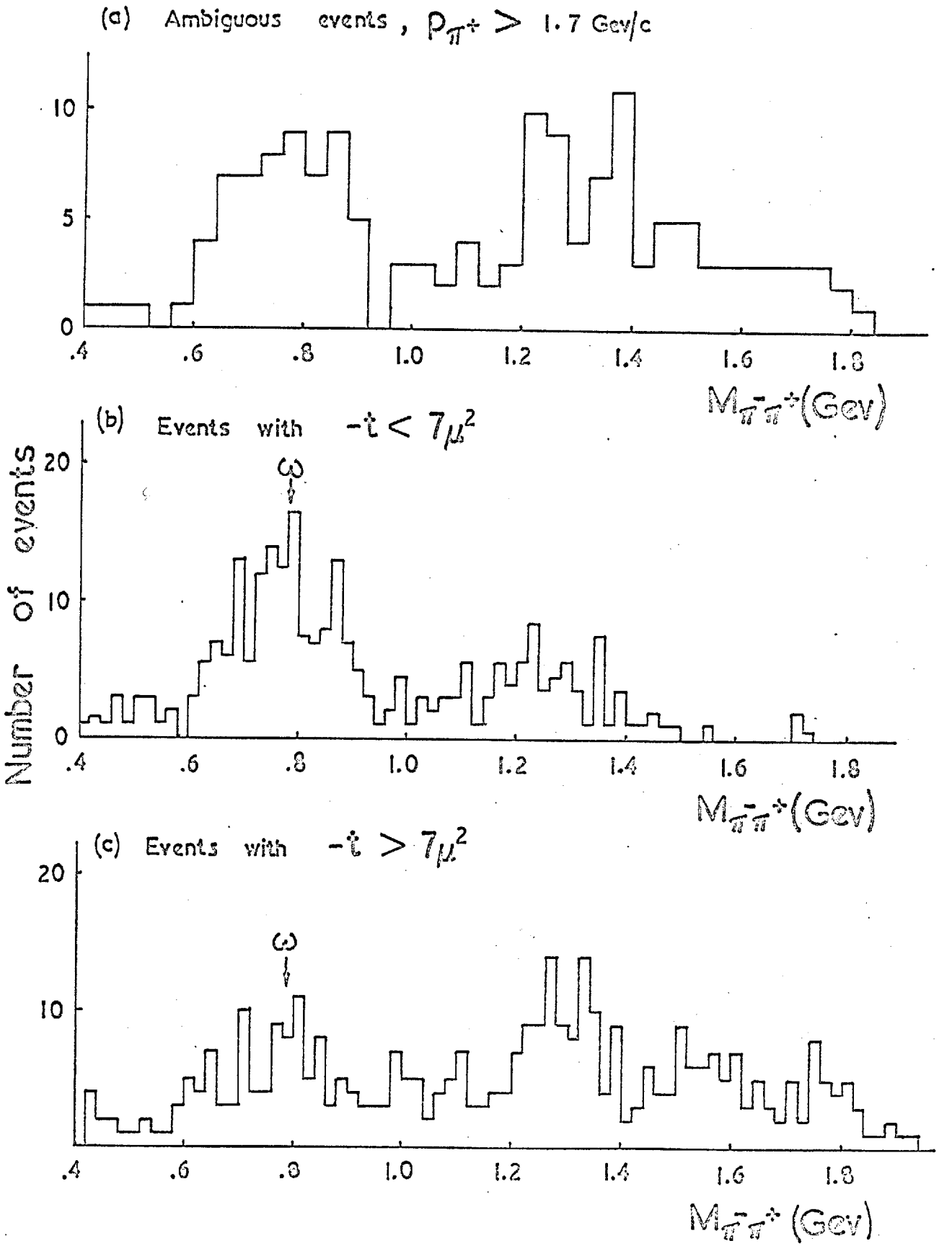
(a) Ambiguous events , $p_{\pi^+} > 1.7$ Gev/c
10
5
0
.4
.6
.8
1.0
1.2
1.4
1.6
1.8
$M_{\pi^-\pi^+}$(Gev)
(b) Events with $-t < 7\mu^2$
Number of events
20
10
0
ω
.4
.6
.8
1.0
1.2
1.4
1.6
1.8
$M_{\pi^-\pi^+}$(Gev)
(c) Events with $-t > 7\mu^2$
20
10
ω
.4
.6
.8
1.0
1.2
1.4
1.6
1.8
$M_{\pi^-\pi^+}$ (Gev)

Fig. 6.10

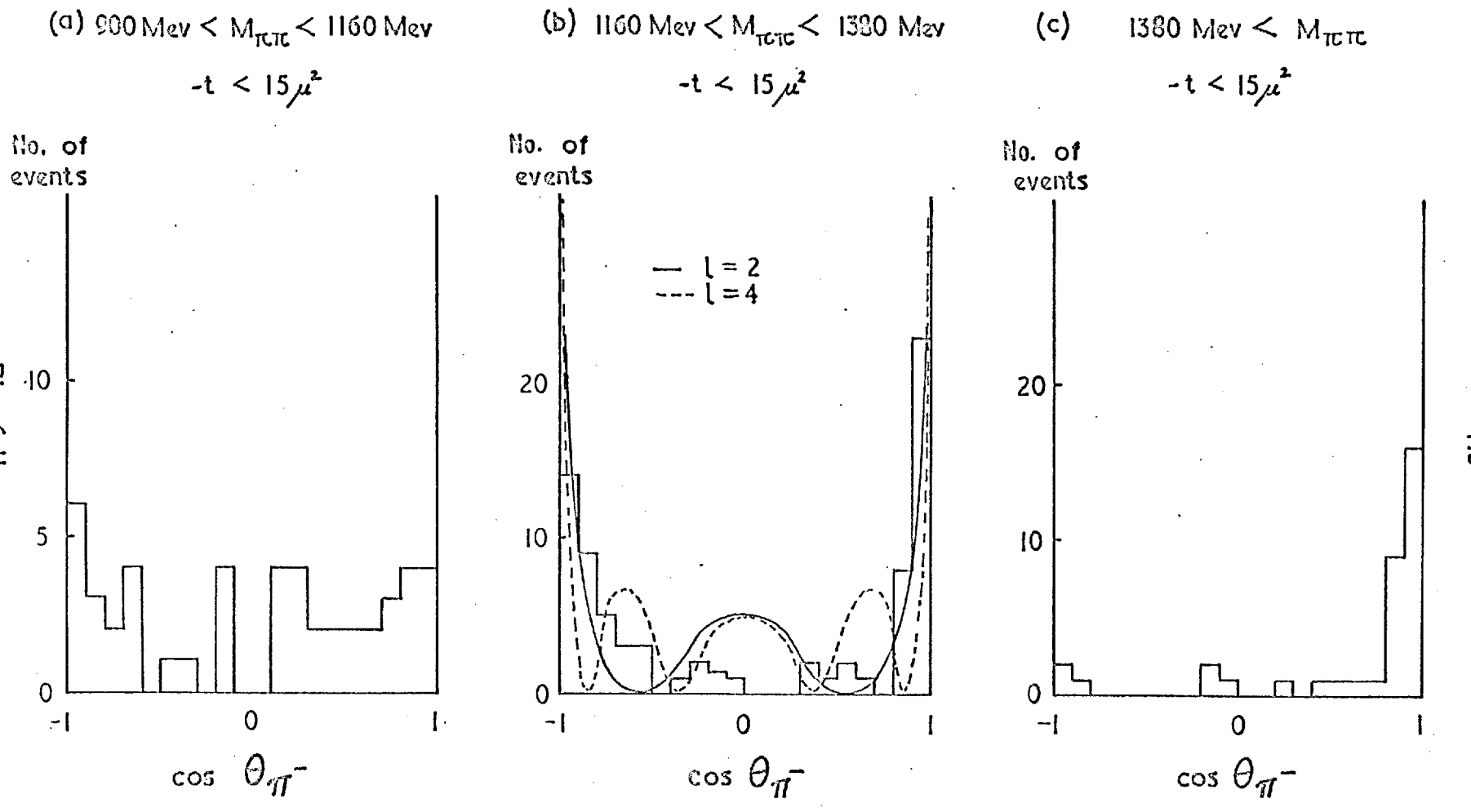

Fig. 6.11

DECAY ANGULAR DISTRIBUTION IN f^o REGION

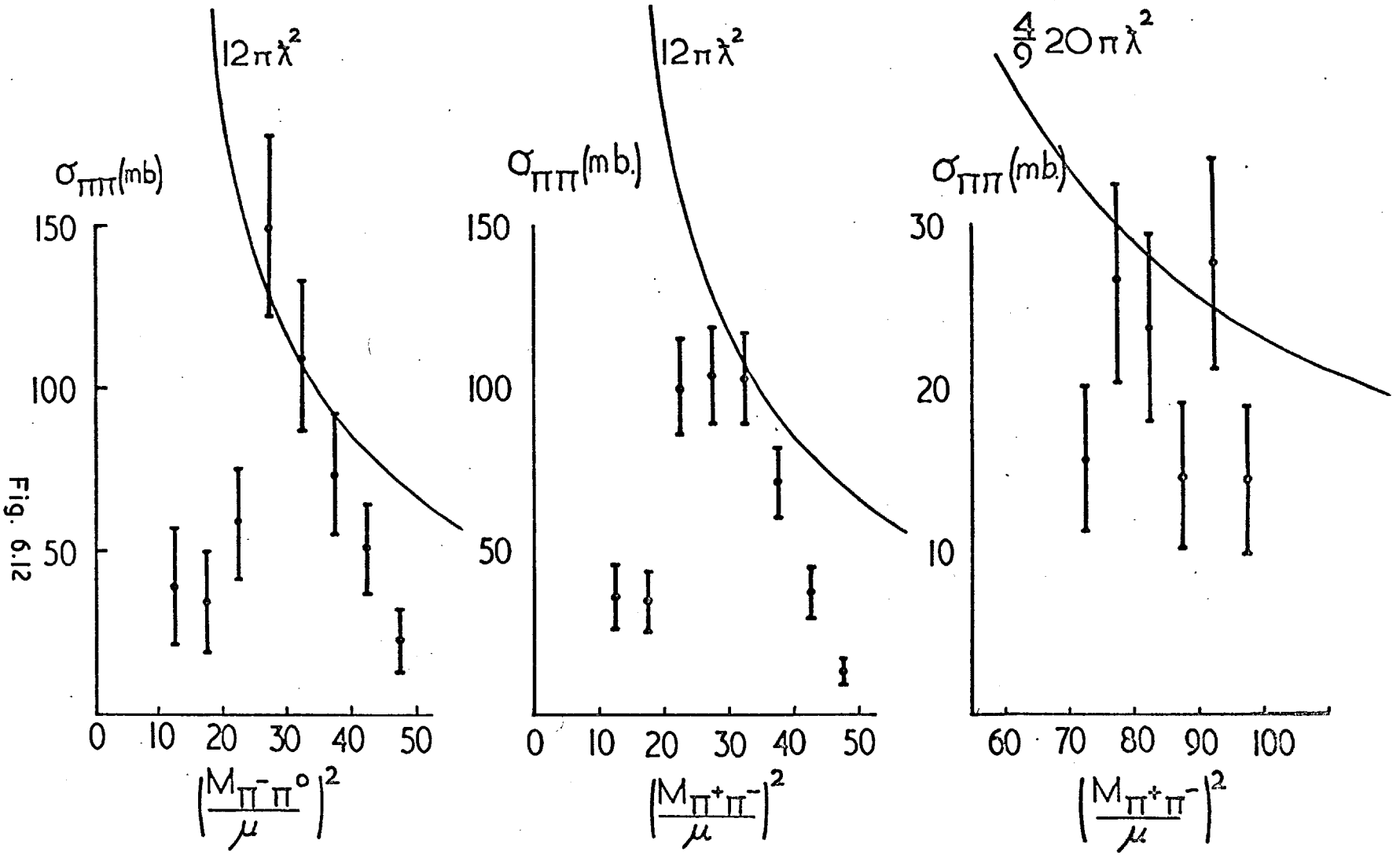
$12\pi\lambda^2$
$\sigma_{\pi\pi}$(mb)
150
100
50
0 10 20 30 40 50
$\left(\frac{M_{\pi^-\pi^0}}{\mu}\right)^2$
(a)
$12\pi\lambda^2$
$\sigma_{\pi\pi}$(mb.)
150
100
50
0 10 20 30 40 50
$\left(\frac{M_{\pi^+\pi^-}}{\mu}\right)^2$
(b)
$\frac{4}{9}20\pi\lambda^2$
$\sigma_{\pi\pi}$(mb.)
30
20
10
60 70 80 90 100
$\left(\frac{M_{\pi^+\pi^-}}{\mu}\right)^2$
(c)

Fig. 6.12

CHAPTER VII

PRELIMINARY RESULTS FROM $\pi^+ p$ INTERACTIONS AT 4Gev/c.

7.1 Experimental Method.

The film was scanned, measured, and analysed in a way similar to that described in the previous experiment on $\pi^- p$ interactions. In the case of a $\pi^+ p$ initial state, one expects an excess of two positive charges in the final state. In the two-prong and four prong reactions, the following hypothesis were tried in the fitting programme :-

$$\pi^+ p \longrightarrow \pi^+ p$$

$$\pi^+ p \longrightarrow \pi^+ p \pi^\circ \qquad \text{I}$$

$$\pi^+ p \longrightarrow \pi^+ n \pi^+ \qquad \text{II}$$

$$\pi^+ p \longrightarrow \pi^+ p \pi^+ \pi^-$$

$$\pi^+ p \longrightarrow \pi^+ p \pi^+ \pi^- \pi^\circ$$

$$\pi^+ p \longrightarrow \pi^+ n \pi^+ \pi^+ \pi^-$$

The following unfittable processes are also possible :

$$\pi^+ p \longrightarrow \pi^+ p \pi^\circ + (m \pi^\circ) \quad , \quad m \geqslant 1 \qquad \text{III}$$

$$\pi^+ p \longrightarrow \pi^+ n \pi^+ + (m \pi^\circ), \quad m \geqslant 1 \qquad \text{IV}$$

$$\pi^+ p \longrightarrow \pi^+ p \pi^+ \pi^- \pi^\circ + (m \pi^\circ), \; m \geqslant 1$$

$$\pi^+ p \longrightarrow \pi^+ n \pi^+ \pi^+ \pi^- + (m \pi^\circ), \; m \geqslant 1$$

The notation used above for the two-prong reactions corresponds to that used in the description of $\pi^- p$ interactions.

The increase in the number of positives in the final state causes more ambiguities between proton and positive pions, and hence between final state channels. This ambiguity occurs in the following way. Some events produce equally acceptable kinematic fits for some reactions, in particulr for reactions I and II. If the 'slow' positive track can be identified as a proton, the ambiguity is resolved. However, if this track is identified as a positive pion, it is necessary to identify the fast positive track. Thus, as can be seen from Table 7.1, a significantly larger number of ambiguities between reactions I and II has arisen, than was the case in the equivalent reactions in the study of $\pi^- p$ interactions. Further, due to the peripheral nature of the reactions, this 'fast' ambiguous positive track will tend to be a pion. Hence, if a weighting procedure is used to attribute such events, a physical bias will be introduced. This kind of ambiguity did not arise in the $\pi^- p$ interactions.

A sample of twenty test events is again being measured by all groups to check the consistency of methods of analysis before combination of final data.

7.2. Cross-Sections.

To date, 2545 two-prong and 960 four-prong events have been analysed by the collaboration. These events are not taken from the same sample of film, and hence are not free from physical bias. The total cross-section

is estimated at (26.6± 1.5) mb. The hydrogen density (0.0625 gm/cm^2), and the correction for loss of elastic events at small scattering angles is assumed to be the same as for the $\pi^- p$ elastic events. The error on the total cross-section quoted above includes an estimate for the uncertainty in the beam contamination correction. Table 7.1 shows the number of events analysed and the corrected cross-sections so far obtained.

TABLE 7.1

CHANNEL	NO. OF EVENTS ANALYSED	CORRECTED CROSS-SECTIONS IN mb.
$\pi^+ p$	860	6.7 ± 0.3
$\pi^+ p\ ^\circ$	395	2.6 ± 0.1
$\pi^+ n\ \pi^+$	233	1.6 ± 0.1
$\pi^+ p\ \pi^\circ + m\ \pi^\circ,\ m \geq 1$	468 (+126 allocated ambiguous events)	4.0 ± 0.2
$\pi^+ n\ \pi^+ + m\ \pi^\circ, m \geq 1$	264 (+ 69 allocated ambiguous events)	2.2 ± 0.1
Total 2-prong.	2415±130=2545	17.1 ± 0.3
$\pi^+ p\ \pi^+\ \pi^-$	307	3.0 ± 0.2
$\pi^+ p\ \pi^+\ \pi^-\ \pi^\circ$	320	3.2 ± 0.2
$\pi^+ n\ \pi^+\ \pi^+\ \pi^-$	109	1.1 ± 0.1
$\pi^+ p\ \pi^+\ \pi^-\ \pi^\circ + m\ \pi^\circ, m \geq 1$	145 (+14 allocated ambiguous events)	1.6 ± 0.1
$\pi^+ n\ \pi^+\ \pi^+\ \pi^-\ + m\pi^\circ, m \geq 1$	60 (+5 allocated ambiguous events)	0.6 ± 0.1
Total 4-prong	960	9.5 ± 0.3
TOTAL	-	26.6 ± 1.5

7.3 Two Prong Interactions.

7.3.1 Elastic Scattering Cross-Section

The elastic events have not bee fully analysed and the scanning loss correction has not been correctly estimated. However, the total elastic cross-section appears to be equal, within the errors, to that found in $\pi^- p$ elastic scattering at the same incident momentum. Pomeranchuk[67] and others have shown that as the incident energy increases, the total $\pi^+ p$ and $\pi^- p$ cross-sections should become equal, but make no predictions concerning the elastic scattering cross-section. Most theories of elastic scattering, however, indicate that diffraction scattering should become independent of isotopic spin with increasing incident energy. At an incident pion momentum of 4Gev/c, it appears that isotopic spin independence has been reached for the elastic scattering cross-section, but not for the total cross-section.

7.3.2. Single pion production.

The effective mass distributions for the $\pi^{\pm} p$ and $\pi^+ \pi^o$ combinations from reaction I are shown in Fig. 7.1. It is seen that both $N^*(3/2,3/2)$ and ρ^+ production are present in this channel. The width of the ρ^+ is estimated at (100 ± 30) mev, which is significantly narrower than for the ρ^o found in single pion production in $\pi^- p$ interactions. The cross-section for the reaction $\pi^+ p \longrightarrow p \rho^+$ was found to be (0.26 ± 0.04)mb. This reaction is the charge conjugate reaction of $\pi^- p \longrightarrow p \rho^-$, if one considers both reactions to be described by a peripheral model. The cross-

section for $\pi^- p \longrightarrow p \rho^-$ was found to be (0.45 ± 0.08) mb. If the selection of events is limited to those with low momentum transfer to the nucleon to ensure the validity of the one pion exchange model, the discrepancy between the cross-sections remains. This suggests that the production of N^* in $\pi^+ p$ interactions interferes with the production of ρ^+. This may explain the smaller width (longer lifetime) of the ρ^+ compared with the ρ^0 and ρ^-. No significant isobar formation was seen in the $\pi^- p$ inelastic interaction. This suggestion is supported by the Dalitz plot of $M^2_{p\,\pi^+}$ against $M^2_{\pi^+\pi^0}$ where a depletion of density is found in the overlap region where production of both N^* and ρ^+ is kinematically possible. (Fig.7.2(a)) More statistics are necessary to be confident of this depletion in the overlap region. The cross-section obtained for N^* production in this channel is (0.37 ± 0.06) mb.

A method of studying the mechanism of isobar production by the exchange of a vector meson has been suggested by Sakurai and Stodolsky [68]. They propose three tests for ρ exchange in $N^*(3/2,3/2)$ isobar production.

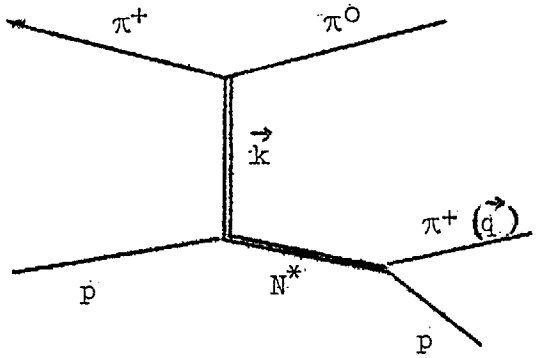

If all quantities are evaluated in the isobar rest system they make the following predictions:-

(i) The distribution of angle α between the normal to the production plane and the direction of the π^+ from the isobar,

$$\cos\alpha = \frac{\vec{p}_+ \wedge \vec{p}_o}{|\vec{p}_+ \wedge \vec{p}_o|} \cdot \frac{\vec{q}}{|\vec{q}|}$$

should have the form $1+3\cos^2\alpha$

(ii) The distribution of angle φ between planes at the upper and lower vertices (extended Treiman-Yang test)

$$\cos\varphi = \frac{\vec{p}_+ \wedge \vec{p}_o}{|\vec{p}_+ \wedge \vec{p}_o|} \cdot \frac{\vec{k} \wedge \vec{q}}{|\vec{k} \wedge \vec{q}|}$$

should have the form $1+2\sin^2\varphi$

(iii) The distribution of angle γ between the direction of the π^+ from the isobar and the direction of the incident π^+

$$\cos\gamma = \vec{q} \cdot \vec{p}_+ \Big/ |\vec{q} \cdot \vec{p}_+|$$

should have the form $1 - {}^3/_5 \cos^2\gamma$.

The first two tests have been applied with the present statistics. Fig. 7.3 shows the experimental $\cos\alpha$ distribution compared with the expected distribution for isobar production in the reaction $\pi^+ p \rightarrow N^*({}^3/_2, {}^3/_2) + \pi^o$, and is seen to agree well. The second test, however, produces an isotropic distribution, (Fig. 7.4) and hence no firm conclusion can be drawn at present. The third test has not yet been applied. It may be added

however that the possible $N^*(^3/2,^3/2) - \rho^+$ interference suggested above could complicate these N^* exchange tests.

The effective mass distribution for the $\pi^+ \pi^+$ system from the reaction $\pi^+ p \longrightarrow \pi^+ n \pi^+$ (Fig. 7.1(c)), shows no evidence for resonance production. This reaction enables the study of a pure T=2 $\pi\pi$ state, and it is hoped that it will provide a starting point for a complete determination of $\pi\pi$ scattering phase shifts in the T=0, 1 and 2 channels.

7.3.3. Multipion production

The cross-section for $\pi^+ p \rightarrow \pi^+ \; n \pi^+ + m\pi^0$, $m \geqslant 1$ (2.2 ± 0.1)mb, which is significantly lower than (5.57 ± 0.17) mb. found for the $\pi^- p \longrightarrow \pi^- n \pi^+ + m \pi^0$, $m \geqslant 1$ reaction. This confirms the suggestion of high cross-section for ω^0 production in the latter reaction. Of course, one cannot form ω^0 in the former reaction.

Fig. 7.2 (b) shows the missing mass squared distribution from the reaction $\pi^+ p \rightarrow \pi^+ \; p \pi^0 + m\pi^0$, $m \geqslant 1$. The peak at 0.3 Gev^2 yields a cross-section of (0.29 ± 0.07) mb for η production, assuming that 72% of all η mesons decay neutrally. The equivalent process $\pi^- p \rightarrow \pi^- \; p\pi^0 + m\pi^0$, $m \geqslant 1$, yielded a cross-section of (0.11 ± 0.03) mb. for η production.

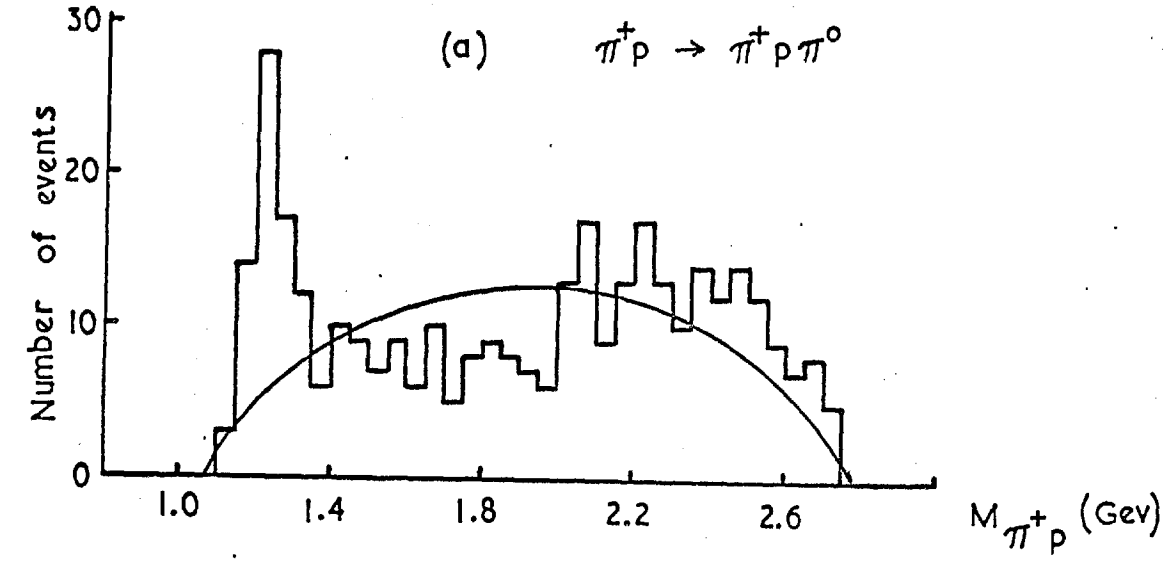
(a) $\pi^+ p \rightarrow \pi^+ p \pi^0$
Number of events
30
20
10
0
1.0
1.4
1.8
2.2
2.6
$M_{\pi^+ p}$ (Gev)

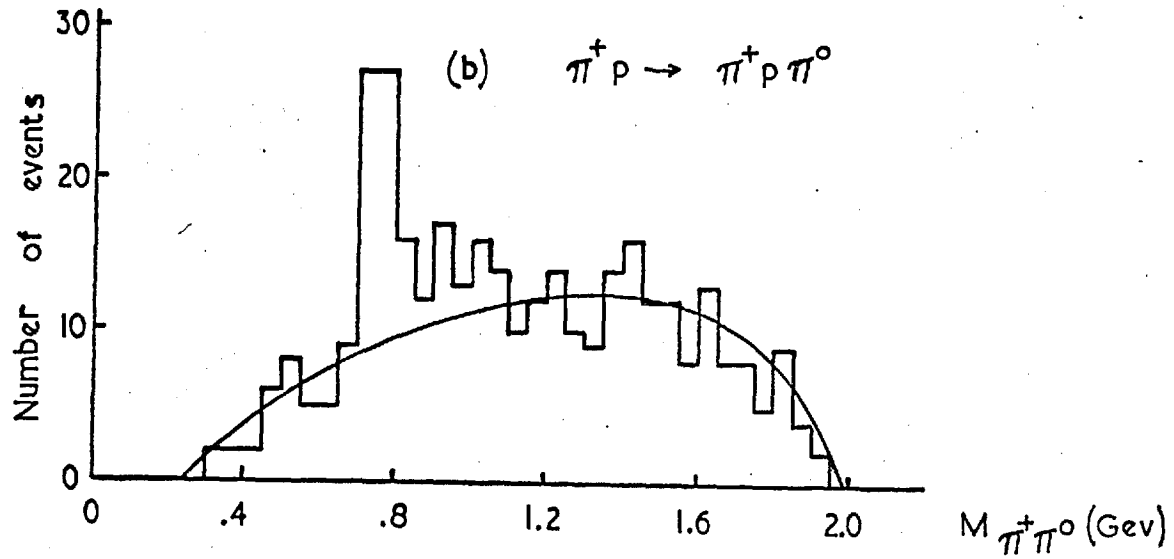
(b) $\pi^+ p \rightarrow \pi^+ p \pi^0$
Number of events
30
20
10
0
0
.4
.8
1.2
1.6
2.0
$M_{\pi^+ \pi^0}$ (Gev)

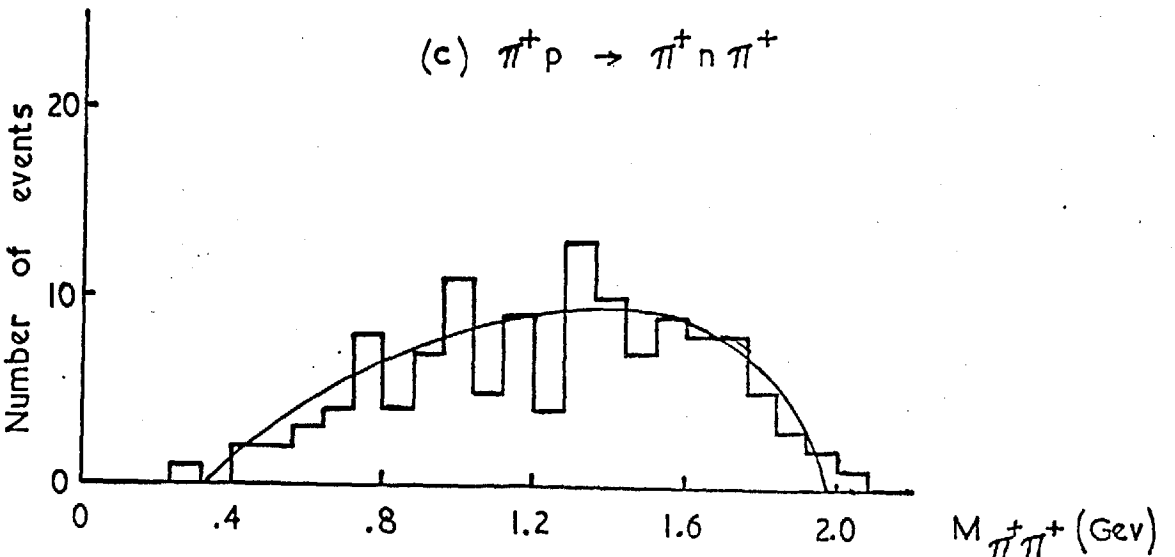
(c) $\pi^+ p \rightarrow \pi^+ n \pi^+$
Number of events
20
10
0
0
.4
.8
1.2
1.6
2.0
$M_{\pi^+ \pi^+}$ (Gev)

Fig 7.1

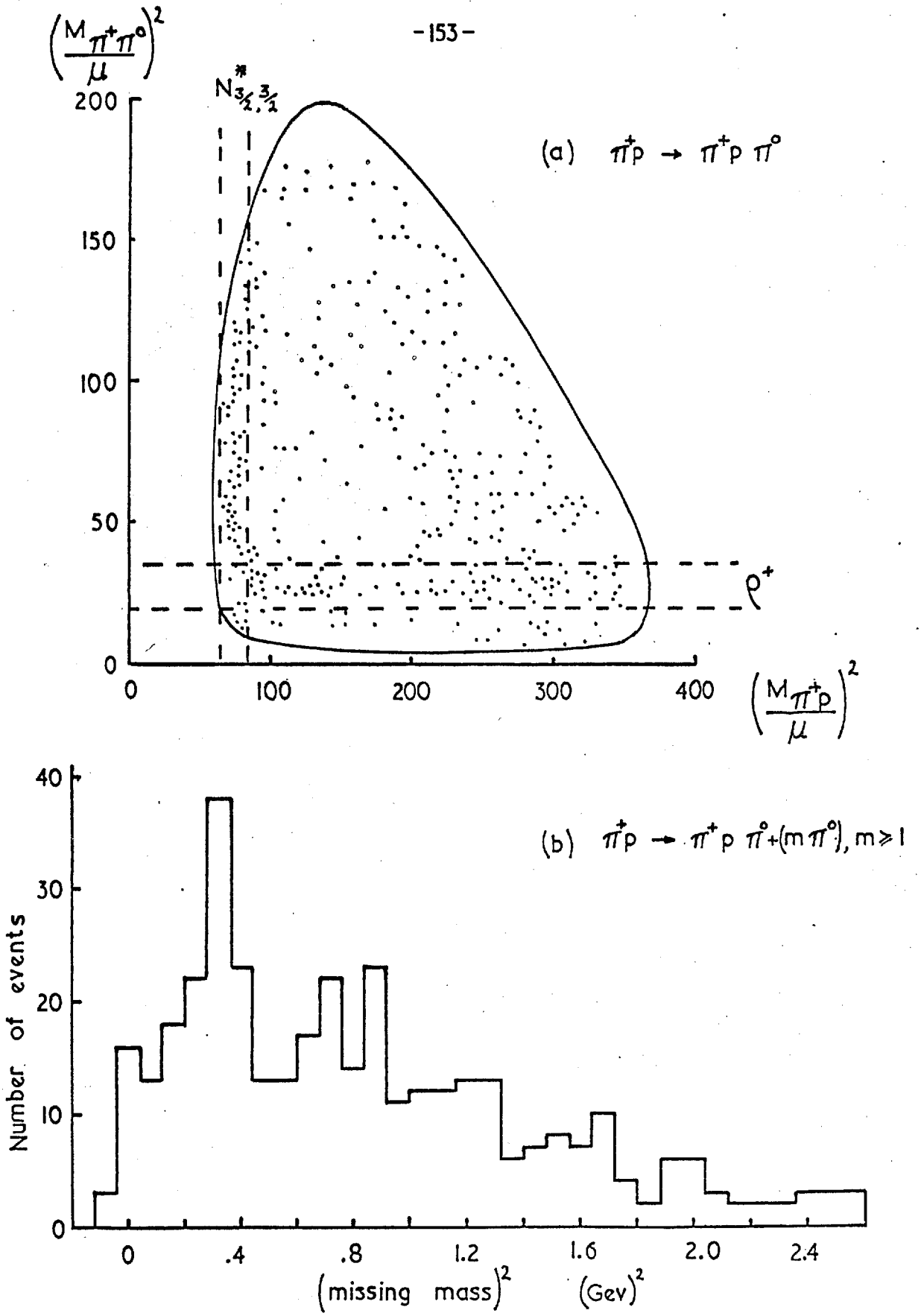
$\left(\frac{M_{\pi^+\pi^0}}{\mu}\right)^2$
$N^*_{3/2,3/2}$
(a) $\pi^+p \to \pi^+p\,\pi^0$
200
150
100
50
0
ρ^+
0
100
200
300
400
$\left(\frac{M_{\pi^+p}}{\mu}\right)^2$
(b) $\pi^+p \to \pi^+p\,\pi^0+(m\pi^0)$, $m \geq 1$
Number of events
40
30
20
10
0
0
.4
.8
1.2
1.6
2.0
2.4
(missing mass)^2 (Gev)^2

Fig 7.2

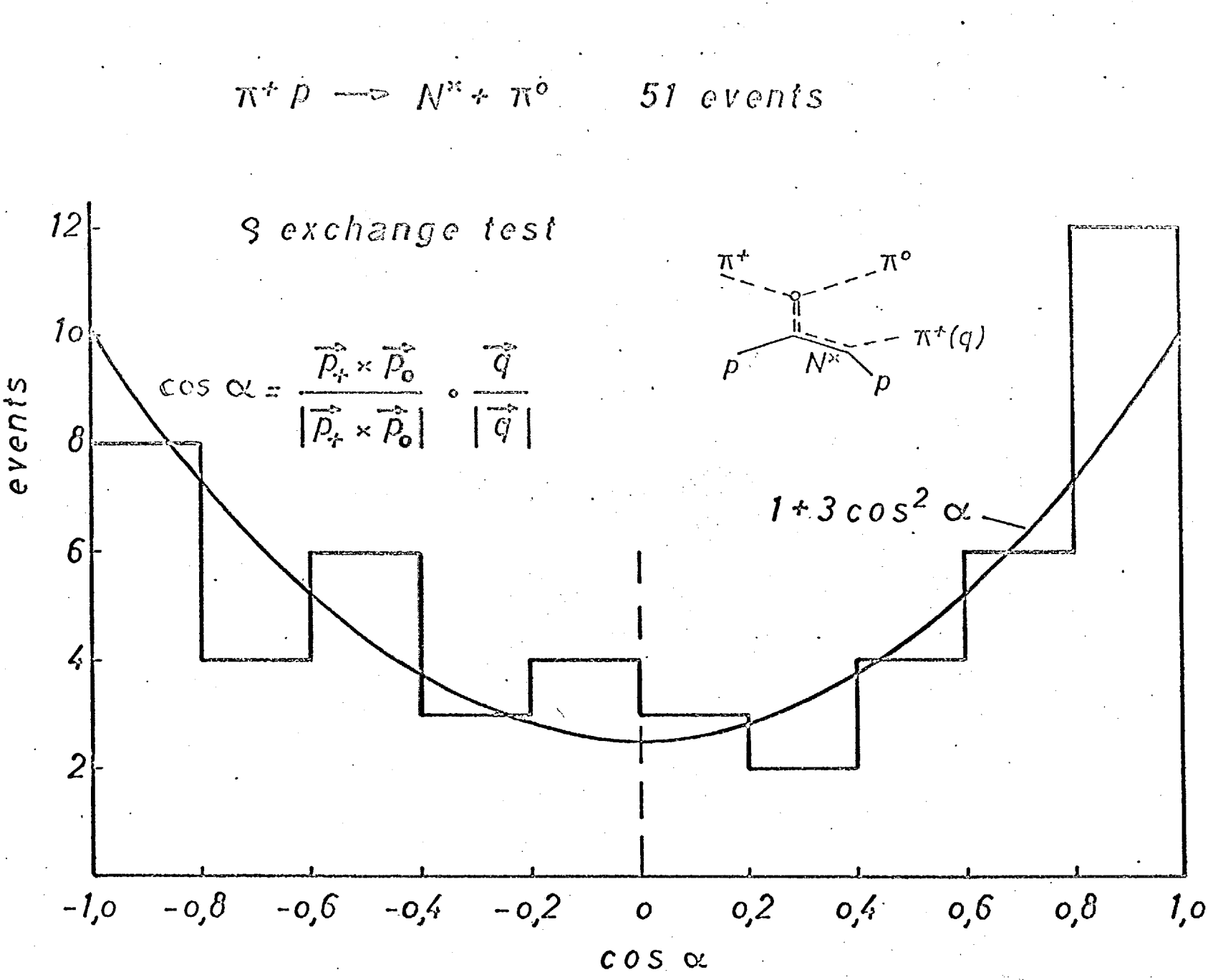
$\pi^+ p \longrightarrow N^{*} + \pi^0$ 51 events
9 exchange test
$\cos\alpha = \frac{\vec{p}_+ \times \vec{p}_0}{|\vec{p}_+ \times \vec{p}_0|} \cdot \frac{\vec{q}}{|\vec{q}|}$
π^+
π^0
$\pi^+(q)$
p
N^{*}
p
$1+3\cos^2\alpha$
events
12
10
8
6
4
2
-1,0
-0,8
-0,6
-0,4
-0,2
0
0,2
0,4
0,6
0,8
1,0
cos α

Fig. 7.3

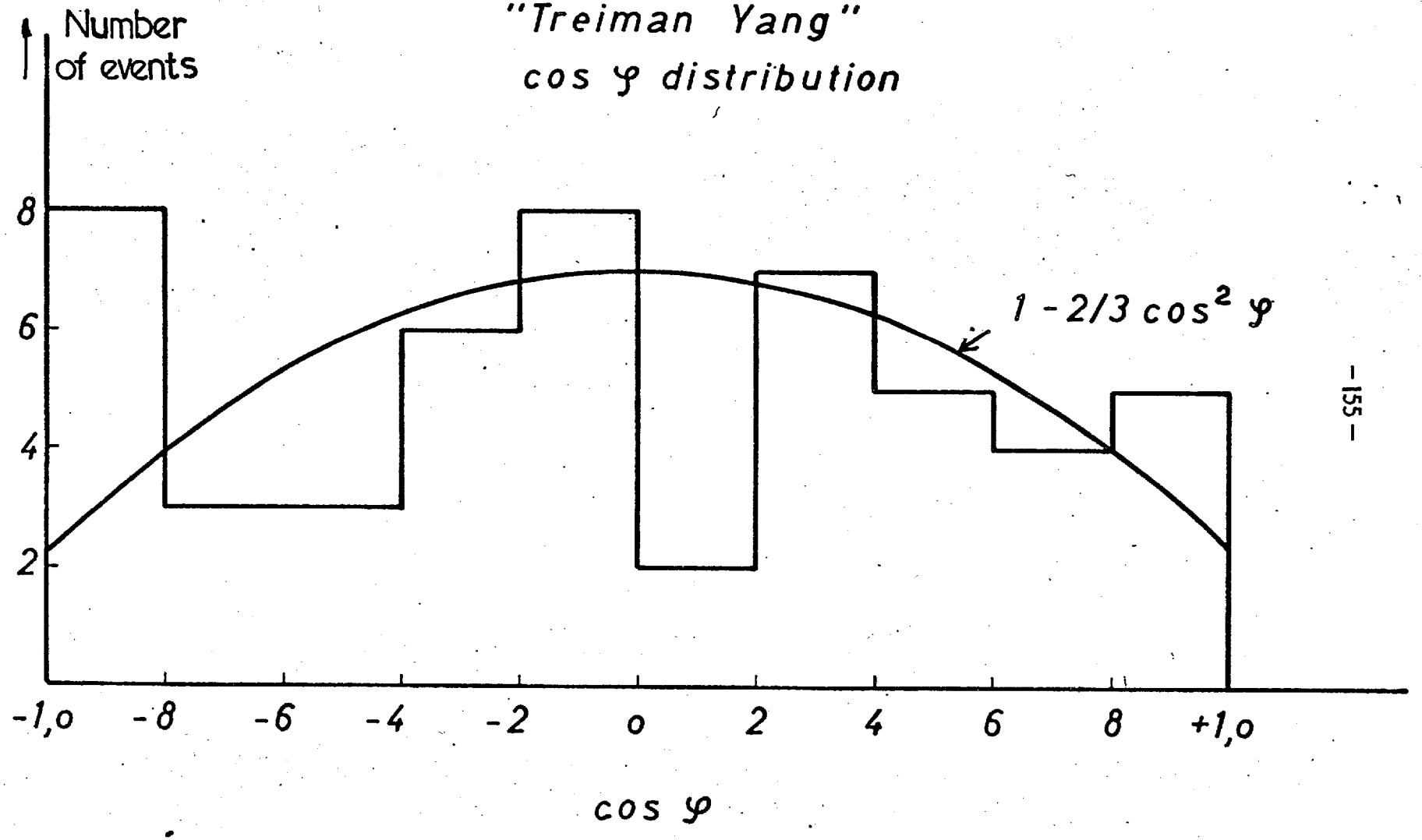
"Treiman Yang"
cos φ distribution
Number of events
8
6
4
2
1 - 2/3 cos² φ
-1,0
-8
-6
-4
-2
0
2
4
6
8
+1,0
cos φ

Fig. 7.4

ACKNOWLEDGEMENTS

The author would like to thank Professor P.M.S. Blackett for the opportunity of working in his laboratory, and Professor C.C. Butler for his supervision of the work.

He is especially grateful to Mr. N.C. Barford for his guidance in the first phase of his work, and to Dr. I. Butterworth for his encouragement and constructive criticism in all phases of the work.

The contributions of all members of the collaboration and the CERN programming staff are gratefully acknowledged. The author would like to thank Mr. L.M. Celnikier for his work on the CERN programmes.

The author wishes to thank his colleagues Dr. Y.S. Liu, Mr. F. Campayne and Miss J. Brownlee for their efforts during the analysis of the pion film.

The work of the Imperial College technical staff is gratefully acknowledged, especially that of Mr. R.F. Wilkins and Mr. A. Cleary for keeping the scanning and measuring machines in order, and that of Miss G. Coster, Miss M. Goodwin, Miss J. Davies and Mrs. J. Sutherland for their diligent work on scanning and book-keeping.

Finally, the author wishes to thank the Department of Scientific and Industrial Research, for a maintenance grant between 1958 and 1961.

REFERENCES

(1) R.B. PALMER, Ph.D. Thesis, Imperial College.

(2) D. REED, Ph.D. Thesis, Imperial College.

(3) Aachen-Bonn-Birmingham-Hamburg-Imperial College-Munich collaboration:

Physics Letters, Vol. 5. No:2 p.153.

Physics Letters, Vol. 5. No:3 p.209.

Nuovo Cimento, Two Prong Interactions, to be published, Nuovo Cimento

Nuovo Cimento, Four Prong Interactions, to be published, Nuovo Cimen

(4) D.A. GLASER, Phys. Rev. 87, 665 (1952); 91, 762 (1955).

(5) N.C. BARFORD; Progress in Gyogenics, 1960.

H. BRADNER; Ann. Rev. Nuc. Sci. 10, 1960.

(6) F. SEITZ; Phys. Fluids, 1, 2, 1958.

(7) The Engineer, May 8th. (1963) p.481.

(8) E. FERMI. Prog. Theor. Phys. (Japan);5, 570 (1950); Phys. Rev., 92, 452 (1953); 93, 1435 (1954).

(9) LINDENBAUM & STERNHEIMER; Phys. Rev. 105, 6, 1874, (1957); 123, 1, 333, (1961)

(10) W.R. FRAZER, J.R. FULCO; Phys. Rev. 117, 1609 (1960).

(11) J. BOWCOCK, W.N. COTLINGHAM, D. LURIE. Phys.Rev.Lett. 5, 386 (1960)

(12) A.R. ERWIN, R.H. MARCH, W.D. WALKER, E. WEST; P.R.L. 6, 628 (1961)

(13) D. STONEHILL, C. BALTAY, H.COURANT, W. FICKINGER, H. KRAYBILL, J. SANDWEISS, J. SANFORD, H. TAFT; P.R.L. 6, 624 (1961).

(14) E. PICKUP, D.K. ROBINSON, E.O. SALANT; P.R.L. 7, 192 (1961)
D. CARMONY, R.T. VAN de WALLE; P.R.L. 8, 73 (1962)

(15) M. ROOS, Rev. Mod. Phys. 35, 2, (1963).

(16) J. BUTTON, G.R. KALBFLEISCH, G.R. LYNCH, B.C. MAGLIC, A.H. ROSENFELD, Phys. Rev. 126, 1858 (1962).

(17) B.C. MAGLIC, L.W. ALVAREZ, A.M. ROSENFELD, M.L. STEVENSON; P.R.L. 7, 178 (1961).

(18) A. PEVSNER, K. KRAEMER, M. NUSSBAUM, P.SCHLEIN, A. KOVAS, C.MELTZER; Proc. 1961 Aix-en-Provence conf. p.277.

(18) -continued-

N.W. XUONG, G.R. LYNCH; P.R.L. 7, 327 (1961).
E.L. HART, R.I. LOUTTIT, T.W. MORRIS; P.R.L. 9, 133 (1962).

(19) J. STEINBERGER et. al. Sienna Conference 1963, to be published.
R. ARMENTEROS et. al. Sienna Conference 1963, to be published.

(20) Y. NAMBU; Phys. Rev. 106, 1366 (1957).

(21) G.F. CHEW; P.R.L. 4, 142 (1960).

(22) L. BASTIEN, J.P. BERGE, O.I. DAHL, M.FERRO-LUZZI, D.H. MILLER, J.J. MURRAY, A.H. ROSENFELD, M.B. WATSON; P.R.L. 8, 114 (1962).

(23) G.R. LYNCH: Review paper presented at High Energy Physics Conference, at Imperial College, March 1962.

(24) A.ABASHIAN, N. BOOTH, K. CROWE, P.R.L. 5, 258 (1960)
C. MENCUCCINI, R. QUERZOLI, G. SALVINI, V.G. SILVESTRINI, CERN Conference 1962, p.33.

A.V.AREFEV et. al., CERN Conference 1962, p.112.

(25) R. BARLOUTAUD, J. HEUGHEBAERT, A.LEVEQUE, J. MEYER, R. OMNES; P.R.L. 8, 32 (1962).

(26) D.L. STONEHILL, H. KRAYBILL , Phys. Rev. (to be published).

(27) W. SELOVE, V. HAGOPIAN, H. BRODY, A. BAKER, E. LEBOY: P.R.L. 8, 272, (1962).

(28) G.F. CHEW, S.C. FRAUTSCHI; P.R.L. 8, 41 (1962).

(29) G.F. CHEW, F.F. LOW; Phys. Rev. 113, 1640 (1959).

(30) J. ANDERSON, V.O. BANG, P.G. BURKE, D.D. CARMONY, P.R.L., 6 365 (1961).

(31) D.D. CARMONY, Ph.D. Thesis, University of California (1961), UCRL 988
L.B. AUERBACH, T. ELLIOTT, W.B. JOHNSON, P.R.L. 9, 173 (1962).

(32) Saclay-Orsay-Bari-Bologna Collaboration, preprint.

(33) SCHIFF, Quantum Mechanics, p.199.

(34) P.T. MATTHEWS, internal communication.

(35) P.P. SRIVASTAVA, G. SUDARSHAN, Phys. Rev., 110, 765 (1958).

(36) Les chambres a bulles Francaises au CERN published in L'Onde Electrique, December 1961.

(37) H. SHERMAN, Ph.D. Thesis, Imperial College (1963).

(38) W.G. MOORHEAD, CERN report 60-33.
R. BOCK, 'GRIND' Manual (CERN Publication).
... R. BOCK, CERN Report 61-29.

(39) ROSSI, High Energy Particles p.68 and p.13-20.

(40) O'CEALLAIGH; CERN Report BS 11 (1954).

(41) B.N. FABIAN, R.L. PLACE, W.A. RILEY, W.H. SIMS, V.P. KENNEY, Rev. Sci. Inst. May 1963.

(42) Y.S. LIU, Ph.D. Thesis Imperial College (1963).

(43) M. CHRETIEN, J. LEITNER, N.P. SAMIOS, M. SCHWARTZ, J. STEINBERGER Phys. Rev. 108, 383 (1957).

(44) R.G. THOMAS, Phys. Rev. 120, 1015 (1960).

(45) R. SERBER, P.R.L. 10, 357 (1963).

(46) T. REGGE, Nuovo Cimento 18, 947 (1960).

(47) G.F. CHEW & S.C. FRAUTSCHI, P.R.L. 8, 394 (1961).

(48) C.C. TING, L.W. JONES, & M.L. PERL; P.R.L. 9, 468 (1962).

(49) S. BRANDT, V.T. COCCONI, D.R.O. MORRISON, A. WROBLEWSKI, P. FLEURY, G. KAYAS, F. MULLER, C. PELLETIER; P.R.L. 10, 413 (1963).

(50) LANDAU & LIFSHITZ, Quantum Mechanics, pps. 436-7.

(51) J.W. CRONIN, Phys. Rev., 118, 824 (1960).

(52) S.J. LINDENBAUM, W.A. LOVE, J.A. NIEDERER, S. OZAKI, J.J. RUSSELL L.C.L. YUAN: P.R.L. 7, 352 (1961).
G. von DARDEL, D. DEKKERS, R. MERMOD, M. VIVARGANT, G. WEBER, K. WINTER; P.R.L. 8, 173 (1962).
A.N. DIDDENS, E.W. JENKINS, T.F. KYCIA, K.R. RILEY; P.R.L. 10, 262 (1963).

(53) Saclay-Bari-Bologna-Orsay Collaboration- preprint (1962).
M.J. LONGO, B.J. MOYER; P.R.L. 9, 466 (1962).
C.C. TING, L.W. JONES, M.L. PERL, p.r.l. 9, 468 (1962).

(54) S.B. TREIMAN, C.N. YANG; P.R.L. 8, 140 (1962).

(55) Aachen-Birmingham-Bonn-Hamburg-London (I.C.) - Munich collaboration; Four Prong Events, Nuovo Cimento, to be published.

(56) N.P. SAMIOS, A.H. BACHMAN, R.M. LEA, T.E. KALOGEROPOULOS; P.R.L. 9, 139 (1962).

(57) C. ALFF, D. BERLEY, D. COLLEY, N. GELFAND, U. NAUENBERG, D. MILLER, J. SCHULTZ; J. STEINBERGER, T.H. TAU, H. BRUGGER, P. KRAEMER, R. PLANO P.R.L. 9, 325 (1962).....

(57) continued -

M. MEER, R. STRAND, R. KRAEMER, L. MANDANSKY, M. NUSSBAUM, A. PEVSNER, T. TOOHIG, M. BLOCK, S. ORENSTEIN, T. FIELDS: Proc. of 1962 CERN Conference, p.103.

(58) D.H. SHARP and W.G. WAGNER, Cal. Tech. Calif (1963) to be published.

(59) V. HAGOPIAN, Ph.D. Thesis, University of Pennsylvania (1963)

(60) J.R. AITCHESON, Brookhaven National Laboratory preprint (1963).

(61) G. PUPPI; Proc. of 1962 CERN Conference p.713.

(62) W.J. FICKINGER, D.K. ROBINSON, E.O. SALANT; P.R.L. 10, 457 (1963).

(63) J. BERNSTEIN, G. FEINBERG, Nuovo Cimento, XXV 6, 1343 (1962). S. GLASHOW, P.R.L. 7, 469 , 1961.

(64) W.D. WALKER, E. WEST, A.R. ERWIN, R.H. MARCH; Proc. of 1962 CERN Conference, p.41.

(65) G.F. CHEW, S.C. FRAUTSCHI, P.R.L. 8, 41, (1962).

(66) K. IGI, P.R.L. 10, 820 (1963).

(67) J. POMERANCHUK, Soviet Phys. JETP, 7, 499 (1958).

(68) L. STODOLSKY, J.J. SAKURAI, P.R.L. 11, 90 (1963).

(69) Z.G.T. GUIRAGOSSIAN, P.R.L. 11, 85 (1963).

(70) J.J. VEILLET, J. HENNESSY, H. BINGHAM. M. BLOCK, D. DRIJARD, A. LAGARRIGUE, P. MITTNER, A. ROUSSET, G. BELLINI, M. CORATO, E. FIORINI, P. NEGRI, Preprint (1963).

FIGURE CAPTIONS

FIG. 1.1. Idealised bubble chamber pressure pulse.

FIG. 1.2. 40 cm. bubble chamber diagrammatic gas expansion circuit.

FIG. 1.3. (a) Typical timing sequence of expansion and pilot valves used in the 40 cm. bubble chamber.

(b) Schematic diagram of expansion valve operation.

FIG. 1.4. (a) Fast Pilot valve.
(b) Discharge circuit used for pilot valve.
(c) Oscilloscope trace of the pilot valve piston monitor.

FIG. 1.5. 40 cm. bubble chamber body.

FIG. 1.6. Various expansion valve designs used in the 40 cm. and British National chambers.

(a) Original valve.
(b) 'Gaco' spool valve.
(c) National Chamber valve - latest design.

FIG. 1.7. Schematic illustration of British National bubble chamber, showing the chamber body and control system.

FIG. 3.1. Flow diagram of the 4Gev/c $\pi^{\pm}$ experiment.

FIG. 3.2. The layout of the 4Gev/c pion beam. Q represents magnetic quadrupole, BM represents bending magnet.

FIG. 3.3. Co-ordinate system associated with the 81 cm. bubble chamber and cameras, and the fiducial volume as defined by the Imperial College Group.

FIG. 3.4. Range-Momentum curves for liquid hydrogen (density 0.06 gm/cm^3).

FIG. 3.5. Scan sheet and Kinematics sheet from a typical two-prong event.

FIG. 4.1 Distribution of fitted beam momentum taken from all two prong events at Imperial College.

FIG. 4.2. (a) Distribution of measured beam track azimuthal angle taken from all two prong events measured at I.C., and extrapolated to x = -28 cm. The effective beam-track selection criterion as applied on the scanning table is indicated by the arrows.
(b) Distribution of errors in azimuthal angle as calculated by GAP.

FIG. 4.3. (a) Distribution of measured beam track dip angle taken from all two prong events measured at I.C.

(b) Distribution of errors in dip angle as calculated by GAP.

FIG. 4.4. Apex distributions taken from all two prong events measured at I.C. (a) X-co-ordinate distribution.
(b) y-co-ordinate.
(c) z-co-ordinate.

FIG. 4.5. χ^2 distributions from Imperial College measurements for reactions (a) $\pi^- p \rightarrow \pi^- p$

(b) $\pi^- p \rightarrow \pi^- p\ \pi^o$

(c) $\pi^- p \rightarrow \pi^- n\ \pi^+$

The solid lines show the theoretical χ^2 predictions.

FIG. 4.6. Probability χ^2 distribution for the reactions $\pi^- p \rightarrow \pi^- p$; $\pi^- p \rightarrow \pi^- p\ \pi^o$, $\pi^- p \rightarrow \pi^- n\ \pi^+$ taken together.

FIG. 4.7. Missing mass squared distributions from Imperial College measurements for the reactions

(a) $\pi^- p \rightarrow \pi^- p$

(b) $\pi^- p \rightarrow \pi^- p \pi^o$

(c) $\pi^- p \rightarrow \pi^- n\ \pi^+$

FIG. 4.8. Missing mass squared distributions from Imperial College measurements for the reactions.

(a) $\pi^- p \rightarrow \pi^- n\ \pi^+$; $\pi^- p \rightarrow \pi^- n\ \pi^+ (m\ \pi^o)$, $m \geq 1$

(b) $\pi^- p \rightarrow \pi^- p\ \pi^o$; $\pi^- p \rightarrow \pi^- p \pi^o\ (m\ \pi^o)$, , $m \geq 1$

FIG. 4.9. Ionisation-Momentum curves for the range of momenta 80 Mev/c - 5Gev/c.

FIG. 4.10. Semi-Logarithmic plot of number of gaps against gap length for beam track and an 890 Mev/c positive secondary.

FIG. 4.11. Diagram showing the fiducial regions used by each group.

FIG. 5.1.. Distributions of azimuthal angle ϕ of the scattering plane with respect to optic axis, for elastic events, and for different ranges of $-t$, the four-momentum transfer to the nucleon.

FIG. 5.2. Differential cross-section for elastic scattering. The curves shown are predicted by a simple optical model with $R = 1.0 \times 10^{-13}$ cm, and $R = 1.1 \times 10^{-13}$ cm.

FIG. 5.3. Differential cross-section for elastic scattering.

(a) for all values of $-t$
(b) for $-t < 0.6$ Gev^2
The solid line shows the fit $(52.87 \pm 3.96)\exp(8.33 \pm 0.49)\ t$.

FIG. 5.4. Pion-proton total cross sections in the range of incident pion kinetic energies 1 to 6 Gev.

FIG. 5.5. Effective mass distribution of $\pi\pi$ system:

(a) reaction $\pi^- p \longrightarrow \pi^- p\ \pi^o$

(b) reaction $\pi^- p \longrightarrow \pi^- n\ \pi^+$

Phase space curves normalised to events outside ρ and f^o peaks.

FIG. 5.6. Effective mass distributions for πN system in the reaction $\pi^- p \longrightarrow \pi^- p\ \pi^o$: (a) $\pi^o p$ (b) $\pi^- p$ and reaction $\pi^- p \longrightarrow \pi^- n \pi^+$: (c) $\pi^+ n$ (d) $\pi^- n$

FIG. 5.7. (a) One Pion exchange diagram for reaction $\pi^- p \longrightarrow \pi^- p\ \pi^o$

(b) One Pion exchange diagram for reaction $\pi^- p \longrightarrow \pi^- n\ \pi^+$

(c) Definition of planes in Treiman-Yang test.

FIG. 5.8. Distribution of four-momentum transfer to the nucleon in the reactions $\pi^- p \longrightarrow p + \rho^-$; $\pi^- p \longrightarrow n + \rho^o$ $\pi^- p \longrightarrow n + f^o$. The solid lines show $\frac{\partial \sigma}{\partial t} = A\exp(8{,}53t)$.

FIG. 5.9. Distribution of four-momentum transfer to the nucleon

(a) for reaction $\pi^- p \longrightarrow p + \rho^-$;

(b) $\pi^- p \longrightarrow n + \rho^o$

(c) $\pi^- p \longrightarrow n + f^o$.

The solid line shows the prediction of the Selleri formula. Only those events with $-t \leq 30\mu^2$ are included.

FIG. 5.10. Treiman-Yang angle distribution for reaction $\pi^- p \rightarrow \pi^- p \pi^0$
(a) All values of $-t$, (c) $-t \leq 15\mu^2$
and reaction $\pi^- p \rightarrow \pi^- n \pi^+$
(b) All values of $-t$, (d) $-t \leq 15\mu^2$.

FIG. 5.11. Centre of mass momentum distributions for reaction $\pi^- p \rightarrow \pi^- p \pi^0$(I) and $\pi^- p \rightarrow \pi^- n \pi^+$ (II):
(a) proton from reaction I, (b) π^- from reaction I,
(c) π^0 from reaction I, (d) neutron from reaction II,
(e) π^- from reaction II, (f) π^+ from reaction II.

FIG. 5.12. Centre of mass angular distribution for reactions $\pi^- p \rightarrow \pi^- p \pi^0$ (I) and $\pi^- p \rightarrow \pi^- n \pi^+$ (II) :
(a) proton from reaction I, (b) π^- from reaction I,
(c) π^0 from reaction I, (d) neutron from reaction II,
(c) π^- from reaction II, (f) π^+ from reaction II.

FIG. 5.13. Effective mass distribution of $\pi^+ \pi^-$ system from the reaction $\pi^- p \rightarrow \pi^- n \pi^+ + (m \pi^0)$; $m \geq 1$. The solid curves show phase space predictions for N+3π and N+4 π final states, each normalised to the total number of events.

FIG. 5.14. Effective mass distribution of $\pi^- p$ system from the reaction $\pi^- p \rightarrow \pi^- p \pi^0 + (m \pi^0)$; $m \geq 1$.

FIG. 5.15. Missing mass squared distribution for the reaction $\pi^- p \rightarrow \pi^- p \pi^0 + (m \pi^0)$, $m \geq 1$.

FIG. 5.16. Centre of mass momentum distributions for the reaction $\pi^- p \rightarrow \pi^- n \pi^+ + (m \pi^0)$, $m \geq 1$: (a) π^+ (b) π^-

FIG. 5.17. Centre of mass momentum distributions for the reaction $\pi^- p \rightarrow \pi^- p \pi^0 + (m \pi^0)$, $m \geq 1$: (a) proton (b) π^-

FIG. 5.18. Centre of mass angular distributions for the reaction $\pi^- p \rightarrow \pi^- n \pi^+ + (m \pi^0)$, $m \geq 1$: (a) π^+ (b) π^-

FIG. 5.19. Centre of mass angular distribution for the reaction $\pi^- p \rightarrow \pi^- p \pi^0 + (m\pi^0)$, $m \geq 1$: (a) proton (b) π^-.

FIG. 6.1. Chew-Low plot of $(M_{\pi^- \pi^0}/\mu)^2$ against $-t/\mu^2$ for the reaction $\pi^- p \rightarrow \pi^- p \pi^0$. The solid line represents the lower kinematic limit on $-t$.

FIG. 6.2. Chew-Low plot of $(M_{\pi^+ \pi^-}/\mu)^2$ against $-t/\mu^2$ for the reaction $\pi^- p \rightarrow \pi^- n \pi^+$. The solid line represents the lower kinematic limit on $-t$.

FIG. 6.3. Centre of mass angular distributions of the $\pi\pi$ systems:
(a) in the ρ^- mass region of reaction $\pi^- p \rightarrow \pi^- p \pi^0$
(b) in the ρ^0 mass region of reaction $\pi^- p \rightarrow \pi^- n \pi^+$
(c) in the f^0 mass region of reaction $\pi^- p \rightarrow \pi^- n \pi^+$

FIG. 6.4. Dalitz plot of $(\frac{M_{\pi\pi}}{\mu})^2$ against $(\frac{M_{\pi N}}{\mu})^2$:
(a) for reaction $\pi^- p \rightarrow \pi^- p \pi^0$ and (b) $\pi^- p \rightarrow \pi^- n \pi^+$.
The dotted lines indicate the isobar bands.

FIG. 6.5. Dalitz plot of $(\frac{M_{\pi\pi}}{\mu})^2$ against $(\frac{M_{\pi N}}{\mu})^2$ for events with $-t < 15\mu^2$: (a) for reaction $\pi^- p \rightarrow \pi^- p \pi^0$
(b) for reaction $\pi^- p \rightarrow \pi^- n \pi^+$.

FIG. 6.6. Isobar production in two prong interactions by ρ-exchange.

FIG. 6.7. Scatter diagram of $(\frac{M_{\pi^- \pi^0}}{\mu})^2$ versus the angle between the incoming and outgoing π^- in the $\pi^- \pi^0$ rest system for $-t < 15\mu^2$.

FIG. 6.8. Scatter diagram of $(\frac{M_{\pi^+ \pi^-}}{\mu})^2$ versus the angle between the incoming and outgoing π^- in the $\pi^+ \pi^-$ rest system for $-t < 15\mu^2$.

FIG. 6.9. Diagram of forward-backward decay asymmetry for the $\pi\pi$ system as a function of $(\frac{M_{\pi\pi}}{\mu})^2$ from the reactions $\pi^- p \rightarrow \pi^- p \pi^0$ and $\pi^- p \rightarrow \pi^- n \pi^+$, and for $-t < 15\mu^2$.

FIG. 6.10. Effective mass distributions for the $\pi^+\pi^-$ system from the reaction $\pi^- p \rightarrow \pi^- n \pi^+$
(a) for events in which the laboratory momentum of the π^+ was greater than 1.7. Gev/c.
(b) for events with $-t < 7_\mu^2$
(c) for events with $-t > 7_\mu^2$

FIG. 6.11. Distribution of decay angle of the outgoing $\bar{\pi}$ with respect to the incident π^- in the $\pi^+\pi^-$ rest system for events from reaction $\pi^- p \rightarrow n \pi^+ \pi^-$ with $-t < 15\mu^2$, and in the mass region of the f^o.

FIG. 6.12. Cross-section for $\pi\pi$ scattering: (a) from reaction $\pi^- p \rightarrow \pi^- p \pi^o$ in the ρ^- region (b) from reaction $\pi^- p \rightarrow \pi^- n \pi^+$ in the ρ^o region (c) from the reaction $\pi^- p \rightarrow \pi^- n \pi^+$ in the f^o region.

FIG. 7.1. Effective mass distributions for the reaction $\pi^+ p \rightarrow \pi^+ p \pi^o$ (a) $M_{p\pi^+}$ (b) $M_{\pi^+\pi^o}$; and for the reaction $\pi^- p \rightarrow \pi^+ n \pi^+$ (c) $M_{\pi^+\pi^+}$

FIG. 7.2. (a) Dalitz plot of $\left(\frac{M_{\pi\pi}}{\mu}\right)^2$ again $\left(\frac{M_{\pi N}}{\mu}\right)^2$ for reaction $\pi^+ p \rightarrow \pi^+ p \pi^o$.
(b) Missing mass squared distribution from the reaction $\pi^+ p \rightarrow \pi^+ p \pi^o + m\pi^o$, $m \geq 1$.

FIG. 7.3. Isobar formation by ρ-exchange -Sakurai test. Distribution of angle α between the normal to the production plane and the direction of the π^+ from the isobar for events consistent with $\pi^+ p \rightarrow N^*(3/2, 3/2) + \pi^o$.

FIG. 7.4. Isobar formation by ρ-exchange -Sakurai test. Distribution of angle φ between planes at upper and lower vertices for events consistent with $\pi^+ p \rightarrow N^*(3/2, 3/2) + \pi^o$.